

# The effective use of BLAS interface for implementation of finite-element ADER-DG and finite-volume ADER-WENO methods

Popov I.S.\*

August 22, 2024

Numerical methods of the ADER family, in particular finite-element ADER-DG and finite-volume ADER-WENO methods, are among the most accurate numerical methods for solving quasilinear PDE systems. The internal structure of ADER-DG and ADER-WENO numerical methods contains a large number of basic linear algebra operations related to matrix multiplication. At the moment, the main interface of software libraries for high-performance computing is BLAS. This paper presents an effective method for integration the standard functions of the BLAS interface into the implementation of these numerical methods. The calculated matrices are small matrices; at the same time, the proposed implementation makes it possible to effectively use existing JIT technologies. The proposed approach immediately operates on AoS, which makes it possible to efficiently calculate flux, source and non-conservative terms without need to carry out transposition. The obtained computational costs allowed to conclude that the effective implementation, based on the use of the JIT functions of the BLAS, outperformed both the implementation based on the general BLAS functions and the naive implementations by several times. At the same time, the complexity of developing an implementation based on the approach proposed in this work does not exceed the complexity of developing a naive optimized implementation.

**PACS.** 47.11.-j, 47.11.Fg, 47.11.Df, 02.70.Dh, 47.40.-x, 47.40.Nm

**2000 MSC.** 65M60, 76M10, 76M12, 35L60, 35L65, 35L45, 35L67

**Key Words.** computational fluid dynamics, conservation laws, non-conservative PDE systems, HRS, HRSCS, ADER-DG, ADER-WENO-FV, LST-DG predictor, a posteriori limitation, BLAS

## Introduction

Numerical methods based on the ADER (Arbitrary high order using DERivatives) paradigm, in particular, finite-element ADER discontinuous Galerkin (DG) methods and finite-volume ADER-WENO methods, are among the most high-precision and high-order numerical methods for simulating evolutionary quasilinear systems of partial differential equation (PDEs). Initially, the ADER paradigm was developed in works [1, 2] for use in finite-volume numerical methods, and was based on the use of the Cauchy-Kowalewski procedure. Subsequently, methods were developed [3, 4] based on the use of a local discrete space-time solution, which was calculated by the local space-time discontinuous Galerkin (LST-DG) predictor. The current state of finite-volume and finite-element DG numerical methods based on the use of the ADER paradigm originates from the development of the Multi-dimensional Optimal Order Detection (MOOD) paradigm [5], as a result of which finite-element ADER-DG methods with a posteriori correction of the solution in subcells by a finite-volume limiter were developed [6–9].

Currently, finite-element ADER-DG methods and finite-volume ADER-WENO methods are used to simulate classical ideal and dissipative hydrodynamic and magnetohydrodynamic flows [10–12], solve problems of hydrodynamics and magnetohydrodynamics in the special and general theory of relativity [13–15], simulate the movements of deformable elastic media [16–18], simulate propagation of seismic waves [16, 19–21], propagation of detonation waves [22], solve the shallow water equations [23, 24], simulate the blood flow [25]; and many other problems [16, 19]. Finite-element ADER-DG methods and finite-volume ADER-WENO methods are developed for both structured Cartesian meshes [6, 7, 13–15], using the adaptive mesh refinement paradigm [8–11, 26], and unstructured triangular and tetrahedral meshes [27–29], and moving meshes [30]. The papers [16, 17, 19, 31–34] discuss the features of the mathematical and algorithmic formulations of numerical methods, as well as the features of their software implementation. Dumbser *et al* developed *well-balanced* ADER-DG method for GRGD problems [15] and for the multilayer shallow water equations [24]. ADER-DG methods were used to solve ODE systems in [3, 29, 35]. The modern state of development of the space-time finite-element ADER-DG is presented in the works [36, 37].

The internal structure of ADER-DG and ADER-WENO methods, especially those based on the use of LST-DG predictor to obtain a local discrete space-time solution, contains a large number of basic linear algebra operations related to matrix multiplication. At the moment, the main interface of software libraries for high-performance computing is BLAS. A method of use of the BLAS interface proposed in the work [16] involves complex additional procedures associated with the calculation of flux, source and non-conservative terms. One should choose a method for 5d array storage, which is the classic AoS vs SoA problem, known in computer science. In the works [16, 19] the use of SoA is proposed, which allows the use of small matrices, well suited for the `lixsmm` library of small matrices computations. However, this choice requires laborious calculations of flux, source and non-conservative terms – direct calculation requires transposing the matrices of the expansion coefficients of the local discrete space-time solution. Despite the fact that the work [16] proposes to use a very efficient implementation of this transposition operation, based on “on the fly” conversion with efficient use of registers of the AVX, AVX2 and AVX-512

\*Department of Theoretical Physics, Dostoevsky Omsk State University, Omsk, Russia [diphosgen@mail.ru](mailto:diphosgen@mail.ru), [popovis@omsu.ru](mailto:popovis@omsu.ru)

instruction subsets, this leads to complication of the computational code and makes it natively dependent on the details of the device of the modern version of the x86 instruction set architecture.

In this work an effective method for integration the standard functions of the BLAS interface into the implementation of these numerical methods has been developed and presented. The proposed approach is different from that in [16, 19]. The proposed approach immediately operates on AoS, which makes it possible to efficiently calculate flux, source and non-conservative terms, in this case, there is no need to carry out transposition, which must be carried out in the algorithm proposed in the work [16] and implemented in the work [19]. Detailed algorithms and tables with function parameters are presented.

## 1 Mathematical framework

In this work, the initial non-homogeneous non-conservative PDE system was chosen in the following form:

$$\frac{\partial \mathbf{U}}{\partial t} + \nabla \cdot \mathbb{F}(\mathbf{U}) + \mathbf{B}(\mathbf{U}) \cdot \nabla \mathbf{U} = \mathbf{S}(\mathbf{U}, \mathbf{r}, t), \quad (1)$$

where  $\mathbf{U} \in \Omega_U \subseteq \mathcal{R}^M$  is the vector of conserved values,  $\mathbb{F}(\mathbf{U}) = (\mathbf{F}_x(\mathbf{U}), \mathbf{F}_y(\mathbf{U}), \mathbf{F}_z(\mathbf{U}))$  is the flux tensor,  $\mathbf{B}(\mathbf{U}) = (\mathbb{B}_x(\mathbf{U}), \mathbb{B}_y(\mathbf{U}), \mathbb{B}_z(\mathbf{U}))$  is a vector of matrices  $M \times M$  defining non-conservative terms,  $\mathbf{S} = \mathbf{S}(\mathbf{U}, \mathbf{r}, t)$  is an algebraic source term. In the expressions presented here and further in the text, an arbitrary dependence of the source terms  $\mathbf{S}$  on coordinates  $\mathbf{r}$  and  $t$  is assumed. However, the flux tensor  $\mathbb{F}(\mathbf{U})$  and matrices of non-conservative terms  $\mathbf{B}$  can also depend on  $(\mathbf{r}, t)$ , this is in no way restricted to the obtained expressions – such dependence can occur in case of using curvilinear systems for coordinates and time. The system of equations can be represented in the non-conservative form  $\partial \mathbf{U} / \partial t + \mathbf{A}(\mathbf{U}) \cdot \nabla \mathbf{U} = \mathbf{S}(\mathbf{U}, \mathbf{r}, t)$ , where  $\mathbf{A}(\mathbf{U}) = \partial \mathbb{F}(\mathbf{U}) / \partial \mathbf{U} + \mathbf{B}$ . The PDE system (1) is hyperbolic if for all vectors  $\mathbf{a} \neq \mathbf{0}$  and for all vectors  $\mathbf{U} \in \Omega_U$  the matrix  $\mathbf{A}(\mathbf{U}) \cdot \mathbf{a}$  has  $M$  real eigenvalues and a full set of  $M$  linearly independent right eigenvectors. Hyperbolicity is of fundamental importance for obtaining a solution to the Riemann problem of calculating fluxes at cell interfaces in these numerical methods; however, hyperbolicity is not fundamental to allow a Riemann solver to correctly calculate fluxes for parabolic PDEs. The system of equations (1) in Cartesian coordinates  $(x, y, z)$ , which is used in this work, takes the following form:

$$\frac{\partial \mathbf{U}}{\partial t} + \frac{\partial \mathbf{F}_x(\mathbf{U})}{\partial x} + \frac{\partial \mathbf{F}_y(\mathbf{U})}{\partial y} + \frac{\partial \mathbf{F}_z(\mathbf{U})}{\partial z} + \mathbb{B}_x(\mathbf{U}) \cdot \frac{\partial \mathbf{U}}{\partial x} + \mathbb{B}_y(\mathbf{U}) \cdot \frac{\partial \mathbf{U}}{\partial y} + \mathbb{B}_z(\mathbf{U}) \cdot \frac{\partial \mathbf{U}}{\partial z} = \mathbf{S}(\mathbf{U}, \mathbf{r}, t). \quad (2)$$

The computational domain  $\Omega \subset \mathcal{R}^3$  is discretized by a spatial mesh  $\Omega = \cup_i \Omega_i$  with coordinate cells  $\Omega_i = [x_{i_1}, x_{i_1+1}] \times [y_{i_2}, y_{i_2+1}] \times [z_{i_3}, z_{i_3+1}]$ , where  $x_{i_1+1} - x_{i_1} = \Delta x$ ,  $y_{i_2+1} - y_{i_2} = \Delta y$ ,  $z_{i_3+1} - z_{i_3} = \Delta z$ ; and  $i$  is a three-component multi-index  $i = (i_1, i_2, i_3)$ . As a result of time discretization  $t^n$  with time step  $\Delta t^n = t^{n+1} - t^n$ , the set of space-time elements  $\Omega_{n,i} = [t^n, t^{n+1}] \times \Omega_i$  was obtained in which a local space-time coordinate system  $(\tau, \boldsymbol{\xi})$ , with  $\boldsymbol{\xi} = (\xi, \eta, \zeta)$ , was introduced in the following form:

$$t = t^n + \Delta t^n \cdot \tau; \quad x = x_{i_1} + \Delta x \cdot \xi; \quad y = y_{i_2} + \Delta y \cdot \eta; \quad z = z_{i_3} + \Delta z \cdot \zeta; \quad 0 \leq \tau, \xi, \eta, \zeta \leq 1, \quad (3)$$

which maps the element  $\Omega_{n,i}$  to a reference space-time element  $\omega_4 = [0, 1] \times \omega_3 = [0, 1]^4$ . In the coordinate system (3) of the reference space-time element  $\Omega_{n,i}$ , the system of equations (2) can be written in the following form:

$$\frac{\partial \mathbf{u}}{\partial t} + \frac{\partial \mathbf{f}_\xi(\mathbf{u})}{\partial \xi} + \frac{\partial \mathbf{f}_\eta(\mathbf{u})}{\partial \eta} + \frac{\partial \mathbf{f}_\zeta(\mathbf{u})}{\partial \zeta} + \mathfrak{B}_\xi(\mathbf{u}) \cdot \frac{\partial \mathbf{u}}{\partial \xi} + \mathfrak{B}_\eta(\mathbf{u}) \cdot \frac{\partial \mathbf{u}}{\partial \eta} + \mathfrak{B}_\zeta(\mathbf{u}) \cdot \frac{\partial \mathbf{u}}{\partial \zeta} = \mathbf{s}(\mathbf{u}, \mathbf{r}(\boldsymbol{\xi}), t(\tau)), \quad (4)$$

where

$$\begin{aligned} \mathbf{u} &= \mathbf{U}, & \mathbf{f}_\xi &= \frac{\Delta t^n}{\Delta x} \cdot \mathbf{F}_x, & \mathbf{f}_\eta &= \frac{\Delta t^n}{\Delta y} \cdot \mathbf{F}_y, & \mathbf{f}_\zeta &= \frac{\Delta t^n}{\Delta z} \cdot \mathbf{F}_z, \\ \mathfrak{B}_\xi &= \frac{\Delta t^n}{\Delta x} \cdot \mathbb{B}_x, & \mathfrak{B}_\eta &= \frac{\Delta t^n}{\Delta y} \cdot \mathbb{B}_y, & \mathfrak{B}_\zeta &= \frac{\Delta t^n}{\Delta z} \cdot \mathbb{B}_z, & \mathbf{s} &= \Delta t^n \cdot \mathbf{S}, \end{aligned} \quad (5)$$

define the rescaled flux tensor, matrices of non-conservative terms, and source terms. A detailed description of the mathematical framework is based on works [6–11, 13–15, 26, 28–30], and is provided primarily to derive the final formulaic apparatus for which the implementation has been developed.

The finite-element ADER-DG and finite-volume ADER-WENO methods are based on the use of a discrete space-time solution  $\mathbf{q}(\tau, \boldsymbol{\xi})$  obtained by the LST-DG predictor [6, 8–11, 16]. The discrete solution  $\mathbf{q}$  determines the solution of the problem in the small, describing the dynamic evolution of the solution in the space-time element  $\Omega_{n,i}$  without taking into account the interaction with other mesh cells, and is represented in the form:

$$\mathbf{q}(\tau, \boldsymbol{\xi}) = \sum_p \hat{\mathbf{q}}_p \Theta_p(\tau, \boldsymbol{\xi}), \quad (6)$$

where  $\Theta_p(\tau, \boldsymbol{\xi})$  is the basis functions,  $\hat{\mathbf{q}}_p$  is the representation coefficients,  $p = (p_0, p_1, p_2, p_3)$  is the four-component multi-index. The basis functions  $\Theta_p(\tau, \boldsymbol{\xi})$  were chosen in the form of tensor products of the nodal basis functions  $\Theta_p(\tau, \boldsymbol{\xi}) = \varphi_{p_0}(\tau) \varphi_{p_1}(\xi) \varphi_{p_2}(\eta) \varphi_{p_3}(\zeta)$ , where  $\varphi_k(\xi)$  are the nodal basis functions, which are Lagrange interpolation polynomials of degree  $N$ , with nodal points at the roots  $\xi_l$  of the Legendre polynomials  $P_{N+1}(\xi)$ :  $\varphi_k(\xi_l) = \delta_{kl}$ , and  $0 \leq p_0, p_1, p_2, p_3 \leq N$ . However, the roots of Radau polynomials, Lobatto polynomials and other polynomials can be chosen as nodal points [38]. In the finite-element ADER-DG method, the solution  $\mathbf{u}^n(\boldsymbol{\xi})$  in the cell  $\Omega_i$  at the time step  $t^n$  is represented in the form:

$$\mathbf{u}^n(\boldsymbol{\xi}) = \sum_k \hat{\mathbf{u}}_k^n \Phi_k(\boldsymbol{\xi}), \quad (7)$$

where  $\Phi_k(\boldsymbol{\xi})$  is the basis functions,  $\hat{\mathbf{u}}_k^n$  is the representation coefficients,  $k = (k_1, k_2, k_3)$  is the three-component multi-index,  $0 \leq k_1, k_2, k_3 \leq N$ . The basis functions  $\Phi_k(\boldsymbol{\xi})$  were also chosen in the form of tensor products of the nodal basis functions

$\Phi_k(\tau, \boldsymbol{\xi}) = \varphi_{k_1}(\xi)\varphi_{k_2}(\eta)\varphi_{k_3}(\zeta)$ . In the finite-volume ADER-WENO method, the solution in the cell  $\Omega_i$  at the time step  $t^n$  is represented by a finite-volume average value  $\mathbf{v}_i^n$ :

$$\mathbf{v}_i^n = \int_0^1 d\xi \int_0^1 d\eta \int_0^1 d\zeta \cdot \mathbf{u}(\mathbf{r}(\boldsymbol{\xi}), t^n). \quad (8)$$

Using the values  $\mathbf{v}_j^n$  in the set of cells  $\Omega_j$  surrounding the cell  $\Omega_i$ , WENO-reconstruction of the solution is performed, allowing to obtain a highly accurate representation of the solution  $\mathbf{w}^n(\boldsymbol{\xi})$  at the time step  $t^n$ , which was presented in the form:

$$\mathbf{w}^n(\boldsymbol{\xi}) = \sum_k \hat{\mathbf{w}}_k^n \Phi_k(\boldsymbol{\xi}), \quad (9)$$

which is technically similar to the DG representation (7) of the solution, however, instead of the coefficients  $\hat{\mathbf{u}}_k^n$  in the expression, the coefficients  $\hat{\mathbf{w}}_k^n$  that are calculated in the WENO-reconstruction of the solution are used.

## 2 LST-DG predictor

### 2.1 General description

The system of nonlinear algebraic equations of the LST-DG predictor was obtained as a result of substitution  $\mathbf{u} \mapsto \mathbf{q}$  into the system of equations (4) and using the condition for the  $L_2$  projection of the residual to be zero on the test functions, for which the functions  $\Theta_p(\tau, \boldsymbol{\xi})$  were chosen, integrating by parts over time  $\tau$  in the time term, and using the initial condition  $\mathbf{q}(0, \boldsymbol{\xi}) = \mathbf{u}(\boldsymbol{\xi})$  (7), which leads to the following expression [6, 8–11, 16]:

$$\begin{aligned} [\Theta_p, \mathbf{q}](1) - [\Theta_p, \mathbf{u}](0) + \left\langle \frac{\partial \Theta_p}{\partial \tau}, \mathbf{q} \right\rangle + \left\langle \Theta_p, \left( \frac{\partial \mathbf{f}_\xi(\mathbf{q})}{\partial \xi} + \frac{\partial \mathbf{f}_\eta(\mathbf{q})}{\partial \eta} + \frac{\partial \mathbf{f}_\zeta(\mathbf{q})}{\partial \zeta} \right) \right\rangle \\ + \left\langle \Theta_p, \left( \mathfrak{B}_\xi(\mathbf{q}) \cdot \frac{\partial \mathbf{q}}{\partial \xi} + \mathfrak{B}_\eta(\mathbf{q}) \cdot \frac{\partial \mathbf{q}}{\partial \eta} + \mathfrak{B}_\zeta(\mathbf{q}) \cdot \frac{\partial \mathbf{q}}{\partial \zeta} - \mathbf{s}(\mathbf{q}, \mathbf{r}(\boldsymbol{\xi}), t(\tau)) \right) \right\rangle = 0, \end{aligned} \quad (10)$$

where following integral operators for  $L_2$  scalar products were introduced to simplify the notation:

$$\begin{aligned} [f(\tau, \boldsymbol{\xi}), g(\tau, \boldsymbol{\xi})](\tau) &= \int_0^1 d\xi \int_0^1 d\eta \int_0^1 d\zeta \cdot f(\tau, \boldsymbol{\xi})g(\tau, \boldsymbol{\xi}); \\ \langle f(\tau, \boldsymbol{\xi}), g(\tau, \boldsymbol{\xi}) \rangle &= \int_0^1 d\tau \cdot [f(\tau, \boldsymbol{\xi}), g(\tau, \boldsymbol{\xi})](\tau) = \int_0^1 d\tau \int_0^1 d\xi \int_0^1 d\eta \int_0^1 d\zeta \cdot f(\tau, \boldsymbol{\xi})g(\tau, \boldsymbol{\xi}). \end{aligned} \quad (11)$$

This form of the system of predictor equations is written for ADER-DG method, but for finite-volume ADER-WENO method it is enough to select the initial condition in the form  $\mathbf{q}(0, \boldsymbol{\xi}) = \mathbf{w}(\boldsymbol{\xi})$  of a reconstructed function (9). The use of the Gaussian quadrature formula, in this case the chosen basis is the Gauss-Legendre quadrature formula:

$$\int_0^1 d\xi \cdot f(\xi) \approx \sum_{k=0}^N w_k f(\xi_k), \quad w_k = \int_0^1 d\xi \cdot \varphi_k^2(\xi), \quad \sum_{k=0}^N w_k = 1, \quad (12)$$

makes it possible to approximately use the point-wise evaluation [39, 40] of the physical fluxes and sources:

$$\begin{aligned} \mathbf{f}_\xi(\mathbf{q}) &\approx \sum_p \Theta_p \cdot \mathbf{f}_\xi(\hat{\mathbf{q}}_p), \quad \mathbf{f}_\eta(\mathbf{q}) \approx \sum_p \Theta_p \cdot \mathbf{f}_\eta(\hat{\mathbf{q}}_p), \quad \mathbf{f}_\zeta(\mathbf{q}) \approx \sum_p \Theta_p \cdot \mathbf{f}_\zeta(\hat{\mathbf{q}}_p), \\ \mathfrak{B}_\xi(\mathbf{q}) \cdot \frac{\partial \mathbf{q}}{\partial \xi} &\approx \sum_p \Theta_p \cdot \left( \mathfrak{B}_\xi(\hat{\mathbf{q}}_p) \sum_r \frac{\partial \Theta_r(\tau_p, \boldsymbol{\xi}_p)}{\partial \xi} \cdot \hat{\mathbf{q}}_r \right), \quad \mathfrak{B}_\eta(\mathbf{q}) \cdot \frac{\partial \mathbf{q}}{\partial \eta} \approx \sum_p \Theta_p \cdot \left( \mathfrak{B}_\eta(\hat{\mathbf{q}}_p) \sum_r \frac{\partial \Theta_r(\tau_p, \boldsymbol{\xi}_p)}{\partial \eta} \cdot \hat{\mathbf{q}}_r \right), \\ \mathfrak{B}_\zeta(\mathbf{q}) \cdot \frac{\partial \mathbf{q}}{\partial \zeta} &\approx \sum_p \Theta_p \cdot \left( \mathfrak{B}_\zeta(\hat{\mathbf{q}}_p) \sum_r \frac{\partial \Theta_r(\tau_p, \boldsymbol{\xi}_p)}{\partial \zeta} \cdot \hat{\mathbf{q}}_r \right), \quad \mathbf{s}(\mathbf{q}, \mathbf{r}(\boldsymbol{\xi}), t(\tau)) \approx \sum_p \Theta_p \cdot \mathbf{s}(\hat{\mathbf{q}}_p, \mathbf{r}(\boldsymbol{\xi}_p), t(\tau_p)), \end{aligned} \quad (13)$$

The approximation by point-wise evaluation can be proved by the following consideration: consider the representation of the source term as an expansion in basis functions in the form:

$$\mathbf{s}(\mathbf{q}, \mathbf{r}(\boldsymbol{\xi}), t(\tau)) = \sum_p \Theta_p \cdot \mathbf{s}_p, \quad \mathbf{s}_p = \frac{\langle \Theta_p, \mathbf{s}(\mathbf{q}, \mathbf{r}(\boldsymbol{\xi}), t(\tau)) \rangle}{\langle \Theta_p, \Theta_p \rangle}, \quad (14)$$

where as a result of using the Gauss-Legendre quadrature formula and the definition of Lagrange interpolation polynomials  $\varphi_p(\xi_k) = \delta_{pk}$ , the following can be obtained:

$$\langle \Theta_p, \mathbf{s}(\mathbf{q}, \mathbf{r}(\boldsymbol{\xi}), t(\tau)) \rangle \approx w_{p_0} w_{p_1} w_{p_2} w_{p_3} \cdot \mathbf{s}(\mathbf{q}_p, \mathbf{r}(\boldsymbol{\xi}_p), t(\tau_p)), \quad \langle \Theta_p, \Theta_p \rangle = w_{p_0} w_{p_1} w_{p_2} w_{p_3}, \quad (15)$$

as a result of which we obtain the point-wise evolution for the source term  $\mathbf{s}_p \approx \mathbf{s}(\mathbf{q}_p, \mathbf{r}(\boldsymbol{\xi}_p), t(\tau_p))$ . Similar transformations can be carried out for all conservative and non-conservative flow terms, which also can be proved the point-wise evaluation of the

physical fluxes. As a result of the approximation by point-wise evaluation, the system of equations of the LST-DG predictor takes the following form:

$$\begin{aligned}
& \sum_q [\Theta_p, \Theta_q](1) \cdot \hat{\mathbf{q}}_q - \sum_q \left\langle \frac{\partial \Theta_p}{\partial \tau}, \Theta_q \right\rangle \cdot \hat{\mathbf{q}}_q + \sum_q \left\langle \Theta_p, \frac{\partial \Theta_q}{\partial \xi} \cdot \mathbf{f}_\xi(\hat{\mathbf{q}}_q) + \frac{\partial \Theta_q}{\partial \eta} \cdot \mathbf{f}_\eta(\hat{\mathbf{q}}_q) + \frac{\partial \Theta_q}{\partial \zeta} \cdot \mathbf{f}_\zeta(\hat{\mathbf{q}}_q) \right\rangle \\
& - \sum_q \langle \Theta_p, \Theta_q \rangle \left( \mathbf{s}(\hat{\mathbf{q}}_q, \mathbf{r}(\boldsymbol{\xi}_q), t(\tau_q)) - \sum_r \left( \mathfrak{B}_\xi(\hat{\mathbf{q}}_q) \frac{\partial \Theta_r(\tau_q, \boldsymbol{\xi}_q)}{\partial \xi} + \mathfrak{B}_\eta(\hat{\mathbf{q}}_q) \frac{\partial \Theta_r(\tau_q, \boldsymbol{\xi}_q)}{\partial \eta} + \mathfrak{B}_\zeta(\hat{\mathbf{q}}_q) \frac{\partial \Theta_r(\tau_q, \boldsymbol{\xi}_q)}{\partial \zeta} \right) \cdot \hat{\mathbf{q}}_r \right) \\
& = \sum_k [\Theta_p, \Phi_k](0) \cdot \hat{\mathbf{u}}_k,
\end{aligned} \tag{16}$$

where the left side of the system of equations contains functional structures containing the desired quantities  $\hat{\mathbf{q}}_p$ , and the right side contains known coefficients  $\hat{\mathbf{u}}_k$  for representing the initial conditions specified at the time step  $t^n$ . To simplify the final form of the system of equations, the following notation was introduced:

$$\begin{aligned}
\hat{\mathbf{f}}_p^\xi &= \mathbf{f}_\xi(\hat{\mathbf{q}}_p); & \hat{\mathbf{f}}_p^\eta &= \mathbf{f}_\eta(\hat{\mathbf{q}}_p); & \hat{\mathbf{f}}_p^\zeta &= \mathbf{f}_\zeta(\hat{\mathbf{q}}_p); & \hat{\mathbf{s}}_p &= \mathbf{s}(\hat{\mathbf{q}}_p, \mathbf{r}(\boldsymbol{\xi}_p), t(\tau_p)), \\
\hat{\mathbf{b}}_p &= \sum_r \left( \mathfrak{B}_\xi(\hat{\mathbf{q}}_p) \frac{\partial \Theta_r(\tau_p, \boldsymbol{\xi}_p)}{\partial \xi} + \mathfrak{B}_\eta(\hat{\mathbf{q}}_p) \frac{\partial \Theta_r(\tau_p, \boldsymbol{\xi}_p)}{\partial \eta} + \mathfrak{B}_\zeta(\hat{\mathbf{q}}_p) \frac{\partial \Theta_r(\tau_p, \boldsymbol{\xi}_p)}{\partial \zeta} \right) \cdot \hat{\mathbf{q}}_r;
\end{aligned} \tag{17}$$

and notation for the matrices was also introduced:

$$\begin{aligned}
\mathbb{K}_{pq}^\tau &= [\Theta_p, \Theta_q](1) - \left\langle \frac{\partial \Theta_p}{\partial \tau}, \Theta_q \right\rangle; & \mathbb{M}_{pq} &= \langle \Theta_p, \Theta_q \rangle; & \mathbb{F}_{pk}^0 &= [\Theta_p, \Phi_k](0); \\
\mathbb{K}_{pq}^\xi &= \left\langle \Theta_p, \frac{\partial \Theta_q}{\partial \xi} \right\rangle; & \mathbb{K}_{pq}^\eta &= \left\langle \Theta_p, \frac{\partial \Theta_q}{\partial \eta} \right\rangle; & \mathbb{K}_{pq}^\zeta &= \left\langle \Theta_p, \frac{\partial \Theta_q}{\partial \zeta} \right\rangle;
\end{aligned} \tag{18}$$

where it is necessary to take into account that  $p = (p_0, p_1, p_2, p_3)$  and  $k = (k_1, k_2, k_3)$  are multi-indices for which a through index can be introduced (multi-indices  $q$  and  $r$  are similar in structure to  $p$ ):

$$\begin{aligned}
p &= p_0 \cdot (N+1)^3 + p_1 \cdot (N+1)^2 + p_2 \cdot (N+1) + p_3; & 0 &\leq p_0, p_1, p_2, p_3 \leq N; & 0 &\leq p \leq (N+1)^4; \\
k &= k_1 \cdot (N+1)^2 + k_2 \cdot (N+1) + k_3; & 0 &\leq k_1, k_2, k_3 \leq N; & 0 &\leq k \leq (N+1)^3.
\end{aligned} \tag{19}$$

In simplifying notation, the system of predictor equations can be rewritten in the following form:

$$\sum_q \left( \mathbb{K}_{pq}^\tau \hat{\mathbf{q}}_q + \mathbb{K}_{pq}^\xi \hat{\mathbf{f}}_q^\xi + \mathbb{K}_{pq}^\eta \hat{\mathbf{f}}_q^\eta + \mathbb{K}_{pq}^\zeta \hat{\mathbf{f}}_q^\zeta - \mathbb{M}_{pq} \left( \hat{\mathbf{s}}_q - \hat{\mathbf{b}}_q \right) \right) = \sum_k \mathbb{F}_{pk}^0 \hat{\mathbf{u}}_k, \tag{20}$$

which after multiplication on the left by the inverse matrix  $[\mathbb{K}^\tau]^{-1}$  takes the following form [40]:

$$\hat{\mathbf{q}}_p - \sum_q \mathbb{L}_{pq}^s \left( \hat{\mathbf{s}}_q - \hat{\mathbf{b}}_q \right) = \sum_k \mathbb{L}_{pk}^0 \hat{\mathbf{u}}_k - \sum_q \left( \mathbb{L}_{pq}^\xi \hat{\mathbf{f}}_q^\xi + \mathbb{L}_{pq}^\eta \hat{\mathbf{f}}_q^\eta + \mathbb{L}_{pq}^\zeta \hat{\mathbf{f}}_q^\zeta \right), \tag{21}$$

where the following notation is introduced:

$$\begin{aligned}
\mathbb{L}_{pq}^\xi &= \sum_r [\mathbb{K}^\tau]_{pr}^{-1} \mathbb{K}_{rq}^\xi, & \mathbb{L}_{pq}^\eta &= \sum_r [\mathbb{K}^\tau]_{pr}^{-1} \mathbb{K}_{rq}^\eta, & \mathbb{L}_{pq}^\zeta &= \sum_r [\mathbb{K}^\tau]_{pr}^{-1} \mathbb{K}_{rq}^\zeta, \\
\mathbb{L}_{pq}^\sigma &= \sum_r [\mathbb{K}^\tau]_{pr}^{-1} \mathbb{M}_{rq}, & \mathbb{L}_{pk}^0 &= \sum_r [\mathbb{K}^\tau]_{pr}^{-1} \mathbb{F}_{rk}.
\end{aligned} \tag{22}$$

The work [39] strictly proves that the eigenvalues of the matrices  $\mathbb{L}^\xi$ ,  $\mathbb{L}^\eta$  and  $\mathbb{L}^\zeta$  are zero, which was previously stated in [40]. Therefore, the Picard iterative process is of the following form:

$$\hat{\mathbf{q}}_p^{(l+1)} - \sum_q \mathbb{L}_{pq}^\sigma \left( \hat{\mathbf{s}}_q^{(l+1)} - \hat{\mathbf{b}}_q^{(l+1)} \right) = \sum_k \mathbb{L}_{pk}^0 \hat{\mathbf{u}}_k - \sum_q \left( \mathbb{L}_{pq}^\xi \hat{\mathbf{f}}_q^{\xi, (l)} + \mathbb{L}_{pq}^\eta \hat{\mathbf{f}}_q^{\eta, (l)} + \mathbb{L}_{pq}^\zeta \hat{\mathbf{f}}_q^{\zeta, (l)} \right), \tag{23}$$

and strictly converges to the solution of the problem in case of zero terms  $\mathbf{B} \equiv 0$  and  $\mathbf{S} \equiv 0$  in (1). The matrix  $\mathbb{L}^0$  has an interesting property:

$$\mathbb{L}_{pk}^0 \equiv \mathbb{L}_{p_0 p_1 p_2 p_3, k_1 k_2 k_3}^0 = \delta_{p_1 k_1} \delta_{p_2 k_2} \delta_{p_3 k_3}, \tag{24}$$

which is due to the fact that in case of zero fluxes  $\mathbb{F} \equiv 0$  and terms  $\mathbf{B} \equiv 0$  and  $\mathbf{S} \equiv 0$  in (1) the solution  $\mathbf{q}(\tau, \boldsymbol{\xi})$  is a constant in time  $\tau$ , therefore the condition  $\hat{\mathbf{q}}_{p_0 p_1 p_2 p_3} = \hat{\mathbf{u}}_{p_1 p_2 p_3}$  must be satisfied that is equivalent to the condition (24). This condition is applicable in software implementation – the calculation of the first term on the right side of the system of equations (23) is reduced to initializing each subarray  $\hat{\mathbf{q}}_{p_0}$  by array  $\hat{\mathbf{u}}$ .

## 2.2 Using the BLAS interface

The matrices (22) included in the system of nonlinear algebraic equations (23) of the LST-DG predictor can be expressed through the matrices of mass  $\Lambda$  and stiffness  $\Xi$  determined by the basis functions  $\{\varphi_k(\xi)\}$ :

$$\Lambda_{kl} = \int_0^1 \varphi_k \varphi_l d\xi = \Lambda_k \delta_{kl}; \quad \Xi_{kl} = \int_0^1 \varphi_k \frac{d\varphi_l}{d\xi} d\xi; \quad \Upsilon_{kl} = \varphi_k(1)\varphi_l(1) - \Xi_{lk}, \quad (25)$$

where the orthogonality property of the functional basis  $\varphi_k(\xi)$  is taken into account and an expression for the matrix  $\Upsilon$  is introduced. Using through indices  $p$  and  $q$  (19), the expressions (18) for the matrices are expressed as follows:

$$\begin{aligned} \mathbb{K}^\tau &= \Upsilon \otimes \Lambda \otimes \Lambda \otimes \Lambda; & \mathbb{M} &= \Lambda \otimes \Lambda \otimes \Lambda \otimes \Lambda; \\ \mathbb{K}^\xi &= \Lambda \otimes \Xi \otimes \Lambda \otimes \Lambda; & \mathbb{K}^\eta &= \Lambda \otimes \Lambda \otimes \Xi \otimes \Lambda; & \mathbb{K}^\zeta &= \Lambda \otimes \Lambda \otimes \Lambda \otimes \Xi, \end{aligned} \quad (26)$$

where  $\otimes$  denotes the Kronecker product. Using these expressions and introducing additional matrices  $\tilde{\mathbf{a}} = \Upsilon^{-1} \cdot \Lambda$  and  $\tilde{\mathbf{k}} = \Lambda^{-1} \cdot \Xi$ , expressions for the LST-DG predictor matrices (22) were obtained:

$$\begin{aligned} \mathbb{L}^\sigma &= [\Upsilon \otimes \Lambda \otimes \Lambda \otimes \Lambda]^{-1} \cdot [\Lambda \otimes \Lambda \otimes \Lambda \otimes \Lambda] = \tilde{\mathbf{a}} \otimes \mathbb{I} \otimes \mathbb{I} \otimes \mathbb{I}; \\ \mathbb{L}^\xi &= [\Upsilon \otimes \Lambda \otimes \Lambda \otimes \Lambda]^{-1} \cdot [\Lambda \otimes \Xi \otimes \Lambda \otimes \Lambda] = \tilde{\mathbf{a}} \otimes \tilde{\mathbf{k}} \otimes \mathbb{I} \otimes \mathbb{I}; \\ \mathbb{L}^\eta &= [\Upsilon \otimes \Lambda \otimes \Lambda \otimes \Lambda]^{-1} \cdot [\Lambda \otimes \Lambda \otimes \Xi \otimes \Lambda] = \tilde{\mathbf{a}} \otimes \mathbb{I} \otimes \tilde{\mathbf{k}} \otimes \mathbb{I}; \\ \mathbb{L}^\zeta &= [\Upsilon \otimes \Lambda \otimes \Lambda \otimes \Lambda]^{-1} \cdot [\Lambda \otimes \Lambda \otimes \Lambda \otimes \Xi] = \tilde{\mathbf{a}} \otimes \mathbb{I} \otimes \mathbb{I} \otimes \tilde{\mathbf{k}}, \end{aligned} \quad (27)$$

where  $\mathbb{I}$  is the  $(N+1) \times (N+1)$  identity matrix. Calculation of non-conservative terms  $\hat{\mathbf{b}}_q$  uses multiplication by gradient matrices for basis functions  $\Theta_p$ :

$$\mathbb{D}_{pq}^\xi = \frac{\partial \Theta_q(\tau_p, \boldsymbol{\xi}_p)}{\partial \xi}; \quad \mathbb{D}_{pq}^\eta = \frac{\partial \Theta_q(\tau_p, \boldsymbol{\xi}_p)}{\partial \eta}; \quad \mathbb{D}_{pq}^\zeta = \frac{\partial \Theta_q(\tau_p, \boldsymbol{\xi}_p)}{\partial \zeta}, \quad (28)$$

for which the following representations were obtained:

$$\mathbb{D}^\xi = \mathbb{I} \otimes [\mathbb{D}^\varphi]^T \otimes \mathbb{I} \otimes \mathbb{I}; \quad \mathbb{D}^\eta = \mathbb{I} \otimes \mathbb{I} \otimes [\mathbb{D}^\varphi]^T \otimes \mathbb{I}; \quad \mathbb{D}^\zeta = \mathbb{I} \otimes \mathbb{I} \otimes \mathbb{I} \otimes [\mathbb{D}^\varphi]^T, \quad (29)$$

where  $\mathbb{D}^\varphi = \|\varphi'_k(\xi_l)\|$  is the  $(N+1) \times (N+1)$  matrix of derivatives of the basis functions  $\varphi_k(\xi)$  in nodes  $\xi_l$ .

Table 1: The main parameters of the BLAS procedures `gemm` used to calculate the discrete solution  $\mathbf{q}$  by the LST-DG predictor.

kernel name	$m$	$n$	$k$	lda	ldb	ldc	$\alpha$	$\beta$
<code>k_ksi_kernel</code>	$N+1$	$M$	$N+1$	$N+1$	$(N+1)^2 M$	$(N+1)^2 M$	1	0
<code>k_eta_kernel</code>	$N+1$	$M$	$N+1$	$N+1$	$(N+1)M$	$(N+1)M$	1	1
<code>k_zeta_kernel</code>	$N+1$	$M$	$N+1$	$N+1$	$M$	$M$	1	1
<code>kappa_kernel</code>	$N+1$	$M$	$N+1$	$N+1$	$(N+1)^3 M$	$(N+1)^3 M$	1	1
<code>d_ksi_kernel</code>	$N+1$	$M$	$N+1$	$N+1$	$(N+1)^2 M$	$(N+1)^2 M$	1	0
<code>d_eta_kernel</code>	$N+1$	$M$	$N+1$	$N+1$	$(N+1)M$	$(N+1)M$	1	0
<code>d_zeta_kernel</code>	$N+1$	$M$	$N+1$	$N+1$	$M$	$M$	1	0
<code>b_ksi_kernel</code>	$M$	$M$	$M$	$M$	$M$	$M$	1	0
<code>b_eta_kernel</code>	$M$	$M$	$M$	$M$	$M$	$M$	1	1
<code>b_zeta_kernel</code>	$M$	$M$	$M$	$M$	$M$	$M$	1	1

The choice and implementation of a numerical method for solving the system (23) of nonlinear algebraic equations of the LST-DG predictor can be based on the Picard method and the Newton method [39]. The work [39] notes that the solution of the system of nonlinear algebraic equations of the predictor in the case of the presence of stiff terms is preferably performed using Newton's method. This work proposes an implementation of the Picard iterative method for solving a system of equations (23), which is organized in the form of two nested Picard iterative processes:

$$\hat{\mathbf{q}}_p^{(l+1, m+1)} = \sum_q \mathbb{L}_{pq}^\sigma \left( \hat{\mathbf{s}}_q^{(l+1, m)} - \hat{\mathbf{b}}_q^{(l+1, m)} \right) + \sum_k \mathbb{L}_{pk}^0 \hat{\mathbf{u}}_k - \sum_q \left( \mathbb{L}_{pq}^\xi \hat{\mathbf{f}}_q^{\xi, (l, m)} + \mathbb{L}_{pq}^\eta \hat{\mathbf{f}}_q^{\eta, (l, m)} + \mathbb{L}_{pq}^\zeta \hat{\mathbf{f}}_q^{\zeta, (l, m)} \right), \quad (30)$$

where in the internal iterative process on index  $m$  convergence is achieved for the stiff terms associated with algebraic sources and non-conservative terms, and in the external iterative process on index  $l$  a general convergence is achieved, associated with flux terms. Further in the text of the work, a method of use of the BLAS interface to implement a LST-DG predictor of this form is presented. Taking into account the recommendations of the work [39], it can be added that the internal iterative process can be implemented using Newton method, rather than Picard method, in the case of the presence of stiff source terms in the system of equations.

All terms in the expression (30) were calculated using the `gemm` function of the BLAS interface. The main parameters of the standard function `gemm` determine the storage method – `layout`, operations with matrices – `transa` and `transb`, matrices sizes  $n$ ,  $m$  and  $k$ , leading dimensions `lda`, `ldb` and `lds`, and the factors  $\alpha$  and  $\beta$ . The `row-major` layout for storing matrices was chosen, and `notrans` was selected for the operations `transa` and `transb`. The values of all parameters used are presented in Table 1. The last two lines of Table 1 are the same, which is done for reasons of syntactically clear introduction of

---

**Algorithm 1** The basic general structure of using BLAS interface procedure calls in the implementation of the LST-DG predictor.

---

```

1: q_init, q_prev, q_next, kf_sum, q_int_prev, q_int_next, s, d: array $[(N + 1)^4 \cdot M]$ 
2: s_args: array $[4 \cdot (N + 1)^4]$ 
3: function GET_CELL_LOCAL_SOLUTION(u_prev)
4:   for all  $p_0 \in [0, N]$  do
5:     q_init $[p_0] \leftarrow \mathbf{u\_prev}$ 
6:   end for
7:   q_prev  $\leftarrow$  INIT_ITER(q_init, dt_div_dr)
8:   repeat
9:     q_next  $\leftarrow$  q_init ▷ added only for symmetry
10:    SET_FLUX_TERMS_SUM(kf_sum)
11:    q_int_prev  $\leftarrow$  q_prev
12:    repeat
13:      q_int_next  $\leftarrow$  q_init
14:      for all  $(p_0, p_1, p_2, p_3) \in [0, N]^4$  do
15:        idx  $\leftarrow (p_0 \cdot (N + 1)^3 + p_1 \cdot (N + 1)^2 + p_2 \cdot (N + 1) + p_3) \cdot M$ 
16:        SET_RESCALED_SOURCE_TERMS(s $[\mathbf{idx}]$ , q_int_prev $[\mathbf{idx}]$ , s_args $[\mathbf{idx}]$ , dt)
17:      end for
18:      SET_NON_CONSERVATIVE_TERMS_SUM(b, q_int_prev, dt_div_dr)
19:      s  $\leftarrow \mathbf{s} - \mathbf{b} - \mathbf{kf\_sum}$ 
20:      for all  $(p_1, p_2, p_3) \in [0, N]^3$  do
21:        idx  $\leftarrow (p_1 \cdot (N + 1)^2 + p_2 \cdot (N + 1) + p_3) \cdot M$ 
22:        KAPPA_KERNEL(q_int_next $[\mathbf{idx}]$ , kappa_tilde, s $[\mathbf{idx}]$ )
23:      end for
24:       $\varepsilon_{\text{inner}} \leftarrow \|\mathbf{q\_int\_next} - \mathbf{q\_int\_prev}\|$ 
25:      q_int_prev  $\leftarrow$  q_int_next
26:    until  $\varepsilon_{\text{inner}} \leq \varepsilon_0$ 
27:    q_next  $\leftarrow$  q_int_next
28:     $\varepsilon_{\text{outer}} \leftarrow \|\mathbf{q\_next} - \mathbf{q\_prev}\|$ 
29:    q_prev  $\leftarrow$  q_next
30:  until  $\varepsilon_{\text{outer}} \leq \varepsilon_0$ 
31:  return q_next
32: end function

```

---

**Algorithm 2** Procedure to Algorithm 1 for calculating the sum of flux terms multiplied by matrices  $\mathbb{L}^\xi$ ,  $\mathbb{L}^\eta$ ,  $\mathbb{L}^\zeta$ .

---

```

1: f_ksi, f_eta, f_zeta, kf_sum, q_prev: array $[(N + 1)^4 \cdot M]$ 
2: procedure SET_FLUX_TERMS_SUM(kf_sum, q_prev, dt_div_dr)
3:   for all  $(p_0, p_1, p_2, p_3) \in [0, N]^4$  do
4:     idx  $\leftarrow (p_0 \cdot (N + 1)^3 + p_1 \cdot (N + 1)^2 + p_2 \cdot (N + 1) + p_3) \cdot M$ 
5:     SET_RESCALED_FLUX_TERMS_3D(f_ksi $[\mathbf{idx}]$ , f_eta $[\mathbf{idx}]$ , f_zeta $[\mathbf{idx}]$ , q_prev $[\mathbf{idx}]$ , dt_div_dr)
6:   end for
7:   for all  $(p_0, p_2, p_3) \in [0, N]^3$  do
8:     idx  $\leftarrow (p_0 \cdot (N + 1)^3 + p_2 \cdot (N + 1) + p_3) \cdot M$ 
9:     K_KSL_KERNEL(kf_sum $[\mathbf{idx}]$ , k_tilde, f_ksi $[\mathbf{idx}]$ )
10:  end for
11:  for all  $(p_0, p_1, p_3) \in [0, N]^3$  do
12:    idx  $\leftarrow (p_0 \cdot (N + 1)^3 + p_1 \cdot (N + 1)^2 + p_3) \cdot M$ 
13:    K_ETA_KERNEL(kf_sum $[\mathbf{idx}]$ , k_tilde, f_eta $[\mathbf{idx}]$ )
14:  end for
15:  for all  $(p_0, p_1, p_2) \in [0, N]^3$  do
16:    idx  $\leftarrow (p_0 \cdot (N + 1)^3 + p_1 \cdot (N + 1)^2 + p_2 \cdot (N + 1)) \cdot M$ 
17:    K_ZETA_KERNEL(kf_sum $[\mathbf{idx}]$ , k_tilde, f_zeta $[\mathbf{idx}]$ )
18:  end for
19: end procedure

```

---

functions **b\_kernel** for each individual direction **ksi**, **eta** and **zeta** (in software implementation this can be an alias, if this is important). The basic general structure of the algorithm for calculating the expansion coefficients  $\mathbf{q}_p$  of a local discrete solution is presented in Algorithm 1, where, to simplify the pseudocode, two support procedures were designed separately, presented in Algorithm 2 and Algorithm 3. Algorithm 1 receives as input an array of coefficients **u**, as well as the time step  $\Delta t$  and coordinate steps  $(\Delta x, \Delta y, \Delta z)$  (as  $(\Delta t/\Delta x, \Delta t/\Delta y, \Delta t/\Delta z)$  ratios). The procedures **set\_rescaled\_flux\_terms\_3d**, **set\_rescaled\_non\_conservative\_matrices** and **set\_rescaled\_source\_terms** calculate fluxes, source terms, and matrices of non-conservative terms, respectively, calculated immediately in rescaled variables. The matrices **k\_tilde**, **kappa\_tilde**, **D\_trans** used

---

**Algorithm 3** Procedure to Algorithm 1 for calculating the sum of non-conservative terms  $\hat{\mathbf{b}}_p$ .

---

```

1: b, q_int_prev, dq_ksi, dq_eta, dq_zeta: array $[(N + 1)^4 \cdot M]$ 
2: B_ksi, B_eta, B_zeta: array $[M^2]$ 
3: procedure SET_NON_CONSERVATIVE_TERMS_SUM(b, q_int_prev, dt_div_dr)
4:   for all  $(p_0, p_2, p_3) \in [0, N]^3$  do
5:     idx  $\leftarrow (p_0 \cdot (N + 1)^3 + p_2 \cdot (N + 1) + p_3) \cdot M$ 
6:     D_KSL_KERNEL(dq_ksi[idx], D_trans, q_int_prev[idx])
7:   end for
8:   for all  $(p_0, p_1, p_3) \in [0, N]^3$  do
9:     idx  $\leftarrow (p_0 \cdot (N + 1)^3 + p_1 \cdot (N + 1)^2 + p_3) \cdot M$ 
10:    D_ETA_KERNEL(dq_eta[idx], D_trans, q_int_prev[idx])
11:  end for
12:  for all  $(p_0, p_1, p_2) \in [0, N]^3$  do
13:    idx  $\leftarrow (p_0 \cdot (N + 1)^3 + p_1 \cdot (N + 1)^2 + p_2 \cdot (N + 1)) \cdot M$ 
14:    D_ZETA_KERNEL(dq_zeta[idx], D_trans, q_int_prev[idx])
15:  end for
16:  for all  $(p_0, p_1, p_2, p_3) \in [0, N]^4$  do
17:    idx  $\leftarrow (p_0 \cdot (N + 1)^3 + p_1 \cdot (N + 1)^2 + p_2 \cdot (N + 1) + p_3) \cdot M$ 
18:    SET_RESCALED_NON_CONSERVATIVE_MATRICES(B_ksi, B_eta, B_zeta, q_int_prev[idx], dt_div_dr)
19:    B_KSL_KERNEL(b[idx], B_ksi, dq_ksi[idx])
20:    B_ETA_KERNEL(b[idx], B_eta, dq_eta[idx])
21:    B_ZETA_KERNEL(b[idx], B_zeta, dq_zeta[idx])
22:  end for
23: end procedure

```

---

for calculations are corresponded to matrices  $\tilde{k}$ ,  $\tilde{\alpha}$ ,  $[\mathbb{D}^\varphi]^T$  and are pre-computed. Array **s\_args** stores the values  $(t(\tau_p), \mathbf{r}(\boldsymbol{\xi})_p)$  for each cell, with the values  $t(\tau_p)$  being recalculated for each time step. The function **init\_iter** can use simple initialization  $\hat{\mathbf{q}}_{p_0 p_1 p_2 p_3} = \hat{\mathbf{u}}_{p_1 p_2 p_3}$ , based on property (24), or more advanced methods for obtaining initial iterations of the solution [16]. Internal and external iterations are implemented in loops, the exit conditions of which are determined by decreasing the error  $\varepsilon$  to a value of  $\varepsilon_0$ , which was chosen equal to  $10^{-12}$ - $10^{-14}$  for the case of using floating point numbers type **double** and  $10^{-4}$ - $10^{-6}$  – for type **float**. The pseudocode of Algorithm 1 does not provide any methods for error handling and infinite loop protection of the iterative process. In a real software implementation, the number of iterations is limited to 100-1000; and in case of an incorrect result, the program is aborted if the error cannot be processed, or the output solution is filled by **nan**, which can then be processed, for example, by a posteriori correction of the solution. It should be noted that all parameters of the **gemm** functions are known in advance and are constants, except for the arrays used. Therefore, this implementation satisfies all the requirements for the use of JIT functions for small matrices computations, in particular, the **jit gemm** from the Intel MKL library.

The similar implementation was proposed and discussed in the work [16]. However, the method of use of the BLAS interface proposed in the work [16] involves application of complex additional procedures associated with the calculation of flux, source and non-conservative terms. In general, the local discrete solution  $\mathbf{q}(\tau, \boldsymbol{\xi})$  is represented as an expansion (6) in basis functions with expansion coefficients  $\mathbf{q}_p$ . Each expansion coefficient  $\mathbf{q}_p$  is an array of  $M$  elements. Then a method for 5d array storage should be chosen. If we choose conserved variables as an index  $r$  of an element of a homogeneous structure, then storage in format  $\mathbf{q}_{p_0 p_1 p_2 p_3, r}$  is AoS, and in format  $\mathbf{q}_{r, p_0 p_1 p_2 p_3}$  is SoA, which is the classic AoS vs SoA problem, known in computer science. In the works [16, 19] the use of SoA is proposed, which allows the use of small matrices, well suited for the **lixsmm** library of small matrices computations. However, this choice requires complicated calculations of flux, source and non-conservative terms – direct calculation requires transposing the matrices  $\mathbf{q}_{r, p} \mapsto \mathbf{q}_{p, r}$ . This work proposes an approach different from that proposed in the works [16, 19]. The proposed approach immediately operates on AoS  $\mathbf{q}_{p, r}$ , which makes it possible to efficiently calculate flux, source and non-conservative terms. This approach simply scales in case of large values of  $M$ , which is typical for problems of simulating multicomponent reacting flows, in which the number of components can be large, as well as problems for simulating dynamic problems of general relativity, in particular within the framework of the conformal and covariant Z4 formalism [13–15], where the value of  $M = 47$ .

## 3 ADER-DG method

### 3.1 General description

The one-step discrete ADER-DG scheme is obtained using the condition of zero  $L_2$  projection in reference space-time element  $\omega_4$  of the residual (4) onto the test functions  $\Phi_k(\boldsymbol{\xi})$  [6, 8–11, 16]:

$$\left\langle \Phi_k, \frac{\partial \mathbf{u}}{\partial \tau} + \frac{\partial \mathbf{f}_\xi(\mathbf{u})}{\partial \xi} + \frac{\partial \mathbf{f}_\eta(\mathbf{u})}{\partial \eta} + \frac{\partial \mathbf{f}_\zeta(\mathbf{u})}{\partial \zeta} + \mathfrak{B}_\xi(\mathbf{u}) \cdot \frac{\partial \mathbf{u}}{\partial \xi} + \mathfrak{B}_\eta(\mathbf{u}) \cdot \frac{\partial \mathbf{u}}{\partial \eta} + \mathfrak{B}_\zeta(\mathbf{u}) \cdot \frac{\partial \mathbf{u}}{\partial \zeta} - \mathbf{s}(\mathbf{u}, \mathbf{r}(\boldsymbol{\xi}), t(\tau)) \right\rangle = 0, \quad (31)$$

where integration by parts was carried out with the selection of complete divergence in the flux terms, substitution of the DG representation (7)  $\mathbf{u}^n$  and  $\mathbf{u}^{n+1}$  in the time term and the discrete solution  $\mathbf{q}$  (6) instead of  $\mathbf{u}$  in the integral expressions, which led to an expression of the form:

$$\begin{aligned}
& \sum_l \langle \Phi_k, \Phi_l \rangle (\mathbf{u}_l^{n+1} - \mathbf{u}_l^n) + \left\{ \Phi_k, \mathfrak{G}(\mathbf{q}^{(-)}, \mathbf{q}^{(+)}) \right\} - \left( \left\langle \frac{\partial \Phi_k}{\partial \xi}, \mathbf{f}_\xi(\mathbf{q}) \right\rangle + \left\langle \frac{\partial \Phi_k}{\partial \eta}, \mathbf{f}_\eta(\mathbf{q}) \right\rangle + \left\langle \frac{\partial \Phi_k}{\partial \zeta}, \mathbf{f}_\zeta(\mathbf{q}) \right\rangle \right) \\
& + \left( \left\langle \Phi_k, \mathfrak{B}_\xi(\mathbf{q}) \cdot \frac{\partial \mathbf{q}}{\partial \xi} \right\rangle + \left\langle \Phi_k, \mathfrak{B}_\eta(\mathbf{q}) \cdot \frac{\partial \mathbf{q}}{\partial \eta} \right\rangle + \left\langle \Phi_k, \mathfrak{B}_\zeta(\mathbf{q}) \cdot \frac{\partial \mathbf{q}}{\partial \zeta} \right\rangle \right) \\
& = \langle \Phi_k, \mathbf{s}(\mathbf{q}, \mathbf{r}(\boldsymbol{\xi}), t(\tau)) \rangle,
\end{aligned} \tag{32}$$

where,  $\mathfrak{G} = (\mathfrak{G}_\xi, \mathfrak{G}_\eta, \mathfrak{G}_\zeta)$  is the Riemann solver, taking into account non-conservative terms in the system of equations and expressed in the rescaled coordinate system (3) of the reference space-time element  $\omega_4$ ,  $\mathbf{q}^{(-)}$  and  $\mathbf{q}^{(+)}$  are the local discrete solutions in cells in the outer normal direction  $\mathbf{n}$  of the cell  $\Omega_i$  and in the opposite direction, and the notation for the integral operator is introduced for simplicity:

$$\begin{aligned}
\{f(\tau, \boldsymbol{\xi}), \mathbf{g}(\tau, \boldsymbol{\xi})\} &= \int_0^1 d\tau \oint_{\partial\omega_3} dS_\xi \cdot f(\tau, \boldsymbol{\xi}) \mathbf{g}(\tau, \boldsymbol{\xi}) \cdot \mathbf{n} \\
&= \int_0^1 d\tau \int_0^1 d\eta \int_0^1 d\zeta \cdot (f(\tau, 1, \eta, \zeta) g_\xi(\tau, 1, \eta, \zeta) - f(\tau, 0, \eta, \zeta) g_\xi(\tau, 0, \eta, \zeta)) \\
&+ \int_0^1 d\tau \int_0^1 d\xi \int_0^1 d\zeta \cdot (f(\tau, \xi, 1, \zeta) g_\eta(\tau, \xi, 1, \zeta) - f(\tau, \xi, 0, \zeta) g_\eta(\tau, \xi, 0, \zeta)) \\
&+ \int_0^1 d\tau \int_0^1 d\xi \int_0^1 d\eta \cdot (f(\tau, \xi, \eta, 1) g_\zeta(\tau, \xi, \eta, 1) - f(\tau, \xi, \eta, 0) g_\zeta(\tau, \xi, \eta, 0)),
\end{aligned} \tag{33}$$

where  $\mathbf{g} = (g_\xi, g_\eta, g_\zeta)$  is a vector field. Substituting the representation (6) of the discrete solution  $\mathbf{q}$  into the resulting expression for the ADER-DG scheme and using the Gauss-Legendre quadrature formulas (12) used in case of the selected set of nodal basis functions  $\varphi_k(\boldsymbol{\xi})$  leads to the following expression:

$$\begin{aligned}
& w_{k_1} w_{k_2} w_{k_3} (\mathbf{u}_{k_1 k_2 k_3}^{n+1} - \mathbf{u}_{k_1 k_2 k_3}^n) \\
&= \sum_{l_0=0}^N w_{l_0} \left[ \sum_{l_1=0}^N w_{l_1} w_{k_2} w_{k_3} \mathbb{D}_{k_1 l_1}^\varphi \mathbf{f}_\xi(\hat{\mathbf{q}}_{l_0 l_1 k_2 k_3}) + \sum_{l_2=0}^N w_{k_1} w_{l_2} w_{k_3} \mathbb{D}_{k_2 l_2}^\varphi \mathbf{f}_\eta(\hat{\mathbf{q}}_{l_0 k_1 l_2 k_3}) + \sum_{l_3=0}^N w_{k_1} w_{k_2} w_{l_3} \mathbb{D}_{k_3 l_3}^\varphi \mathbf{f}_\zeta(\hat{\mathbf{q}}_{l_0 k_1 k_2 l_3}) \right] \\
&- \sum_{l_0=0}^N w_{l_0} w_{k_2} w_{k_3} \left[ \tilde{\psi}_{k_1} \mathfrak{G}_\xi \left( \sum_{p_1=0}^N \tilde{\psi}_{p_1} \hat{\mathbf{q}}_{l_0 p_1 k_2 k_3}, \sum_{p_1=0}^N \psi_{p_1} \hat{\mathbf{q}}_{l_0 p_1 k_2 k_3}^{(R, \xi)} \right) - \psi_{k_1} \mathfrak{G}_\xi \left( \sum_{p_1=0}^N \tilde{\psi}_{p_1} \hat{\mathbf{q}}_{l_0 p_1 k_2 k_3}^{(L, \xi)}, \sum_{p_1=0}^N \psi_{p_1} \hat{\mathbf{q}}_{l_0 p_1 k_2 k_3} \right) \right] \\
&- \sum_{l_0=0}^N w_{l_0} w_{k_1} w_{k_3} \left[ \tilde{\psi}_{k_2} \mathfrak{G}_\eta \left( \sum_{p_2=0}^N \tilde{\psi}_{p_2} \hat{\mathbf{q}}_{l_0 k_1 p_2 k_3}, \sum_{p_2=0}^N \psi_{p_2} \hat{\mathbf{q}}_{l_0 k_1 p_2 k_3}^{(R, \eta)} \right) - \psi_{k_2} \mathfrak{G}_\eta \left( \sum_{p_2=0}^N \tilde{\psi}_{p_2} \hat{\mathbf{q}}_{l_0 k_1 p_2 k_3}^{(L, \eta)}, \sum_{p_2=0}^N \psi_{p_2} \hat{\mathbf{q}}_{l_0 k_1 p_2 k_3} \right) \right] \\
&- \sum_{l_0=0}^N w_{l_0} w_{k_1} w_{k_2} \left[ \tilde{\psi}_{k_3} \mathfrak{G}_\zeta \left( \sum_{p_3=0}^N \tilde{\psi}_{p_3} \hat{\mathbf{q}}_{l_0 k_1 k_2 p_3}, \sum_{p_3=0}^N \psi_{p_3} \hat{\mathbf{q}}_{l_0 k_1 k_2 p_3}^{(R, \zeta)} \right) - \psi_{k_3} \mathfrak{G}_\zeta \left( \sum_{p_3=0}^N \tilde{\psi}_{p_3} \hat{\mathbf{q}}_{l_0 k_1 k_2 p_3}^{(L, \zeta)}, \sum_{p_3=0}^N \psi_{p_3} \hat{\mathbf{q}}_{l_0 k_1 k_2 p_3} \right) \right] \\
&- \sum_{l_0=0}^N w_{l_0} w_{k_1} w_{k_2} w_{k_3} \left[ \mathfrak{B}_\xi(\hat{\mathbf{q}}_{l_0 k_1 k_2 k_3}) \sum_{r_1=0}^N \mathbb{D}_{r_1 k_1}^\varphi \hat{\mathbf{q}}_{l_0 r_1 k_2 k_3} + \mathfrak{B}_\eta(\hat{\mathbf{q}}_{l_0 k_1 k_2 k_3}) \sum_{r_2=0}^N \mathbb{D}_{r_2 k_2}^\varphi \hat{\mathbf{q}}_{l_0 k_1 r_2 k_3} \right. \\
&\quad \left. + \mathfrak{B}_\zeta(\hat{\mathbf{q}}_{l_0 k_1 k_2 k_3}) \sum_{r_3=0}^N \mathbb{D}_{r_3 k_3}^\varphi \hat{\mathbf{q}}_{l_0 k_1 k_2 r_3} - \mathbf{s}(\hat{\mathbf{q}}_{l_0 k_1 k_2 k_3}, \mathbf{r}(\boldsymbol{\xi}_{k_1 k_2 k_3}), t(\tau_{l_0})) \right],
\end{aligned} \tag{34}$$

where  $\psi_k = \varphi_k(0)$ ,  $\tilde{\psi}_k = \varphi_k(1)$ , and upper indices  $(L, \xi)$ ,  $(L, \eta)$ ,  $(L, \zeta)$  and  $(R, \xi)$ ,  $(R, \eta)$ ,  $(R, \zeta)$  denote the discrete space-time solution  $\mathbf{q}$  in the left and right cells with respect to the selected cell in directions  $\xi$ ,  $\eta$  and  $\zeta$ , respectively.

---

**Algorithm 4** The basic general structure of using BLAS interface procedure calls in the implementation of the one-step discrete ADER-DG scheme.

---

```

1: function GET_DG_SOLUTION(u_prev)
2:   u_next  $\leftarrow$  u_prev
3:   UPDATE_VOLUME_TERMS(u_next)
4:   UPDATE_INTERFACE_TERMS(u_next)
5:   return u_next
6: end function

```

---

### 3.2 Using the BLAS interface

The resulting expression (34) for the one-step discrete ADER-DG scheme contained basic linear algebra operations, which are implemented using the BLAS interface. The general paradigm for data storage and using the matrix-matrix multiplication operation was chosen in a form similar to the implementation of the LST-DG predictor, which is presented in Subsection 2.2. Only the `gemm` procedure of the 3rd level of the BLAS interface was used. In this case, only the row major data storage format was



Table 2: The main parameters of the BLAS procedures `gemm` used in the one-step discrete ADER-DG scheme.

kernel name	$m$	$n$	$k$	lda	ldb	ldc	$\alpha$	$\beta$
<code>interface::psi_ksi_conv_kernel</code>	1	$M$	$N + 1$	$N + 1$	$(N + 1)^2 M$	$M$	1	0
<code>interface::psi_eta_conv_kernel</code>	1	$M$	$N + 1$	$N + 1$	$(N + 1)M$	$M$	1	0
<code>interface::psi_zeta_conv_kernel</code>	1	$M$	$N + 1$	$N + 1$	$M$	$M$	1	0
<code>interface::w_conv_kernel</code>	1	$M$	$N + 1$	$N + 1$	$(N + 1)^2 M$	$M$	1	0
<code>volume::w_conv_kernel</code>	1	$M$	$N + 1$	$N + 1$	$(N + 1)^3 M$	$(N + 1)^2 M$	1	0
<code>volume::d_tilde_f_ksi_kernel</code>	$N + 1$	$M$	$N + 1$	$N + 1$	$(N + 1)^2 M$	$(N + 1)^2 M$	1	0
<code>volume::d_tilde_f_eta_kernel</code>	$N + 1$	$M$	$N + 1$	$N + 1$	$(N + 1)M$	$(N + 1)M$	1	0
<code>volume::d_tilde_f_zeta_kernel</code>	$N + 1$	$M$	$N + 1$	$N + 1$	$M$	$M$	1	0
<code>volume::d_q_ksi_kernel</code>	$N + 1$	$M$	$N + 1$	$N + 1$	$(N + 1)^2 M$	$(N + 1)^2 M$	1	0
<code>volume::d_q_eta_kernel</code>	$N + 1$	$M$	$N + 1$	$N + 1$	$(N + 1)M$	$(N + 1)M$	1	0
<code>volume::d_q_zeta_kernel</code>	$N + 1$	$M$	$N + 1$	$N + 1$	$M$	$M$	1	0
<code>volume::b_ksi_kernel</code>	$M$	$M$	$M$	$M$	$M$	$M$	1	0
<code>volume::b_eta_kernel</code>	$M$	$M$	$M$	$M$	$M$	$M$	1	1
<code>volume::b_zeta_kernel</code>	$M$	$M$	$M$	$M$	$M$	$M$	1	1

used. Table 2 presents the main parameters of all `gemm` procedures used. Algorithm 4 presents the general form of the algorithm for calculating the solution `u_next` at the next time step  $t^{n+1}$ , while the calculation of the solution is separated into two main procedures presented in Algorithms 5 and 6, as well as in an additional procedures in Algorithm 7 for computing the interface flux terms `f_rp_ksi_interface`, `f_rp_eta_interface`, `f_rp_zeta_interface`. The calculation of interface flux terms is carried out in three separate procedures `set_interfaces_terms_ksi`, `set_interfaces_terms_eta` and `set_interfaces_terms_zeta`, which is associated with the use of Cartesian meshes – each interface contains terms only for the projection orthogonal to its plane; therefore, for each mesh interface one does not need to call all three procedures, just one is enough. It should be noted that the parameters of the procedures `d_q_ksi_kernel`, `d_q_eta_kernel` and `d_q_zeta_kernel` in Table 2 from the name space `volume` are identical to the parameters procedures `d_tilde_f_ksi_kernel`, `d_tilde_f_eta_kernel` and `d_tilde_f_zeta_kernel`, which is associated with the same sizes of matrices and leading dimensions; however, the calculation of non-conservative terms requires the use of a transposed matrix  $[\mathbb{D}^\varphi]^T$ , which can be implemented by the parameter `transa=trans`, or by storing two pre-computed matrices – the original  $\mathbb{D}^\varphi$  and the transposed  $[\mathbb{D}^\varphi]^T$ ; in the implementation presented in Algorithm 5, the method with the transposed matrix  $[\mathbb{D}^\varphi]^T$  is used. The `D.tilde` matrix used in Algorithm 5 contains elements  $w_l \mathbb{D}_{kl}^\varphi$ , which is convenient according to the expression (34). Matrices `psi_1`, `psi_2` and `w` contain values  $\psi_k$ ,  $\psi_k$  and  $w_k$ . The procedures `rs_rescaled_flux_ksi`, `rs_rescaled_flux_eta` and `rs_rescaled_flux_zeta` calculate the solution to the Riemann problem, where fluxes expressed immediately in the rescaled variables, for which the values `dt.div.dx`, `dt.div.dy` and `dt.div.dz` are passed as formal parameters to procedures. Procedure `volume::set_non_conservative_terms_sum`, responsible for calculating non-conservative terms, is structured similarly to the procedure presented in Algorithm 3 for the LST-DG predictor – matrix calculations are performed using the procedures `d_q_ksi_kernel`, `d_q_eta_kernel` and `d_q_zeta_kernel` from the name space `volume`. In general, the presented implementation allows the solution  $\mathbf{u}^{n+1}$  to be computed at the next time step  $t^{n+1}$  using BLAS interface procedures, without the use of transpose  $\mathbf{q}_{r,p} \mapsto \mathbf{q}_{p,r}$  [16]. The parameters of the procedure are known in advance, so the proposed approach is well suited to the use of JIT functions available in modern implementations of the BLAS interface for calculations with small matrices.

## 4 ADER-WENO-FV method

### 4.1 General description

The one-step discrete finite-volume ADER-WENO scheme is obtained by integrating the system of equations (4) over the reference space-time element  $\omega_4$ , which is technically equivalent to the  $L_2$  projection onto “test function” 1, resulting in the following expression [8, 9, 16]:

$$\left\langle \frac{\partial \mathbf{u}}{\partial \tau} + \frac{\partial \mathbf{f}_\xi(\mathbf{u})}{\partial \xi} + \frac{\partial \mathbf{f}_\eta(\mathbf{u})}{\partial \eta} + \frac{\partial \mathbf{f}_\zeta(\mathbf{u})}{\partial \zeta} + \mathfrak{B}_\xi(\mathbf{u}) \cdot \frac{\partial \mathbf{u}}{\partial \xi} + \mathfrak{B}_\eta(\mathbf{u}) \cdot \frac{\partial \mathbf{u}}{\partial \eta} + \mathfrak{B}_\zeta(\mathbf{u}) \cdot \frac{\partial \mathbf{u}}{\partial \zeta} - \mathbf{s}(\mathbf{u}, \mathbf{r}(\boldsymbol{\xi}), t(\tau)) \right\rangle = 0, \quad (35)$$

where  $\langle \cdot \rangle \equiv \langle 1, \cdot \rangle$ . The substitution of the finite-volume average values (8)  $\mathbf{v}^n$  and  $\mathbf{v}^{n+1}$  in the time term and the discrete solution  $\mathbf{q}$  (6) instead of  $\mathbf{u}$  in the integrals which leads to an expression of the form:

$$\mathbf{v}^{n+1} = \mathbf{v}^n - \left\{ \mathfrak{G}(\mathbf{q}^{(-)}, \mathbf{q}^{(+)}) \right\} - \left( \left\langle \mathfrak{B}_\xi(\mathbf{q}) \cdot \frac{\partial \mathbf{q}}{\partial \xi} \right\rangle + \left\langle \mathfrak{B}_\eta(\mathbf{q}) \cdot \frac{\partial \mathbf{q}}{\partial \eta} \right\rangle + \left\langle \mathfrak{B}_\zeta(\mathbf{q}) \cdot \frac{\partial \mathbf{q}}{\partial \zeta} \right\rangle \right) + \langle \mathbf{s}(\mathbf{q}, \mathbf{r}(\boldsymbol{\xi}), t(\tau)) \rangle, \quad (36)$$

where  $\mathfrak{G} = (\mathfrak{G}_\xi, \mathfrak{G}_\eta, \mathfrak{G}_\zeta)$  is the Riemann solver, taking into account non-conservative terms in the system of equations and expressed in the rescaled coordinate system (3) of the reference space-time element  $\omega_4$ ,  $\mathbf{q}^{(+)}$  and  $\mathbf{q}^{(-)}$  are the local discrete solutions in cells in the outer normal direction  $\mathbf{n}$  of the cell  $\Omega_i$  and in the opposite direction, and  $\{ \cdot \} = \{ 1, \cdot \}$ .

Substituting the representation (6) of the discrete solution  $\mathbf{q}$  into the resulting expression for the ADER-DG scheme and using the Gauss-Legendre quadrature formulas (12) used in case of the selected set of nodal basis functions  $\varphi_k(\boldsymbol{\xi})$  leads to the

**Algorithm 5** Procedure to Algorithm 4 responsible for calculating the contributions from the volume terms in the expression (34) and updating them to the preliminary solution `u_next_upd` at a next time step  $t^{n+1}$ .

```

1: f_ksi, f_eta, f_zeta, s, b: array[(N + 1)4 · M]
2: w_conv_f_ksi, w_conv_f_eta, w_conv_f_zeta: array[(N + 1)3 · M]
3: D_mult_ww_conv_f_ksi, D_mult_ww_conv_f_eta, D_mult_ww_conv_f_zeta: array[(N + 1)3 · M]
4: procedure UPDATE_VOLUME_TERMS(u_next_upd)
5:   for all (p0, p1, p2, p3) ∈ [0, N]4 do
6:     idx ← (p0 · (N + 1)3 + p1 · (N + 1)2 + p2 · (N + 1) + p3) · M
7:     SET_RESCALED_FLUX_TERMS_3D(f_ksi[idx], f_eta[idx], f_zeta[idx], q[idx], dt_div_dr)
8:     SET_RESCALED_SOURCE_TERMS(s[idx], q[idx], s_args[idx], dt)
9:   end for
10:  VOLUME::SET_NON_CONSERVATIVE_TERMS_SUM(b, q, dt_div_dr)
11:  s ← s - b
12:  for all (k1, k2, k3) ∈ [0, N]3 do
13:    idx ← (k1 · (N + 1)2 + k2 · (N + 1) + k3) · M
14:    VOLUME::W_CONV_KERNEL(w_conv_f_ksi[idx], w, f_ksi[idx])
15:    VOLUME::W_CONV_KERNEL(w_conv_f_eta[idx], w, f_eta[idx])
16:    VOLUME::W_CONV_KERNEL(w_conv_f_zeta[idx], w, f_zeta[idx])
17:    VOLUME::W_CONV_KERNEL(w_conv_s[idx], w, s[idx])
18:  end for
19:  for all (k2, k3) ∈ [0, N]2 do
20:    idx ← (k2 · (N + 1) + k3) · M
21:    VOLUME::D_TILDE_F_KSI_KERNEL(D_mult_ww_conv_f_ksi[idx], D_tilde, w_conv_f_ksi[idx])
22:  end for
23:  for all (k1, k3) ∈ [0, N]2 do
24:    idx ← (k1 · (N + 1)2 + k3) · M
25:    VOLUME::D_TILDE_F_ETA_KERNEL(D_mult_ww_conv_f_eta[idx], D_tilde, w_conv_f_eta[idx])
26:  end for
27:  for all (k1, k2) ∈ [0, N]2 do
28:    idx ← (k1 · (N + 1)2 + k2 · (N + 1)) · M
29:    VOLUME::D_TILDE_F_ZETA_KERNEL(D_mult_ww_conv_f_zeta[idx], D_tilde, w_conv_f_zeta[idx])
30:  end for
31:  for all (k1, k2, k3) ∈ [0, N]3 do
32:    idx ← (k1 · (N + 1)2 + k2 · (N + 1) + k3) · M
33:    D_mult_ww_conv_f_ksi[idx] ← D_mult_ww_conv_f_ksi[idx] · w[k2] · w[k3]
34:    D_mult_ww_conv_f_eta[idx] ← D_mult_ww_conv_f_eta[idx] · w[k1] · w[k3]
35:    D_mult_ww_conv_f_zeta[idx] ← D_mult_ww_conv_f_zeta[idx] · w[k1] · w[k2]
36:    w_conv_s[idx] ← w_conv_s[idx] · w[k1] · w[k2] · w[k3]
37:  end for
38:  for all (k1, k2, k3) ∈ [0, N]3 do
39:    idx ← (k1 · (N + 1)2 + k2 · (N + 1) + k3) · M
40:    upd_sum ← D_mult_ww_conv_f_ksi[idx] + D_mult_ww_conv_f_eta[idx]
41:    upd_sum ← upd_sum + D_mult_ww_conv_f_zeta[idx] + w_conv_s[idx]
42:    upd_sum ← upd_sum / (w[k1] · w[k2] · w[k3])
43:    u_next_upd[idx] ← u_next_upd[idx] + upd_sum
44:  end for
45: end procedure

```

Table 3: The main parameters of the BLAS procedures `gemm` used in the one-step discrete finite-volume ADER-WENO scheme.

kernel name	$m$	$n$	$k$	lda	ldb	ldc	$\alpha$	$\beta$
psi_ksi_conv_kernel	1	$M$	$N + 1$	$N + 1$	$(N + 1)^2 M$	$M$	1	0
psi_eta_conv_kernel	1	$M$	$N + 1$	$N + 1$	$(N + 1)M$	$M$	1	0
psi_zeta_conv_kernel	1	$M$	$N + 1$	$N + 1$	$M$	$M$	1	0
w_conv_kernel	1	$M$	$N + 1$	$N + 1$	$M$	$M$	1	0
d_q_ksi_kernel	$N + 1$	$M$	$N + 1$	$N + 1$	$(N + 1)^2 M$	$(N + 1)^2 M$	1	0
d_q_eta_kernel	$N + 1$	$M$	$N + 1$	$N + 1$	$(N + 1)M$	$(N + 1)M$	1	0
d_q_zeta_kernel	$N + 1$	$M$	$N + 1$	$N + 1$	$M$	$M$	1	0
b_ksi_kernel	$M$	$M$	$M$	$M$	$M$	$M$	1	0
b_eta_kernel	$M$	$M$	$M$	$M$	$M$	$M$	1	1
b_zeta_kernel	$M$	$M$	$M$	$M$	$M$	$M$	1	1

**Algorithm 6** Procedure to Algorithm 4 responsible for calculating the contributions from the interface flux terms in the expression (34) and updating them to the preliminary solution  $\mathbf{u}_{\text{next\_upd}}$  at a next time step  $t^{n+1}$ . *Note:* before calling this procedure, it is necessary to call Algorithm 7 responsible for calculating interface flux terms for all mesh interfaces.

```

1: procedure UPDATE_INTERFACE_TERMS( $\mathbf{u}_{\text{next\_upd}}$ )
2:   for all  $(k_1, k_2, k_3) \in [0, N]^3$  do
3:      $\text{idx\_u} \leftarrow (k_1 \cdot (N + 1)^2 + k_2 \cdot (N + 1) + k_3) \cdot M$ 
4:      $\text{idx\_f\_ksi} \leftarrow (k_2 \cdot (N + 1) + k_3) \cdot M$ 
5:      $\text{idx\_f\_eta} \leftarrow (k_1 \cdot (N + 1) + k_3) \cdot M$ 
6:      $\text{idx\_f\_zeta} \leftarrow (k_1 \cdot (N + 1) + k_2) \cdot M$ 
7:      $\text{flux\_term\_ksi} \leftarrow \text{psi\_1}[k_1] \cdot \text{f\_rp\_ksi\_R}[\text{idx\_f\_ksi}] - \text{psi\_0}[k_1] \cdot \text{f\_rp\_ksi\_L}[\text{idx\_f\_ksi}]$ 
8:      $\text{flux\_term\_eta} \leftarrow \text{psi\_1}[k_2] \cdot \text{f\_rp\_eta\_R}[\text{idx\_f\_eta}] - \text{psi\_0}[k_2] \cdot \text{f\_rp\_eta\_L}[\text{idx\_f\_eta}]$ 
9:      $\text{flux\_term\_zeta} \leftarrow \text{psi\_1}[k_3] \cdot \text{f\_rp\_zeta\_R}[\text{idx\_f\_zeta}] - \text{psi\_0}[k_3] \cdot \text{f\_rp\_zeta\_L}[\text{idx\_f\_zeta}]$ 
10:     $\text{upd\_sum} \leftarrow -(\text{flux\_term\_ksi} + \text{flux\_term\_eta} + \text{flux\_term\_zeta}) / (\mathbf{w}[k_1] \cdot \mathbf{w}[k_2] \cdot \mathbf{w}[k_3])$ 
11:     $\mathbf{u}_{\text{next\_upd}}[\text{idx\_u}] \leftarrow \mathbf{u}_{\text{next\_upd}}[\text{idx\_u}] + \text{upd\_sum}$ 
12:   end for
13: end procedure

```

following expression:

$$\begin{aligned}
\mathbf{v}^{n+1} = & \mathbf{v}^n - \sum_{l_0=0}^N \sum_{l_2=0}^N \sum_{l_3=0}^N w_{l_0} w_{l_2} w_{l_3} \left[ \mathfrak{G}_\xi \left( \sum_{p_1=0}^N \tilde{\psi}_{p_1} \hat{\mathbf{q}}_{l_0 p_1 l_2 l_3}, \sum_{p_1=0}^N \psi_{p_1} \hat{\mathbf{q}}_{l_0 p_1 l_2 l_3}^{(R, \xi)} \right) - \mathfrak{G}_\xi \left( \sum_{p_1=0}^N \tilde{\psi}_{p_1} \hat{\mathbf{q}}_{l_0 p_1 l_2 l_3}^{(L, \xi)}, \sum_{p_1=0}^N \psi_{p_1} \hat{\mathbf{q}}_{l_0 p_1 l_2 l_3} \right) \right] \\
& - \sum_{l_0=0}^N \sum_{l_1=0}^N \sum_{l_3=0}^N w_{l_0} w_{l_1} w_{l_3} \left[ \mathfrak{G}_\eta \left( \sum_{p_2=0}^N \tilde{\psi}_{p_2} \hat{\mathbf{q}}_{l_0 l_1 p_2 l_3}, \sum_{p_2=0}^N \psi_{p_2} \hat{\mathbf{q}}_{l_0 l_1 p_2 l_3}^{(R, \eta)} \right) - \mathfrak{G}_\eta \left( \sum_{p_2=0}^N \tilde{\psi}_{p_2} \hat{\mathbf{q}}_{l_0 l_1 p_2 l_3}^{(L, \eta)}, \sum_{p_2=0}^N \psi_{p_2} \hat{\mathbf{q}}_{l_0 l_1 p_2 l_3} \right) \right] \\
& - \sum_{l_0=0}^N \sum_{l_1=0}^N \sum_{l_2=0}^N w_{l_0} w_{l_1} w_{l_2} \left[ \mathfrak{G}_\zeta \left( \sum_{p_3=0}^N \tilde{\psi}_{p_3} \hat{\mathbf{q}}_{l_0 l_1 l_2 p_3}, \sum_{p_3=0}^N \psi_{p_3} \hat{\mathbf{q}}_{l_0 l_1 l_2 p_3}^{(R, \zeta)} \right) - \mathfrak{G}_\zeta \left( \sum_{p_3=0}^N \tilde{\psi}_{p_3} \hat{\mathbf{q}}_{l_0 l_1 l_2 p_3}^{(L, \zeta)}, \sum_{p_3=0}^N \psi_{p_3} \hat{\mathbf{q}}_{l_0 l_1 l_2 p_3} \right) \right] \\
& - \sum_{l_0=0}^N \sum_{l_1=0}^N \sum_{l_2=0}^N \sum_{l_3=0}^N w_{l_0} w_{l_1} w_{l_2} w_{l_3} \left[ \mathfrak{B}_\xi(\hat{\mathbf{q}}_{l_0 l_1 l_2 l_3}) \sum_{r_1=0}^N \mathbb{D}_{r_1 l_1}^\varphi \hat{\mathbf{q}}_{l_0 r_1 l_2 l_3} + \mathfrak{B}_\eta(\hat{\mathbf{q}}_{l_0 l_1 l_2 l_3}) \sum_{r_2=0}^N \mathbb{D}_{r_2 l_2}^\varphi \hat{\mathbf{q}}_{l_0 l_1 r_2 l_3} \right. \\
& \quad \left. + \mathfrak{B}_\zeta(\hat{\mathbf{q}}_{l_0 l_1 l_2 l_3}) \sum_{r_3=0}^N \mathbb{D}_{r_2 l_2}^\varphi \hat{\mathbf{q}}_{l_0 l_1 l_2 r_3} - \mathbf{s}(\hat{\mathbf{q}}_{l_0 l_1 l_2 l_3}, \mathbf{r}(\boldsymbol{\xi}_{l_1 l_2 l_3}), t(\tau_{l_0})) \right], \tag{37}
\end{aligned}$$

where  $\psi_k = \varphi_k(0)$ ,  $\tilde{\psi}_k = \varphi_k(1)$ , and upper indices  $(L, \xi)$ ,  $(L, \eta)$ ,  $(L, \zeta)$  and  $(R, \xi)$ ,  $(R, \eta)$ ,  $(R, \zeta)$  denote the discrete space-time solution  $\mathbf{q}$  in the left and right cells with respect to the selected cell in directions  $\xi$ ,  $\eta$  and  $\zeta$ , respectively.

## 4.2 Using the BLAS interface

The resulting expression (37) for the one-step discrete finite-volume ADER-WENO scheme contained basic linear algebra operations, which were implemented using the BLAS interface. The general paradigm for data storage and using the matrix-matrix multiplication operation was chosen in a form similar to the implementation of the LST-DG predictor and the finite-element ADER-DG scheme, which is presented in Subsections 2.2 and 3.2. Only the `gemm` procedure of the 3rd level of the BLAS interface was used. In this case, only the row major data storage format was used. Table 3 presents the main parameters of all `gemm` procedures used. Algorithm 8 presents the general form of the algorithm for calculating the solution  $\mathbf{v}_{\text{next}}$  at the next time step  $t^{n+1}$ , while the calculation of the solution is separate into two main procedures, one of which presented in Algorithm 9, the second procedure `update_interface_terms` updates the solution with differences in interface flux terms, which is a trivial operation and is essentially similar to Algorithm 6 for the ADER-DG method. Also the additional procedures in Algorithm 7 for computing the interface flux terms `f_rp_ksi_interface`, `f_rp_eta_interface`, `f_rp_zeta_interface` is separated. The calculation of interface flux terms is carried out in three separate procedures `set_interfaces_terms_ksi`, `set_interfaces_terms_eta` and `set_interfaces_terms_zeta`, which is associated with the use of Cartesian meshes. Matrices `psi_1`, `psi_2` and `w` contain values  $\psi_k$ ,  $\tilde{\psi}_k$  and  $w_k$ . The procedures calculating the solution to the Riemann problem `rs_rescaled_flux_ksi`, `rs_rescaled_flux_eta` and `rs_rescaled_flux_zeta`, calculated fluxes immediately in the rescaled variables, for which the values `dt_div_dx`, `dt_div_dy` and `dt_div_dz` are passed as formal parameters to procedures. Procedure `volume::set_non_conservative_terms_sum`, responsible for calculating non-conservative terms, is structured similarly to the procedure presented in Algorithms 3 for the LST-DG predictor and 5 for finite-element ADER-DG scheme. In general, the presented implementation allows the solution  $\mathbf{u}^{n+1}$  to be computed at the next time step  $t^{n+1}$  using BLAS interface procedures, without the use of transpose  $\mathbf{q}_{r,p} \mapsto \mathbf{q}_{p,r}$  [16]. The parameters of the procedure are known in advance, so the proposed approach is well suited to the use of JIT functions available in modern implementations of the BLAS interface for calculations with small matrices.

---

**Algorithm 7** The procedure associated with Algorithm 4 responsible for computing the interface flux terms in the expression (34).

---

```

1: psi_conv_qL, psi_conv_qR, f_rp_ksi, f_rp_eta, f_rp_zeta: array[(N + 1)3 · M]
2: f_rp_ksi_interface, f_rp_eta_interface, f_rp_zeta_interface: array[(N + 1)2 · M]
3: procedure SET_INTERFACES_TERMS_KSI
4:   for all (k0, k1, k3) ∈ [0, N]3 do
5:     idx_f ← (k0 · (N + 1)2 + k2 · (N + 1) + k3) · M
6:     idx_q ← (k0 · (N + 1)3 + k2 · (N + 1) + k3) · M
7:     INTERFACE::PSI_KSI_CONV_KERNEL(psi_conv_qL[0], psi_1, qL_ksi[idx_q])
8:     INTERFACE::PSI_KSI_CONV_KERNEL(psi_conv_qR[0], psi_0, qR_ksi[idx_q])
9:     RS_RESCALED_FLUX_KSI(f_rp_ksi[idx_f], psi_conv_qL, psi_conv_qR[0], dt_div_dx)
10:   end for
11:   for all (k2, k3) ∈ [0, N]2 do
12:     idx ← (k1 · (N + 1) + k3) · M
13:     INTERFACE::W_CONV_KERNEL(f_rp_ksi_interface[idx], w, f_rp_ksi[idx])
14:     f_rp_ksi_interface[idx] ← f_rp_ksi_interface[idx] · w[k2] · w[k3]
15:   end for
16: end procedure
17: procedure SET_INTERFACES_TERMS_ETA
18:   for all (k0, k1, k3) ∈ [0, N]3 do
19:     idx_f ← (k0 · (N + 1)2 + k1 · (N + 1) + k3) · M
20:     idx_q ← (k0 · (N + 1)3 + k1 · (N + 1)2 + k3) · M
21:     INTERFACE::PSI_ETA_CONV_KERNEL(psi_conv_qL[0], psi_1, qL_eta[idx_q])
22:     INTERFACE::PSI_ETA_CONV_KERNEL(psi_conv_qR[0], psi_0, qR_eta[idx_q])
23:     RS_RESCALED_FLUX_ETA(f_rp_eta[idx_f], psi_conv_qL, psi_conv_qR[0], dt_div_dy)
24:   end for
25:   for all (k1, k3) ∈ [0, N]2 do
26:     idx ← (k1 · (N + 1) + k3) · M
27:     INTERFACE::W_CONV_KERNEL(f_rp_eta_interface[idx], w, f_rp_eta[idx])
28:     f_rp_eta_interface[idx] ← f_rp_eta_interface[idx] · w[k1] · w[k3]
29:   end for
30: end procedure
31: procedure SET_INTERFACES_TERMS_ZETA
32:   for all (k0, k1, k2) ∈ [0, N]3 do
33:     idx_f ← (k0 · (N + 1)2 + k1 · (N + 1) + k2) · M
34:     idx_q ← (k0 · (N + 1)3 + k1 · (N + 1)2 + k2 · (N + 1)) · M
35:     INTERFACE::PSI_ZETA_CONV_KERNEL(psi_conv_qL[0], psi_1, qL_zeta[idx_q])
36:     INTERFACE::PSI_ZETA_CONV_KERNEL(psi_conv_qR[0], psi_0, qR_zeta[idx_q])
37:     RS_RESCALED_FLUX_ZETA(f_rp_zeta[idx_f], psi_conv_qL, psi_conv_qR[0], dt_div_dz)
38:   end for
39:   for all (k1, k2) ∈ [0, N]2 do
40:     idx ← (k2 · (N + 1) + k3) · M
41:     INTERFACE::W_CONV_KERNEL(f_rp_zeta_interface[idx], w, f_rp_zeta[idx])
42:     f_rp_zeta_interface[idx] ← f_rp_zeta_interface[idx] · w[k1] · w[k2]
43:   end for
44: end procedure

```

---

**Algorithm 8** The basic general structure of using BLAS interface procedure calls in the implementation of the one-step discrete finite-volume ADER-WENO scheme.

---

```

1: function GET_FV_SOLUTION(v_prev)
2:   v_next ← v_prev
3:   UPDATE_VOLUME_TERMS(v_next)
4:   UPDATE_INTERFACE_TERMS(v_next)
5:   return v_next
6: end function

```

---

## 5 Representations transformations in subcell correction by finite-volume method

### 5.1 General description

The finite-element ADER-DG methods are the high order linear methods, therefore, the fundamental property of monotonicity of the numerical solution obtained using them may be violated, which is explained by the well-known Godunov theorem. Therefore, ADER-DG methods are used in conjunction with high stable finite-volume limiters, which avoid violation of monotonicity and the occurrence of non-physical artifacts of the numerical solution [6, 10, 11, 16]. The finite-volume limiters can use both the

---

**Algorithm 9** Procedure to Algorithm 8 responsible for calculating the contributions from the volume terms in the expression (37) and updating them to the preliminary solution  $\mathbf{v}_{\text{next\_upd}}$  at a next time step  $t^{n+1}$ .

---

```

1:  $\mathbf{f\_ksi}, \mathbf{f\_eta}, \mathbf{f\_zeta}, \mathbf{s}, \mathbf{b}$ : array $[(N + 1)^4 \cdot M]$ 
2:  $\mathbf{w\_conv\_f\_ksi}, \mathbf{w\_conv\_f\_eta}, \mathbf{w\_conv\_f\_zeta}$ : array $[(N + 1)^3 \cdot M]$ 
3:  $\mathbf{D\_mult\_ww\_conv\_f\_ksi}, \mathbf{D\_mult\_ww\_conv\_f\_eta}, \mathbf{D\_mult\_ww\_conv\_f\_zeta}$ : array $[(N + 1)^3 \cdot M]$ 
4: procedure UPDATE_VOLUME_TERMS( $\mathbf{v}_{\text{next\_upd}}$ )
5:   for all  $(p_0, p_1, p_2, p_3) \in [0, N]^4$  do
6:      $\text{idx} \leftarrow (p_0 \cdot (N + 1)^3 + p_1 \cdot (N + 1)^2 + p_2 \cdot (N + 1) + p_3) \cdot M$ 
7:     SET_RESCALED_SOURCE_TERMS( $\mathbf{s}[\text{idx}], \mathbf{q}[\text{idx}], \mathbf{s\_args}[\text{idx}], \text{dt}$ )
8:   end for
9:   VOLUME::SET_NON_CONSERVATIVE_TERMS_SUM( $\mathbf{b}, \mathbf{q}, \text{dt.div.dr}$ )
10:   $\mathbf{s} \leftarrow \mathbf{s} - \mathbf{b}$ 
11:  for all  $(p_0, p_1, p_2) \in [0, N]^3$  do
12:     $\text{idx\_s} \leftarrow (p_0 \cdot (N + 1)^3 + p_1 \cdot (N + 1)^2 + p_2 \cdot (N + 1)) \cdot M$ 
13:     $\text{idx\_d} \leftarrow (p_0 \cdot (N + 1)^2 + p_1 \cdot (N + 1) + p_2) \cdot M$ 
14:    W_CONV_KERNEL( $\mathbf{w\_p3\_conv\_s}[\text{idx\_d}], \mathbf{w}, \mathbf{s}[\text{idx\_s}]$ )
15:  end for
16:  for all  $(p_0, p_1) \in [0, N]^2$  do
17:     $\text{idx\_s} \leftarrow (p_0 \cdot (N + 1)^2 + p_1 \cdot (N + 1)) \cdot M$ 
18:     $\text{idx\_d} \leftarrow (p_0 \cdot (N + 1) + p_1) \cdot M$ 
19:    W_CONV_KERNEL( $\mathbf{w\_p2p3\_conv\_s}[\text{idx\_d}], \mathbf{w}, \mathbf{w\_p3\_conv\_s}[\text{idx\_s}]$ )
20:  end for
21:  for all  $p_0 \in [0, N]$  do
22:     $\text{idx\_s} \leftarrow (p_0 \cdot (N + 1) + p_1) \cdot M$ 
23:     $\text{idx\_d} \leftarrow p_0 \cdot M$ 
24:    W_CONV_KERNEL( $\mathbf{w\_p1p2p3\_conv\_s}[\text{idx\_d}], \mathbf{w}, \mathbf{w\_p2p3\_conv\_s}[\text{idx\_s}]$ )
25:  end for
26:  W_CONV_KERNEL( $\mathbf{w\_p0p1p2p3\_conv\_s}[0], \mathbf{w}, \mathbf{w\_p1p2p3\_conv\_s}[0]$ )
27:   $\mathbf{v}_{\text{next\_upd}} \leftarrow \mathbf{v}_{\text{next\_upd}} + \mathbf{w\_p0p1p2p3\_conv\_s}$ 
28: end procedure

```

---

classical Godunov and TVD methods [11], as well as the high-precision finite-volume ADER-WENO method [6, 10]. To maintain high accuracy and subgrid resolution of the numerical solution obtained by ADER-DG methods, it is customary to use the method of subcell correction of the solution [6, 10], when a finite-volume limiter, which does not have subgrid resolution, is called in the subgrid created in the cell. A sub-grid is created within the cell  $\Omega_i$  containing  $N_s$  subcells with the spatial step  $h/N_s$  in each coordinate direction – a total of  $N_s^3$  sub-cells in the 3D case. In subcells  $\Omega_{i,j}$ , an alternative data representation  $\mathbf{v}_j$  is determined by finite-volume average values (8) for each subcell  $\Omega_{i,j}$  from the original high-precision DG representation  $\mathbf{u}(\boldsymbol{\xi})$  of the solution. It should be noted that the subgrid finite-volume alternative data representation is used not only for the purpose of subcell correction of the solution: calculating the time step  $\Delta t^n$  requires calculating the maximum values of the signal speed  $\lambda$  in the solution in the entire spatial mesh, which is usually difficult to do mathematically strictly due to the high computational cost of calculating the extrema of multidimensional polynomials degrees in each cell – instead of strict extrema, maximum values can be calculated using a finite-volume subcell representation  $\mathbf{v}_j$ ; a similar approach is used to test the numerical admissibility detector [10].

Using a subgrid solution correction requires the use of two subgrid operators – the suitable piecewise-constant projection operator  $\hat{\mathbb{P}}$  and the suitable high order accurate reconstruction operator  $\hat{\mathbb{R}}$ . The suitable piecewise-constant projection operator  $\hat{\mathbb{P}}$  calculates finite-volume average values  $\mathbf{v}$  for each subcells  $\Omega$  using the known high-precision DG representation  $\mathbf{u}(\boldsymbol{\xi})$  of the solution:

$$\mathbf{v} = \hat{\mathbb{P}} \cdot \mathbf{u}, \quad (38)$$

and the suitable high order accurate reconstruction operator  $\hat{\mathbb{R}}$  calculates the inverse transformation, calculating a high-precision DG representation of the solution using the known subgrid finite-volume representation:

$$\mathbf{u} = \hat{\mathbb{R}} \cdot \mathbf{v}. \quad (39)$$

The operators  $\hat{\mathbb{P}}$  and  $\hat{\mathbb{R}}$  have one-side reversibility:  $\hat{\mathbb{R}} \circ \hat{\mathbb{P}} = 1$ . In case  $N_s = N$ , the amount of information about the solution in the finite-volume subcell representation  $\mathbf{v}$  and in the high-precision DG representation  $\mathbf{u}$  is the same, and the operators have the property of complete reversibility –  $\hat{\mathbb{P}} \circ \hat{\mathbb{R}} = 1$ . However, usually the value  $N_s = 2N + 1$ , which is due to the requirement that the time step  $\Delta t^n$  coincide for finite-volume numerical methods and DG methods [6], therefore reversibility in a different order of action of the operators does not occur –  $\hat{\mathbb{P}} \circ \hat{\mathbb{R}} \neq 1$ , in the chosen case  $N_s = 2N + 1 > N + 1$  for  $N \geq 1$ .

The derivation of the formula expression for operator 1 is based on the following considerations. A high-precision DG representation of the solution  $\mathbf{u} = \mathbf{u}(\boldsymbol{\xi})$  (7) is averaged over each subcell  $\Omega_{i,j}$  of the subgrid in cell  $\Omega_i$ , resulting in the following expression (8):

$$\mathbf{v}_j = N_s^3 \int_{\Omega_{i,j}} d\boldsymbol{\xi} \cdot \mathbf{u}(\boldsymbol{\xi}) = N_s^3 \int_{\frac{j_1}{N_s}}^{\frac{j_1+1}{N_s}} d\xi \int_{\frac{j_2}{N_s}}^{\frac{j_2+1}{N_s}} d\eta \int_{\frac{j_3}{N_s}}^{\frac{j_3+1}{N_s}} d\zeta \cdot \sum_k \mathbf{u}_k \Phi_k(\xi, \eta, \zeta) = \sum_k \mathbb{P}_{j,k} \mathbf{u}_k, \quad (40)$$

**Algorithm 10** The procedure associated with Algorithm 8 responsible for computing the interface flux terms in the expression (37).

---

```

1: psi_conv_qL, psi_conv_qR, f_rp_ksi, f_rp_eta, f_rp_zeta: array[(N + 1)3 · M]
2: wk3_conv_f_rp_ksi, wk3_conv_f_rp_eta, wk3_conv_f_rp_zeta: array[(N + 1)2 · M]
3: wk2k3_conv_f_rp_ksi, wk2k3_conv_f_rp_eta, wk2k3_conv_f_rp_zeta: array[(N + 1) · M]
4: f_rp_ksi_interface, f_rp_eta_interface, f_rp_zeta_interface: array[M]
5: procedure SET_INTERFACES_TERMS_KSI
6:   for all (k0, k2, k3) ∈ [0, N]3 do
7:     idx_f ← (k0 · (N + 1)2 + k2 · (N + 1) + k3) · M
8:     idx_q ← (k0 · (N + 1)3 + k2 · (N + 1) + k3) · M
9:     INTERFACE::PSL_KSI_CONV_KERNEL(psi_conv_qL[0], psi_1, qL_ksi[idx_q])
10:    INTERFACE::PSL_KSI_CONV_KERNEL(psi_conv_qR[0], psi_0, qR_ksi[idx_q])
11:    RS_RESCALED_FLUX_KSI(f_rp_ksi[idx_f], psi_conv_qL, psi_conv_qR[0], dt_div_dx)
12:  end for
13:  for all (k0, k2) ∈ [0, N]2 do
14:    idx_s ← (k0 · (N + 1)2 + k2) · M
15:    idx_d ← (k0 · (N + 1) + k2) · M
16:    W_CONV_KERNEL(w_k3_conv_f_rp_ksi[idx_d], w, f_rp_ksi[idx_s])
17:  end for
18:  for all k0 ∈ [0, N]2 do
19:    idx_s ← k0 · (N + 1)M
20:    idx_d ← k0 · M
21:    W_CONV_KERNEL(w_k2k3_conv_f_rp_ksi[idx_d], w, wk3_conv_f_rp_ksi[idx_s])
22:  end for
23:  W_CONV_KERNEL(f_rp_ksi_interface[0], w, wk2k3_conv_f_rp_ksi[0])
24: end procedure
25: procedure SET_INTERFACES_TERMS_ETA
26:   for all (k0, k1, k3) ∈ [0, N]3 do
27:     idx_f ← (k0 · (N + 1)2 + k1 · (N + 1) + k3) · M
28:     idx_q ← (k0 · (N + 1)3 + k1 · (N + 1)2 + k3) · M
29:     INTERFACE::PSI_ETA_CONV_KERNEL(psi_conv_qL[0], psi_1, qL_eta[idx_q])
30:     INTERFACE::PSI_ETA_CONV_KERNEL(psi_conv_qR[0], psi_0, qR_eta[idx_q])
31:     RS_RESCALED_FLUX_ETA(f_rp_eta[idx_f], psi_conv_qL, psi_conv_qR[0], dt_div_dy)
32:   end for
33:   for all (k0, k1) ∈ [0, N]2 do
34:     idx_s ← (k0 · (N + 1)2 + k1 · (N + 1)) · M
35:     idx_d ← (k0 · (N + 1) + k1) · M
36:     W_CONV_KERNEL(w_k3_conv_f_rp_eta[idx_d], w, f_rp_eta[idx_s])
37:   end for
38:   for all k0 ∈ [0, N]2 do
39:     idx_s ← k0 · (N + 1)M
40:     idx_d ← k0 · M
41:     W_CONV_KERNEL(w_k2k3_conv_f_rp_eta[idx_d], w, wk3_conv_f_rp_eta[idx_s])
42:   end for
43:   W_CONV_KERNEL(f_rp_eta_interface[0], w, wk2k3_conv_f_rp_eta[0])
44: end procedure

```

---

Table 4: The main parameters of the BLAS procedures `gemm` used in the suitable piecewise-constant projection operator  $\hat{\mathbb{P}}$  and the suitable high order accurate reconstruction operator  $\hat{\mathbb{R}}$ .

kernel name	$m$	$n$	$k$	lda	ldb	ldc	$\alpha$	$\beta$
<code>p_inner_stage_kernel</code>	$N_s$	$M$	$N + 1$	$N + 1$	$M$	$(N + 1)^2 M$	1	0
<code>p_mider_stage_kernel</code>	$N_s$	$M$	$N + 1$	$N + 1$	$M$	$(N + 1)N_s M$	1	0
<code>p_outer_stage_kernel</code>	$N_s$	$M$	$N + 1$	$N + 1$	$M$	$N_s^2 M$	1	0
<code>r_inner_stage_kernel</code>	$N + 1$	$M$	$N_s$	$N_s$	$M$	$N_s^2 M$	1	0
<code>r_mider_stage_kernel</code>	$N + 1$	$M$	$N_s$	$N_s$	$M$	$(N + 1)N_s M$	1	0
<code>r_outer_stage_kernel</code>	$N + 1$	$M$	$N_s$	$N_s$	$M$	$(N + 1)^2 M$	1	0

where  $k = (k_1, k_2, k_3)$ ,  $j = (j_1, j_2, j_3)$  is the three-component multi-indices:  $0 \leq k_1, k_2, k_3 \leq N$ ,  $0 \leq j_1, j_2, j_3 < N_s$ ; it should be noted that these multi-indices define different index ranges and can be unambiguously converted into through indices (19):

$$\begin{aligned}
k &= k_1 \cdot (N + 1)^2 + k_2 \cdot (N + 1) + k_3; \\
j &= j_1 \cdot N_s^2 + j_2 \cdot N_s + j_3;
\end{aligned} \tag{41}$$

which take ranges of  $0 \leq k < (N + 1)^3$  and  $0 \leq j < N_s^3$ . In an application-interesting [6, 10, 11, 16] case  $N_s = 2N + 1 > N + 1$ ,

---

**Algorithm 11** Continuation of Algorithm 10.

---

```

45: procedure SET_INTERFACES_TERMS_ZETA
46:   for all  $(k_0, k_1, k_2) \in [0, N]^3$  do
47:      $\text{idx}_f \leftarrow (k_0 \cdot (N+1)^2 + k_1 \cdot (N+1) + k_2) \cdot M$ 
48:      $\text{idx}_q \leftarrow (k_0 \cdot (N+1)^3 + k_1 \cdot (N+1)^2 + k_2 \cdot (N+1)) \cdot M$ 
49:     INTERFACE::PSI_ZETA_CONV_KERNEL( $\text{psi\_conv\_q\_L}[0]$ ,  $\text{psi}_1$ ,  $\text{q\_L\_zeta}[\text{idx}_q]$ )
50:     INTERFACE::PSI_ZETA_CONV_KERNEL( $\text{psi\_conv\_q\_R}[0]$ ,  $\text{psi}_0$ ,  $\text{q\_R\_zeta}[\text{idx}_q]$ )
51:     RS_RESCALED_FLUX_ZETA( $\text{f\_rp\_zeta}[\text{idx}_f]$ ,  $\text{psi\_conv\_q\_L}$ ,  $\text{psi\_conv\_q\_R}[0]$ ,  $\text{dt\_div\_dz}$ )
52:   end for
53:   for all  $(k_0, k_1) \in [0, N]^2$  do
54:      $\text{idx}_s \leftarrow (k_0 \cdot (N+1)^2 + k_1 \cdot (N+1)) \cdot M$ 
55:      $\text{idx}_d \leftarrow (k_0 \cdot (N+1) + k_1) \cdot M$ 
56:     W_CONV_KERNEL( $\text{w\_k3\_conv\_f\_rp\_zeta}[\text{idx}_d]$ ,  $\text{w}$ ,  $\text{f\_rp\_zeta}[\text{idx}_s]$ )
57:   end for
58:   for all  $k_0 \in [0, N]^2$  do
59:      $\text{idx}_s \leftarrow k_0 \cdot (N+1)M$ 
60:      $\text{idx}_d \leftarrow k_0 \cdot M$ 
61:     W_CONV_KERNEL( $\text{w\_k2k3\_conv\_f\_rp\_zeta}[\text{idx}_d]$ ,  $\text{w}$ ,  $\text{w\_k3\_conv\_f\_rp\_zeta}[\text{idx}_s]$ )
62:   end for
63:   W_CONV_KERNEL( $\text{f\_rp\_zeta\_interface}[0]$ ,  $\text{w}$ ,  $\text{w\_k2k3\_conv\_f\_rp\_zeta}[0]$ )
64: end procedure

```

---

**Algorithm 12** The basic general structure of using BLAS interface procedure calls in the suitable piecewise-constant projection operator  $\hat{\mathbb{P}}$ .

---

```

1:  $\mathbf{u}$ : array $[(N+1)^3 \cdot M]$ 
2:  $\text{temp\_matrix\_inner}$ : array $[(N+1)^2 \cdot N_s \cdot M]$ 
3:  $\text{temp\_matrix\_mider}$ : array $[(N+1) \cdot N_s^2 \cdot M]$ 
4:  $\mathbf{v}$ : array $[N_s^3 \cdot M]$ 
5: function P_OPERATOR( $\mathbf{u}$ )
6:   for all  $(p_1, p_2) \in [0, N] \times [0, N]$  do
7:      $\text{idx}_d \leftarrow (p_1 \cdot (N+1) + p_2) \cdot M$ 
8:      $\text{idx}_s \leftarrow (p_1 \cdot (N+1)^2 + p_2 \cdot (N+1)) \cdot M$ 
9:     P_INNER_STAGE_KERNEL( $\text{temp\_matrix\_inner}[\text{idx}_d]$ ,  $\text{p\_matrix}$ ,  $\mathbf{u}[\text{idx}_s]$ )
10:  end for
11:  for all  $(k_3, p_1) \in [0, N_s - 1] \times [0, N]$  do
12:     $\text{idx}_d \leftarrow (k_3 \cdot (N+1) + p_1) \cdot M$ 
13:     $\text{idx}_s \leftarrow (k_3 \cdot (N+1)^2 + p_1 \cdot (N+1)) \cdot M$ 
14:    P_MIDER_STAGE_KERNEL( $\text{temp\_matrix\_mider}[\text{idx}_d]$ ,  $\text{p\_matrix}$ ,  $\text{temp\_matrix\_inner}[\text{idx}_s]$ )
15:  end for
16:  for all  $(k_2, p_3) \in [0, N_s - 1] \times [0, N_s - 1]$  do
17:     $\text{idx}_d \leftarrow (k_2 \cdot N_s + k_3) \cdot M$ 
18:     $\text{idx}_s \leftarrow (k_2 \cdot (N+1)N_s + k_3 \cdot (N+1)) \cdot M$ 
19:    P_OUTER_STAGE_KERNEL( $\mathbf{v}[\text{idx}_d]$ ,  $\text{p\_matrix}$ ,  $\text{temp\_matrix\_mider}[\text{idx}_s]$ )
20:  end for
21:  return  $\mathbf{v}$ 
22: end function

```

---

the inverse transformation is defined by suitable high order accurate reconstruction operator  $\hat{\mathbb{R}}$  using a pseudo-inverse matrix:

$$\mathbf{u}_k = \sum_j \mathbb{R}_{k,j} \mathbf{v}_j = \sum_j \left\{ \left[ \mathbb{P}^T \mathbb{P} \right]^{-1} \cdot \mathbb{P} \right\}_{k,j} \mathbf{v}_j, \quad (42)$$

where expression  $[\mathbb{P}^T \mathbb{P}]^{-1} \mathbb{P}$  defines the pseudo-inverse matrix. The presented expressions for the suitable piecewise-constant projection operator  $\hat{\mathbb{P}}$  and the suitable high order accurate reconstruction operator  $\hat{\mathbb{R}}$  allowed to conclude that the matrices of these operators can be represented in the form of Kronecker products:

$$\begin{aligned} \mathbb{P} &= \mathbf{P} \otimes \mathbf{P} \otimes \mathbf{P}; \\ \mathbb{R} &= \mathbf{R} \otimes \mathbf{R} \otimes \mathbf{R}; \end{aligned} \quad (43)$$

which can be pre-computed in code, and where  $\mathbf{P}$  is a  $N_s \times (N+1)$  matrix containing elements of the following form:

$$\mathbf{P}_{j,k} = N_s \int_{\frac{j}{N_s}}^{\frac{j+1}{N_s}} d\xi \cdot \varphi_k(\xi), \quad (44)$$

where indices take ranges of  $0 \leq j < N_s$  and  $0 \leq k \leq N$ , and  $\mathbf{R}$  is the pseudo-inverse of matrix  $\mathbf{P}$ .

---

**Algorithm 13** The basic general structure of using BLAS interface procedure calls in the suitable high order accurate reconstruction operator  $\hat{\mathbb{R}}$ .

---

```

1: v: array[ $N_s^3 \cdot M$ ]
2: temp_matrix_inner: array[ $N_s^2 \cdot (N + 1) \cdot M$ ]
3: temp_matrix_mider: array[ $N_s \cdot (N + 1)^2 \cdot M$ ]
4: u: array[ $(N + 1)^3 \cdot M$ ]
5: function R_OPERATOR(v)
6:   for all  $(k_1, k_2) \in [0, N_s - 1] \times [0, N_s - 1]$  do
7:     idx.d  $\leftarrow (k_1 \cdot N_s + k_2) \cdot M$ 
8:     idx.s  $\leftarrow (k_1 \cdot N_s^2 + k_2 \cdot N_s) \cdot M$ 
9:     P_INNER_STAGE_KERNEL(temp_matrix_inner[idx.d], p_matrix, v[idx.s])
10:   end for
11:   for all  $(p_3, k_1) \in [0, N] \times [0, N_s - 1]$  do
12:     idx.d  $\leftarrow (p_3 \cdot N_s + k_1) \cdot M$ 
13:     idx.s  $\leftarrow (p_3 \cdot N_s^2 + k_1 \cdot N_s) \cdot M$ 
14:     P_MIDER_STAGE_KERNEL(temp_matrix_mider[idx.d], p_matrix, temp_matrix_inner[idx.s])
15:   end for
16:   for all  $(p_2, p_3) \in [0, N] \times [0, N]$  do
17:     idx.d  $\leftarrow (p_2 \cdot (N + 1) + p_3) \cdot M$ 
18:     idx.s  $\leftarrow (p_2 \cdot N_s^2 + p_3 \cdot N_s) \cdot M$ 
19:     P_OUTER_STAGE_KERNEL(u[idx.d], p_matrix, temp_matrix_mider[idx.s])
20:   end for
21:   return u
22: end function

```

---

## 5.2 Using the BLAS interface

The resulting expressions for the suitable piecewise-constant projection operator  $\hat{\mathbb{P}}$  (38) and the suitable high order accurate reconstruction operator  $\hat{\mathbb{R}}$  (39) were implemented using the `gemm` function of the BLAS interface. In this case, only the row major data storage format was used, and `notrans` was selected for the operations `transa` and `transb`. The parameters of the `gemm` function that were used in the implementation are presented in Table 4. The algorithmic description of the implementation of the suitable piecewise-constant projection operator  $\hat{\mathbb{P}}$  is presented in Algorithm 12; the algorithmic description of the implementation of the suitable high order accurate reconstruction operator  $\hat{\mathbb{R}}$  is presented in Algorithm 13. The parameters of the procedure are known in advance, so the proposed approach is well suited to the use of JIT functions available in modern implementations of the BLAS interface for calculations with small matrices.

## 6 Applications of the numerical method

Applications of the implementations of the numerical methods of the ADER family presented in this work have been implemented using the example of classical gas dynamics problems described by a system of non-stationary Euler equations, which is a quasilinear system of hyperbolic equations for describing compressible flows, which takes the following form:

$$\frac{\partial}{\partial t} \begin{bmatrix} \rho \\ \rho \mathbf{v} \\ \varepsilon \end{bmatrix} + \nabla \cdot \begin{bmatrix} \rho \mathbf{v} \\ \rho \mathbf{v} \otimes \mathbf{v} + p \mathbf{I} \\ (\varepsilon + p) \mathbf{v} \end{bmatrix} = \mathbf{S}, \quad (45)$$

where  $\rho$  is the mass density;  $\mathbf{v} = (u, v, w)$  is the velocity;  $p$  is the pressure;  $\varepsilon$  is the total energy density including the thermal  $e$  and the kinetic contributions  $\varepsilon = e + \frac{1}{2} \rho v^2$ ;  $\mathbf{v} \otimes \mathbf{v} \equiv \mathbf{v} \mathbf{v}^T$  is the tensor products. The source term  $\mathbf{S} = \mathbf{S}(\mathbf{U}; \mathbf{r}, t)$  allows arbitrary dependence on conserved variables  $\mathbf{U}$ , spatial coordinates  $\mathbf{r} = (x, y, z)$  and time  $t$ .

The numerical finite-element method ADER-DG with a posteriori correction of the solution by the finite-volume ADER-WENO limiter in subcells was chosen, which made it possible to demonstrate the capabilities of the implementations of the finite-element ADER-DG and finite-volume ADER-WENO methods presented in this work. The adaptive finite-element ADER-DG method is characterized by a very high accuracy and resolution of the smooth components of the solution. Non-physical anomalies of the numerical solution arising due to the fundamental linearity of the ADER-DG method, which are explained by the well-known Godunov theorem, were corrected by an a posteriori limiter, for which the high-precision finite-volume ADER-WENO method was chosen. Each time step of the space-time adaptive ADER-DG finite-element method with LST-DG predictor and a posteriori sub-cell ADER-WENO finite-volume limiting involved a sequence of steps [6–11, 13, 14, 26, 28–30]:

- a LST-DG predictor, using which a local discrete space-time solution in the small was obtained;
- a pure ADER-DG scheme, using which a candidate high accuracy solution was obtained;
- a determination of physical and numerical admissibility of the obtained high accuracy candidate solution and identification of “troubled” cells;
- a recalculation of the solution in “troubled” cells by a stable ADER-WENO finite-volume limiter.



An excellent detailed description of this computational scheme is given in the basic works [6–11, 13, 14, 26, 28–30] of the developers of this method. Details of the internal structure of the ADER-DG are presented in the works [6, 7, 28, 29]. Details of the internal structure of the finite-element ADER-DG and finite-volume ADER-WENO methods, in which the LST-DG prediction method is used, are presented in the works [8, 9]. Peculiarities of mathematical formulation and efficient software implementation are discussed in [16, 17] and [19, 31–34]. The modern state of development of the space-time adaptive ADER finite-element DG method with a posteriori correction technique of solutions on sub-cells by the finite-volume limiter using AMR for use on unstructured meshes and using the ALE approach is presented in the works [36, 37].

The one-step discrete ADER-DG scheme is explicit, despite the presence of a locally implicit LST-DG predictor. The Courant-Friedrichs-Lewy stability criterion is imposed on the time step  $\Delta t^n$  [43, 44]:

$$\Delta t^n = \text{CFL} \cdot \frac{1}{d} \cdot \frac{1}{2N+1} \cdot \min_{k=1, \dots, d} \left[ \frac{h_k}{|\lambda_k^{max}|} \right], \quad (46)$$

where  $\text{CFL} \leq 1$  is the Courant number,  $d$  is the spatial dimension of the problem,  $N$  is the degrees of polynomials used in the DG representation (7),  $h_k$  is the spatial mesh step in the  $k$ -direction,  $|\lambda_k^{max}|$  is the maximum signal speed in the  $k$ -direction for which the expression  $|\lambda_k^{max}| = |u_k| + c$  was used, where  $u_k$  is the flow velocity in the  $k$ -direction,  $c$  is the sound speed.

Two main admissibility criteria were used: the physical admissibility detector (PAD) and the numerical admissibility detector (NAD), which are widely used [6–11, 13, 14, 26, 28–30] in numerical methods for solving quasi-linear equations with a posteriori correction of the numerical solution. The physical admissibility detector checks the candidate numerical solution for the admissibility of the main physical assumptions of the problem; in this work, these were the condition of positivity of the density  $\rho$  and internal energy density  $e$ . The positiveness of the pressure  $p$  automatically follow from the fulfillment of these admissibility conditions. In this work the numerical admissibility detector was chosen in a cell representation. It is based on the use of the relaxed discrete maximum principle (DMP) in the polynomial sense, and is expressed by the following inequality [7, 10, 11]:

$$\min_{\mathbf{r}' \in V_i} (\mathbf{u}(\mathbf{r}', t^n)) - \delta \leq \mathbf{u}^*(\mathbf{r}, t^{n+1}) \leq \max_{\mathbf{r}' \in V_i} (\mathbf{u}(\mathbf{r}', t^n)) + \delta, \quad \forall \mathbf{r} \in \Omega_i, \quad (47)$$

where the maximum and minimum are taken over the set  $V_i$  that contains this cell  $\Omega_i$  and its Voronov neighboring cells. An additional small vector quantity  $\delta$ , which is given by the expression

$$\delta = \max \left[ \delta_0, \epsilon_0 \cdot \left( \max_{\mathbf{r}' \in V_i} (\mathbf{u}(\mathbf{r}', t^n)) - \min_{\mathbf{r}' \in V_i} (\mathbf{u}(\mathbf{r}', t^n)) \right) \right], \quad (48)$$

determines the tolerance of the criterion – the real calculation in software implementation is carried out not on the polynomial representation  $\mathbf{u}$  (7) of the solution, but on the basis of a finite-volume sub-cell representation  $\mathbf{v}_j$  (38), which is formed in a subgrid of the cell; the use of exact extrema of the solution representation would require significant computational costs, especially in the case of high degrees of  $N$  and two- and three-dimensional problems, so an approach was chosen with the analysis of the finite-volume representation  $\mathbf{v}_j$  and a small expansion of the criterion admissibility window by  $\delta$ . The values  $\delta_0 = 10^{-4}$  and  $\epsilon = 10^{-3}$  were chosen in accordance with the recommendations of the works [7, 10]. The inequality (47) was stated in vector form – feasibility was checked for each individual component of the vector of conservative variables, and the final conclusion of feasibility was determined by the  $\wedge$  logical operation for all components of the vector. Subcell forms of the numerical admissibility detector (the so-called SubNAD), used in particular in methods with flux reconstruction [41, 42], were not used in this work. In general, the choice of criteria for the admissibility of a candidate numerical solution corresponds to the approaches proposed in the works [7, 10, 11].

The algorithmic and software implementation of the numerical finite-element method ADER-DG with a posteriori correction of the solution by the finite-volume ADER-WENO limiter in subcells was chosen in the form presented in this work, with effective use of the BLAS interface for performing matrix-matrix operations of linear algebra.

## 6.1 Accuracy and convergence

**PDE system problem** The accuracy and convergence of the space-time adaptive ADER-DG numerical method with a posteriori sub-cell ADER-WENO finite-volume limiting were tested based on a numerical solution of the two-dimensional problem of the advection of a sine wave in a periodic spatial domain [41]. The accuracy and convergence for two-dimensional and three-dimensional problems were studied. The use of a sine wave advection problem is standard in the field of research of numerical methods.

The initial conditions were chosen in the form of a stationary ambient gas flow with the parameters: density  $\rho_\infty = 1$ , velocity  $(u_\infty, v_\infty, w_\infty)$ , pressure  $p_\infty = 1$ . In the two-dimensional case, the velocity was chosen as  $(u_\infty, v_\infty, w_\infty) = (1, 1, 0)$ , in the three-dimensional case, the velocity was chosen as  $(u_\infty, v_\infty, w_\infty) = (1, 1, 1)$ . The local density perturbation  $\delta\rho$  was imposed on the flow, expressed in the form of a sine wave, which in the two-dimensional case was given in form  $\delta\rho = 0.5 \cdot \sin(2\pi(x+y))$ , in the three-dimensional case – in form  $\delta\rho = 0.5 \cdot \sin(2\pi(x+y+z))$ . The adiabatic index  $\gamma = 1.4$ .

The coordinate domain was chosen in the form of a unit square  $\Omega = [0, 1] \times [0, 1]$  in the two-dimensional case and a unit cube  $\Omega = [0, 1] \times [0, 1] \times [0, 1]$  in the three-dimensional case. Periodic boundary conditions were chosen. The exact analytical solution of the problem represents the process of simple advection of a sine wave, which can be expressed by a function  $\rho = \rho_0(\mathbf{r} - \mathbf{v}_\infty t)$  for the density, constant pressure  $p = p_\infty$  and constant flow velocity  $(u, v, w) = (u_\infty, v_\infty, w_\infty)$ . With the selected initial conditions, coordinate domain and periodic boundary conditions, the sine wave returns to its original coordinate position, and the exact solution returns to the initial conditions, after a period of time  $\Delta t = 1$ . Therefore the final time  $t_{\text{final}} = 1.0$  was chosen. The exact solutions are shown in Figure 2 (left) in the two-dimensional case and Figure 1 (left) in the three-dimensional case.

Figure 1 and Figure 2 shows numerical solution to this problem in the two-dimensional and the three-dimensional cases obtained using the ADER-DG- $\mathbb{P}_9$  method on  $2 \times 2$  and  $2 \times 2 \times 2$  meshes, respectively. The presented results demonstrate that the numerical solution differs slightly from the exact solution visually, while in the three-dimensional case these differences are

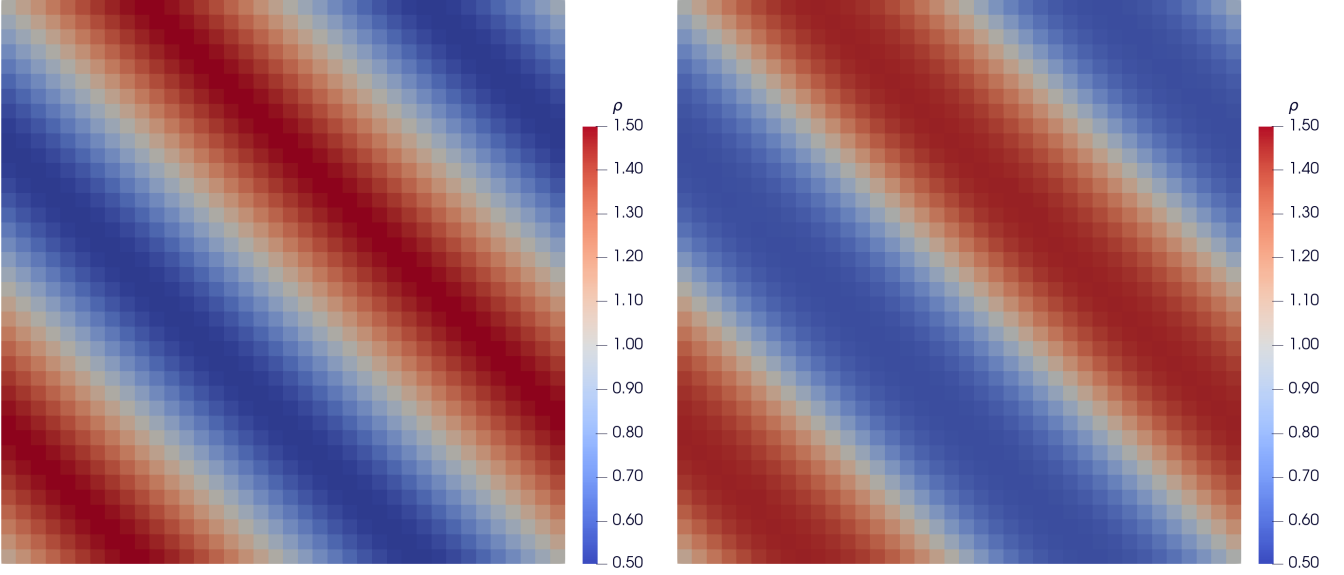


Figure 1: Numerical solution of the two-dimensional problem of a sine wave advection (a detailed statement of the problem is presented in the text) obtained using the ADER-DG- $\mathbb{P}_9$  method on a  $2 \times 2$  mesh at the final time  $t_{\text{final}} = 1.0$ : subcells finite-volume representation of exact (left) and numerical (right) solutions for density  $\rho$ .

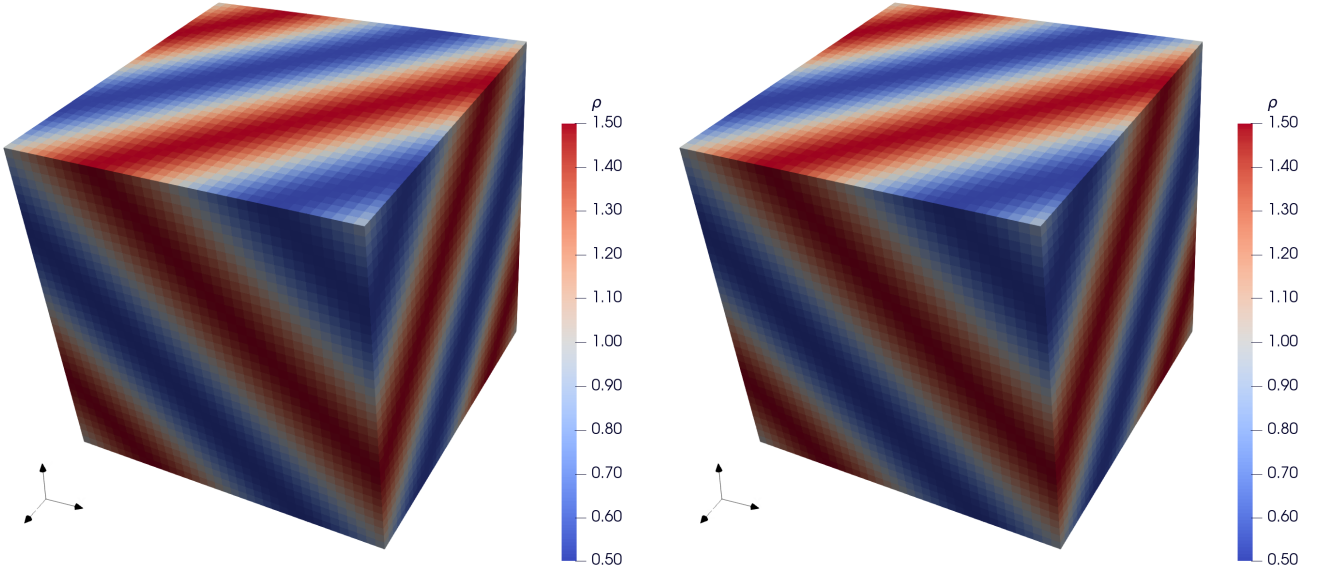


Figure 2: Numerical solution of the three-dimensional problem of a sine wave advection (a detailed statement of the problem is presented in the text) obtained using the ADER-DG- $\mathbb{P}_9$  method on a  $2 \times 2$  mesh at the final time  $t_{\text{final}} = 1.0$ : subcells finite-volume representation of exact (left) and numerical (right) solutions for density  $\rho$ .

practically not visible. However, when the  $2 \times 2$  size of the spatial mesh is taken into account, this result demonstrates the unusually high accuracy of the ADER-DG- $\mathbb{P}_N$  method.

The error  $\epsilon$  of the numerical solution was calculated in three functional norms  $L_1$ ,  $L_2$ ,  $L_\infty$  for the density  $\rho$ :

$$\begin{aligned}
 \epsilon_{L_1} &= \int_{\Omega} |\rho(\mathbf{r}, t_{\text{final}}) - \rho_{\text{exact}}(\mathbf{r})| dV; \\
 \epsilon_{L_2}^2 &= \int_{\Omega} [\rho(\mathbf{r}, t_{\text{final}}) - \rho_{\text{exact}}(\mathbf{r})]^2 dV; \\
 \epsilon_{L_\infty} &= \text{ess sup}_{\mathbf{r} \in \Omega} |\rho(\mathbf{r}, t_{\text{final}}) - \rho_{\text{exact}}(\mathbf{r})|;
 \end{aligned} \tag{49}$$

where the integrals were calculated as the sum of the integrals for each finite-element cell  $\Omega_k$  over the function of the DG representation of the solution  $\mathbf{u}$ , and the calculation was carried out using the Gauss-Legendre quadrature formula based on polynomials of degree 25 for each coordinate direction; the calculation of the supremum to determine the norm of error  $\epsilon_{L_\infty}$  was performed using a finite-volume subcell representation of the solution. The errors  $\epsilon$  were obtained for a set of

Table 5:  $L_1$ ,  $L_2$  and  $L_\infty$  norms of errors  $\epsilon$ , by density  $\rho$ , and convergence orders  $p$  for ADER-DG- $\mathbb{P}_N$  method with a posteriori ADER-WENO2 finite-volume limiter, for two-dimensional sine wave advection problem;  $p_{\text{theor.}} = N+1$  is the theoretical accuracy order of the ADER-DG- $\mathbb{P}_N$  method.

	cells	$\epsilon_{L_1}$	$\epsilon_{L_2}$	$\epsilon_{L_\infty}$	$p_{L_1}$	$p_{L_2}$	$p_{L_\infty}$	theor.
DG- $\mathbb{P}_1$	$10^2$	5.48E-03	7.33E-03	3.29E-02	–	–	–	2
	$15^2$	2.44E-03	3.26E-03	1.46E-02	1.99	1.99	2.00	
	$20^2$	1.37E-03	1.84E-03	8.16E-03	2.01	2.00	2.02	
	$25^2$	8.78E-04	1.18E-03	5.25E-03	2.00	2.00	1.98	
DG- $\mathbb{P}_2$	$10^2$	2.87E-04	3.89E-04	1.98E-03	–	–	–	3
	$15^2$	8.44E-05	1.16E-04	6.04E-04	3.02	2.99	2.93	
	$20^2$	3.55E-05	4.88E-05	2.54E-04	3.01	3.00	3.02	
	$25^2$	1.81E-05	2.50E-05	1.31E-04	3.00	3.00	2.97	
DG- $\mathbb{P}_3$	$10^2$	1.13E-05	1.54E-05	9.07E-05	–	–	–	4
	$15^2$	2.22E-06	3.05E-06	1.79E-05	4.00	4.00	3.99	
	$20^2$	7.02E-07	9.66E-07	5.65E-06	4.01	4.00	4.02	
	$25^2$	2.87E-07	3.96E-07	2.33E-06	4.00	4.00	3.97	
DG- $\mathbb{P}_4$	$10^2$	3.58E-07	4.87E-07	3.04E-06	–	–	–	5
	$15^2$	4.67E-08	6.42E-08	4.15E-07	5.02	5.00	4.91	
	$20^2$	1.10E-08	1.52E-08	9.77E-08	5.01	5.00	5.03	
	$25^2$	3.61E-09	5.00E-09	3.23E-08	5.00	5.00	4.96	
DG- $\mathbb{P}_5$	$5^2$	6.09E-07	8.12E-07	5.50E-06	–	–	–	6
	$10^2$	9.33E-09	1.28E-08	8.89E-08	6.03	5.99	5.95	
	$15^2$	8.18E-10	1.12E-09	7.80E-09	6.00	6.00	6.00	
	$20^2$	1.45E-10	2.00E-10	1.38E-09	6.01	6.00	6.02	
DG- $\mathbb{P}_6$	$5^2$	2.75E-08	3.66E-08	2.69E-07	–	–	–	7
	$10^2$	2.12E-10	2.88E-10	2.05E-09	7.02	6.99	7.04	
	$15^2$	1.23E-11	1.69E-11	1.25E-10	7.03	7.00	6.90	
	$20^2$	1.63E-12	2.25E-12	1.65E-11	7.01	7.00	7.03	
DG- $\mathbb{P}_7$	$5^2$	1.08E-09	1.44E-09	1.08E-08	–	–	–	8
	$10^2$	4.13E-12	5.66E-12	4.39E-11	8.03	7.99	7.95	
	$15^2$	1.61E-13	2.21E-13	1.71E-12	8.01	8.00	8.00	
	$20^2$	1.60E-14	2.22E-14	1.71E-13	8.01	8.00	8.00	
DG- $\mathbb{P}_8$	$2^2$	1.49E-07	1.84E-07	7.36E-07	–	–	–	9
	$4^2$	2.77E-10	3.74E-10	2.29E-09	9.08	8.94	8.33	
	$6^2$	7.37E-12	9.79E-12	7.03E-11	8.94	8.98	8.59	
	$8^2$	5.39E-13	7.37E-13	5.58E-12	9.09	8.99	8.81	
DG- $\mathbb{P}_9$	$2^2$	1.09E-08	1.45E-08	1.19E-07	–	–	–	10
	$4^2$	1.09E-11	1.47E-11	9.27E-11	9.97	9.95	10.33	
	$6^2$	1.88E-13	2.57E-13	2.14E-12	10.00	9.98	9.30	
	$8^2$	1.06E-14	1.45E-14	1.15E-13	10.01	9.99	10.17	

mesh coordinate steps  $h$ , from which the empirical values of the convergence orders  $p$  were calculated:  $\epsilon \sim h^p$ , therefore  $p = \ln(\epsilon(h_1)/\epsilon(h_2))/\ln(h_1/h_2)$ .

The calculated empirical convergence orders  $p_1, p_2, p_\infty$  for errors  $\epsilon_{L_1}, \epsilon_{L_2}, \epsilon_{L_\infty}$  for ADER-DG- $\mathbb{P}_N$  method with a posteriori limitation of the solution by a ADER-WENO2 finite-volume limiter are presented in Table 5 for two-dimensional problem and in Table 6 for three-dimensional problem. The results are obtained for degrees  $N = 1, \dots, 9$ . It should be noted that the solution to this test problem is smooth, and the limiter was not called in all cases the solution was obtained from the use of a limiter – the admissibility criteria were not activated. The expected theoretical values of the convergence orders  $p_{\text{theor.}} = N + 1$  [6] are presented in Tables 5 and 6 for comparison. The presented results show that in all cases of orders of polynomials  $N \leq 9$  in the DG-representation, there is a good correspondence between the empirical  $p$  and theoretical  $p_{\text{theor.}}$  convergence orders. It should be noted, in order to obtain correct values of empirical orders of convergence in the case of large degrees  $N = 8, 9$ , a special choice of the mesh coordinate step  $h$  is necessary – in the region of small  $h$  there is a significant increase in round-off errors, which leads to an increase in error  $\epsilon$ .

The ADER-DG- $\mathbb{P}_N$  numerical method demonstrates very high accuracy of the numerical solution even on very coarse meshes, which is especially well observed for polynomial degrees  $N = 7-9$ . In the case of ADER-DG- $\mathbb{P}_7$  method, the round-off error of double-precision floating-point numbers is practically achieved on  $15^2$ - $20^2$  meshes, both for two-dimensional and three-dimensional problems, and in the case of ADER-DG- $\mathbb{P}_9$  method, such a low error of the numerical solution is achieved already on  $6^2$ - $8^2$  meshes.

The presented results on the convergence orders for ADER-DG- $\mathbb{P}_N$  method with a posteriori limitation of the solution by finite-volume limiter are in good agreement with the results of the basic works [6, 10]. This allows us to conclude that the software implementation of the ADER-DG- $\mathbb{P}_N$  method is correct.

**ODE system problem** It should be noted separately that the numerical method applied to initial value problems (IVP) for ordinary differential equation systems (ODE systems) demonstrates superconvergence with convergence orders  $2N + 1$ , which is

Table 6:  $L_1$ ,  $L_2$  and  $L_\infty$  norms of errors  $\epsilon$ , by density  $\rho$ , and convergence orders  $p$  for ADER-DG- $\mathbb{P}_N$  method with a posteriori ADER-WENO2 finite-volume limiter, for three-dimensional sine wave advection problem;  $p_{\text{theor.}} = N + 1$  is the theoretical accuracy order of the ADER-DG- $\mathbb{P}_N$  method.

	cells	$\epsilon_{L_1}$	$\epsilon_{L_2}$	$\epsilon_{L_\infty}$	$p_{L_1}$	$p_{L_2}$	$p_{L_\infty}$	theor.
DG- $\mathbb{P}_1$	$10^3$	5.24E-02	5.83E-02	1.75E-01	–	–	–	2
	$15^3$	1.08E-02	1.30E-02	5.23E-02	3.89	3.71	2.98	
	$20^3$	4.62E-03	5.70E-03	2.99E-02	2.95	2.86	1.94	
	$25^3$	2.82E-03	3.53E-03	2.18E-02	2.21	2.15	1.42	
DG- $\mathbb{P}_2$	$10^3$	7.69E-04	9.29E-04	6.07E-03	–	–	–	3
	$15^3$	2.22E-04	2.72E-04	1.92E-03	3.06	3.03	2.85	
	$20^3$	9.29E-05	1.15E-04	8.20E-04	3.03	3.01	2.95	
	$25^3$	4.74E-05	5.86E-05	4.20E-04	3.02	3.00	3.00	
DG- $\mathbb{P}_3$	$10^3$	2.17E-05	2.78E-05	2.46E-04	–	–	–	4
	$15^3$	4.28E-06	5.48E-06	4.89E-05	4.00	4.01	3.99	
	$20^3$	1.35E-06	1.73E-06	1.56E-05	4.01	4.01	3.97	
	$25^3$	5.54E-07	7.08E-07	6.42E-06	4.00	4.00	3.97	
DG- $\mathbb{P}_4$	$10^3$	7.69E-07	9.96E-07	8.96E-06	–	–	–	5
	$15^3$	1.03E-07	1.34E-07	1.26E-06	4.95	4.95	4.84	
	$20^3$	2.48E-08	3.21E-08	2.99E-07	4.97	4.97	4.99	
	$25^3$	8.16E-09	1.06E-08	9.68E-08	4.97	4.98	5.05	
DG- $\mathbb{P}_5$	$5^3$	1.11E-06	1.45E-06	1.36E-05	–	–	–	6
	$10^3$	1.67E-08	2.19E-08	2.26E-07	6.05	6.05	5.90	
	$15^3$	1.46E-09	1.92E-09	1.97E-08	6.01	6.01	6.02	
	$20^3$	2.60E-10	3.41E-10	3.52E-09	6.00	6.00	5.99	
DG- $\mathbb{P}_6$	$5^3$	5.24E-08	6.83E-08	6.55E-07	–	–	–	7
	$10^3$	4.36E-10	5.74E-10	5.37E-09	6.91	6.90	6.93	
	$15^3$	2.59E-11	3.42E-11	3.39E-10	6.96	6.96	6.82	
	$20^3$	3.49E-12	4.59E-12	4.55E-11	6.98	6.98	6.98	
DG- $\mathbb{P}_7$	$5^3$	1.90E-09	2.52E-09	2.43E-08	–	–	–	8
	$10^3$	7.14E-12	9.50E-12	1.01E-10	8.05	8.05	7.90	
	$15^3$	2.78E-13	3.70E-13	3.97E-12	8.00	8.01	7.99	
	$20^3$	2.74E-14	3.72E-14	4.45E-13	8.06	7.99	7.61	
DG- $\mathbb{P}_8$	$2^3$	2.27E-07	2.94E-07	2.17E-06	–	–	–	9
	$4^3$	5.08E-10	6.67E-10	5.01E-09	8.81	8.78	8.76	
	$6^3$	1.39E-11	1.84E-11	1.58E-10	8.88	8.86	8.52	
	$8^3$	1.07E-12	1.42E-12	1.28E-11	8.91	8.90	8.73	
DG- $\mathbb{P}_9$	$2^3$	2.20E-08	2.87E-08	2.56E-07	–	–	–	10
	$4^3$	1.98E-11	2.63E-11	1.89E-10	10.12	10.09	10.40	
	$6^3$	3.30E-13	4.40E-13	4.36E-12	10.10	10.08	9.30	
	$8^3$	1.91E-14	2.53E-14	2.73E-13	9.91	9.93	9.62	

obtained when considering the solution at time nodes  $\mathbf{u}^n$  (7). This type of superconvergence for DG methods for solving ODE systems is well known [45, 46] and has been studied in many works [47–52]. In work [22], the superconvergence with convergence orders  $2N + 1$  was shown specifically for the ADER-DG method as applied to ODE systems. However, the convergence of the local discrete space-time solution  $\mathbf{q}$  (6) (in the case of ODE systems, this is already a local discrete *time* solution, because the sought function depends only on one argument with respect to the ODE system problem) demonstrates only the convergence order  $N + 1$ , which is typical for the ADER-DG method when solving PDE systems.

In this work, the convergence of the ADER-DG- $\mathbb{P}_N$  method was also investigated in solving “ODE systems”, which are PDE systems from the point of view of the formula statement of the problem, and ODE systems taking into account the coordinate dependence of the initial conditions and the selected boundary conditions. In the selected problem, the initial conditions are completely free of dependence on space variables, making the coordinate derivatives of the flux terms zero, and the boundary conditions are chosen to be consistent with the selected initial conditions. As a result of this choice of initial and boundary conditions for the PDE system, the dynamic evolution of the solution is determined only by the source term  $\mathbf{S}$ , which was also chosen to be independent of the coordinates.

The original system of Euler equations (45), extended by the system of two convection-reaction equations, taking into account the chosen reaction mechanism in a two-component medium, takes the following form:

$$\frac{\partial}{\partial t} \begin{bmatrix} \rho \\ \rho \mathbf{v} \\ \varepsilon \\ \rho c_1 \\ \rho c_2 \end{bmatrix} + \nabla \cdot \begin{bmatrix} \rho \mathbf{v} \\ \rho \mathbf{v} \otimes \mathbf{v} + p \mathbf{I} \\ (\varepsilon + p) \mathbf{v} \\ \rho c_1 \mathbf{v} \\ \rho c_2 \mathbf{v} \end{bmatrix} = \begin{bmatrix} 0 \\ \mathbf{0} \\ 0 \\ +\rho c_2 \\ -\omega^2 \rho c_1 \end{bmatrix}, \quad (50)$$

where  $c_1$  is the mass concentration of the reaction reagent  $A$ ,  $c_2$  is the mass concentration of the reaction reagent  $B$ ,  $[\rho c_2, -\omega^2 \rho c_1]^T$  is the “reaction rates” (in real reacting flows, it is clear that such a reaction mechanism does not exist – the equations allow

Table 7: Global  $L_1$ ,  $L_2$  and  $L_\infty$  norms of errors  $\epsilon$  and global convergence orders  $p$  for ADER-DG- $\mathbb{P}_N$  method for IVP ODE system problem;  $p_{\text{theor.}} = 2N + 1$  is the theoretical global accuracy order of the ADER-DG- $\mathbb{P}_N$  method for IVP ODE system problem.

	time steps	$\epsilon_{L_1}$	$\epsilon_{L_2}$	$\epsilon_{L_\infty}$	$p_{L_1}$	$p_{L_2}$	$p_{L_\infty}$	theor.
DG- $\mathbb{P}_1$	10	1.56E+00	5.15E-01	2.53E-01	–	–	–	3
	20	2.35E-01	7.81E-02	4.06E-02	2.73	2.72	2.64	
	30	7.16E-02	2.37E-02	1.25E-02	2.93	2.94	2.90	
	40	3.05E-02	1.01E-02	5.34E-03	2.97	2.98	2.96	
	50	1.56E-02	5.15E-03	2.75E-03	2.99	2.99	2.98	
DG- $\mathbb{P}_2$	10	2.86E-02	9.60E-03	4.95E-03	–	–	–	5
	20	9.56E-04	3.18E-04	1.67E-04	4.90	4.92	4.89	
	30	1.27E-04	4.19E-05	2.23E-05	4.98	5.00	4.97	
	40	3.03E-05	9.98E-06	5.31E-06	4.98	4.99	4.98	
	50	9.91E-06	3.26E-06	1.74E-06	5.01	5.01	4.99	
DG- $\mathbb{P}_3$	10	2.35E-04	7.92E-05	4.13E-05	–	–	–	7
	20	1.94E-06	6.44E-07	3.39E-07	6.92	6.94	6.93	
	30	1.14E-07	3.75E-08	2.00E-08	7.00	7.01	6.98	
	40	1.53E-08	5.03E-09	2.68E-09	6.97	6.99	6.99	
	50	3.19E-09	1.05E-09	5.63E-10	7.01	7.01	6.99	
DG- $\mathbb{P}_4$	10	1.16E-06	3.93E-07	2.05E-07	–	–	–	9
	20	2.37E-09	7.87E-10	4.14E-10	8.94	8.96	8.95	
	30	6.16E-11	2.04E-11	1.09E-11	9.00	9.01	8.98	
	40	4.65E-12	1.53E-12	8.17E-13	8.98	8.99	8.99	
	50	6.23E-13	2.05E-13	1.10E-13	9.01	9.02	9.00	
DG- $\mathbb{P}_5$	3	1.51E-03	5.35E-04	2.53E-04	–	–	–	11
	4	8.19E-05	2.83E-05	1.30E-05	10.13	10.22	10.31	
	5	7.09E-06	2.45E-06	1.23E-06	10.97	10.97	10.59	
	6	1.01E-06	3.49E-07	1.73E-07	10.67	10.68	10.73	
	7	1.93E-07	6.68E-08	3.27E-08	10.78	10.74	10.81	
DG- $\mathbb{P}_6$	3	4.14E-05	1.48E-05	7.09E-06	–	–	–	13
	4	1.25E-06	4.31E-07	1.98E-07	12.17	12.29	12.43	
	5	6.73E-08	2.33E-08	1.18E-08	13.08	13.07	12.66	
	6	6.69E-09	2.30E-09	1.14E-09	12.66	12.69	12.78	
	7	9.24E-10	3.21E-10	1.58E-10	12.84	12.79	12.84	
DG- $\mathbb{P}_7$	3	8.37E-07	3.01E-07	1.46E-07	–	–	–	15
	4	1.41E-08	4.87E-09	2.24E-09	14.20	14.34	14.52	
	5	4.78E-10	1.66E-10	8.41E-11	15.16	15.15	14.71	
	6	3.30E-11	1.14E-11	5.65E-12	14.66	14.70	14.81	
	7	3.33E-12	1.16E-12	5.71E-13	14.89	14.83	14.87	
DG- $\mathbb{P}_8$	1	1.53E-01	6.11E-02	2.44E-02	–	–	–	17
	2	1.00E-05	3.65E-06	1.60E-06	13.90	14.03	13.90	
	3	1.32E-08	4.76E-09	2.31E-09	16.35	16.38	16.13	
	4	1.23E-10	4.25E-11	1.96E-11	16.26	16.40	16.58	
	5	2.65E-12	9.19E-13	4.66E-13	17.19	17.18	16.75	
DG- $\mathbb{P}_9$	1	2.49E-02	9.91E-03	3.96E-03	–	–	–	19
	2	2.95E-07	1.07E-07	4.69E-08	16.36	16.50	16.36	
	3	1.66E-10	5.98E-11	2.89E-11	18.45	18.48	18.23	
	4	8.55E-13	2.95E-13	1.36E-13	18.32	18.46	18.63	

negative concentrations  $c_1$  and  $c_2$  of components),  $\omega$  is the constant.

The initial conditions are presented in the form of spatially uniform stationary gas flow with parameters  $\rho_\infty = 1$ ,  $(u_\infty, v_\infty, w_\infty) = (1, 1, 1)$ ,  $p_\infty = 1$ . The initial concentration values were chosen as follows:  $c_1 = 1$ ,  $c_2 = 0$ . The periodic boundary conditions were chosen. The coordinate domain  $\Omega = [0, 1] \times [0, 1] \times [0, 1]$ . Taking into account such initial and boundary conditions, the problem (50) is reduced to the following IVP for ODE system:

$$\begin{cases} \frac{du_1}{dt} = u_2; & u_1(0) = 1; \\ \frac{du_2}{dt} = -\omega^2 u_1; & u_2(0) = 0; \end{cases} \quad (51)$$

which is a system of equations of a one-dimensional linear harmonic oscillator with frequency  $\omega$ , where  $u_1 \equiv c_1$  and  $u_2 \equiv c_2$ . The exact analytical solution of this problem is as follows:  $u_1^{\text{ex}}(t) = \cos(\omega t)$ ,  $u_2^{\text{ex}}(t) = -\omega \sin(\omega t)$ . In the calculations it was assumed that  $\omega = 1$ . The final time was chosen as  $t_{\text{final}} = 2\pi$ . The spatial mesh was selected as single cell. The values of the time step  $\Delta t^n$  were not determined from the Courant condition, but were explicitly specified by the amount of time steps, chosen uniformly in the range  $[0, t_{\text{final}}]$ .

Table 8: Local  $L_1$ ,  $L_2$  and  $L_\infty$  norms of errors  $\epsilon$  and local convergence orders  $p$  for ADER-DG- $\mathbb{P}_N$  method for IVP ODE system problem;  $p_{\text{theor.}} = N + 1$  is the theoretical local accuracy order of the ADER-DG- $\mathbb{P}_N$  method for IVP ODE system problem.

	time steps	$\epsilon_{L_1}$	$\epsilon_{L_2}$	$\epsilon_{L_\infty}$	$p_{L_1}$	$p_{L_2}$	$p_{L_\infty}$	theor.
DG- $\mathbb{P}_1$	10	1.87E+00	2.49E+00	3.09E-01	–	–	–	2
	20	3.55E-01	4.84E-01	6.04E-02	2.40	2.37	2.36	
	30	1.38E-01	1.90E-01	2.78E-02	2.34	2.31	1.91	
	40	7.21E-02	1.01E-01	1.60E-02	2.24	2.20	1.92	
	50	4.43E-02	6.28E-02	1.03E-02	2.18	2.12	1.95	
DG- $\mathbb{P}_2$	10	1.09E-01	1.54E-01	3.08E-02	–	–	–	3
	20	1.24E-02	1.95E-02	4.07E-03	3.13	2.98	2.92	
	30	3.64E-03	5.84E-03	1.22E-03	3.03	2.98	2.98	
	40	1.53E-03	2.47E-03	5.11E-04	3.02	2.99	3.02	
	50	7.82E-04	1.27E-03	2.64E-04	3.00	2.98	2.96	
DG- $\mathbb{P}_3$	10	7.75E-03	1.23E-02	2.89E-03	–	–	–	4
	20	4.84E-04	7.99E-04	1.84E-04	4.00	3.95	3.97	
	30	9.53E-05	1.59E-04	3.65E-05	4.01	3.98	3.99	
	40	3.00E-05	5.04E-05	1.15E-05	4.02	4.00	4.03	
	50	1.23E-05	2.08E-05	4.74E-06	3.98	3.97	3.96	
DG- $\mathbb{P}_4$	10	4.87E-04	8.16E-04	2.02E-04	–	–	–	5
	20	1.53E-05	2.65E-05	6.43E-06	4.99	4.95	4.97	
	30	2.01E-06	3.51E-06	8.50E-07	5.01	4.98	4.99	
	40	4.75E-07	8.34E-07	2.00E-07	5.02	5.00	5.03	
	50	1.56E-07	2.75E-07	6.62E-08	4.98	4.97	4.95	
DG- $\mathbb{P}_5$	3	3.32E-02	4.85E-02	1.27E-02	–	–	–	6
	4	6.60E-03	1.04E-02	2.53E-03	5.61	5.34	5.63	
	5	1.63E-03	2.65E-03	6.95E-04	6.28	6.14	5.78	
	6	5.51E-04	9.22E-04	2.39E-04	5.94	5.79	5.85	
	7	2.18E-04	3.72E-04	9.63E-05	6.00	5.89	5.90	
DG- $\mathbb{P}_6$	3	5.15E-03	7.81E-03	2.14E-03	–	–	–	7
	4	7.76E-04	1.26E-03	3.13E-04	6.58	6.35	6.69	
	5	1.53E-04	2.54E-04	6.82E-05	7.29	7.17	6.82	
	6	4.32E-05	7.35E-05	1.95E-05	6.92	6.80	6.88	
	7	1.47E-05	2.53E-05	6.70E-06	7.01	6.91	6.92	
DG- $\mathbb{P}_7$	3	6.95E-04	1.10E-03	3.09E-04	–	–	–	8
	4	7.88E-05	1.32E-04	3.33E-05	7.57	7.37	7.74	
	5	1.23E-05	2.12E-05	5.78E-06	8.31	8.20	7.85	
	6	2.91E-06	5.10E-06	1.37E-06	7.92	7.81	7.90	
	7	8.47E-07	1.50E-06	4.03E-07	8.01	7.92	7.93	
DG- $\mathbb{P}_8$	1	8.40E-01	8.43E-01	1.99E-01	–	–	–	9
	2	3.00E-03	4.52E-03	1.24E-03	8.13	7.54	7.32	
	3	8.21E-05	1.35E-04	3.89E-05	8.87	8.66	8.54	
	4	6.95E-06	1.21E-05	3.11E-06	8.58	8.39	8.78	
	5	8.71E-07	1.55E-06	4.31E-07	9.31	9.21	8.87	
DG- $\mathbb{P}_9$	1	2.70E-01	2.98E-01	8.27E-02	–	–	–	10
	2	4.99E-04	7.56E-04	2.14E-04	9.08	8.62	8.60	
	3	9.00E-06	1.48E-05	4.36E-06	9.90	9.70	9.60	
	4	5.74E-07	9.90E-07	2.60E-07	9.57	9.40	9.80	

The convergence orders were calculated separately for the solution at the nodes  $\mathbf{u}^n$ , for which the phenomenon of superconvergence  $p = 2N + 1$  was expected, and for the local discrete solution  $\mathbf{q}$ . The errors for solution at time nodes  $\epsilon$  and for the local discrete solution  $\epsilon$  were calculated based on the following expressions:

$$\begin{aligned}
\epsilon_{L_1} &= \sum_n \Delta t^n \int_{\Omega} |\mathbf{u}^n(\boldsymbol{\xi}(\mathbf{r})) - \mathbf{u}_{\text{exact}}(\mathbf{r}, t^n)| dV; & \epsilon_{L_1} &= \int_0^{t_{\text{final}}} \int_{\Omega} |\mathbf{q}(\boldsymbol{\xi}(\mathbf{r}), \tau(t)) - \mathbf{u}_{\text{exact}}(\mathbf{r}, t)| dt dV; \\
\epsilon_{L_2}^2 &= \sum_n \Delta t^n \int_{\Omega} |\mathbf{u}^n(\boldsymbol{\xi}(\mathbf{r})) - \mathbf{u}_{\text{exact}}(\mathbf{r}, t^n)|^2 dV; & \epsilon_{L_2}^2 &= \int_0^{t_{\text{final}}} \int_{\Omega} |\mathbf{q}(\boldsymbol{\xi}(\mathbf{r}), \tau(t)) - \mathbf{u}_{\text{exact}}(\mathbf{r}, t)|^2 dt dV; \\
\epsilon_{L_\infty} &= \max_n \text{ess sup}_{\mathbf{r} \in \Omega} |\mathbf{u}^n(\boldsymbol{\xi}(\mathbf{r})) - \mathbf{u}_{\text{exact}}(\mathbf{r}, t^n)|; & \epsilon_{L_\infty} &= \text{ess sup}_{\mathbf{r}, t \in \Omega \times [0, t_{\text{final}}]} |\mathbf{q}(\boldsymbol{\xi}(\mathbf{r}), \tau(t)) - \mathbf{u}_{\text{exact}}(\mathbf{r}, t)|;
\end{aligned} \tag{52}$$

where the integrals were calculated as an integral by single finite-element cell  $\Omega_k$  and as a sum for each time range  $[t^n, t^{n+1}] \subseteq$

$[0, t_{\text{final}}]$  over the function of the DG representation of the solution  $\mathbf{u}$ , and the calculation was carried out using the Gauss-Legendre quadrature formula based on polynomials of degree 25 for each coordinate direction and by time; the calculation of the supremum to determine the norm of error  $\epsilon_{L_\infty}$  was performed using a finite-volume subcell representation of the solution for coordinate directions and obtaining the maximum value of 1000 equally spaced nodes in each time range  $[t^n, t^{n+1}]$ . The operation  $|\dots|$  denotes taking the maximum absolute value of the components of a vector. The errors  $\epsilon$  were obtained for a set of time steps amount with time step  $\Delta t$ , from which the empirical values of the convergence orders  $p$  were calculated:  $\epsilon \sim \Delta t^p$ , therefore  $p = \ln(\epsilon(\Delta t_1)/\epsilon(\Delta t_2))/\ln(\Delta t_1/\Delta t_2)$ .

The calculated empirical convergence orders  $p_1, p_2, p_\infty$  by errors  $\epsilon_{L_1}, \epsilon_{L_2}, \epsilon_{L_\infty}$  for solution at time nodes and by  $\epsilon_{L_1}, \epsilon_{L_2}, \epsilon_{L_\infty}$  for local solution are presented in Tables 7 and 8 for ADER-DG- $\mathbb{P}_N$  method. The results were obtained for degrees  $N = 1, \dots, 9$ . The expected theoretical values of the convergence orders  $p_{\text{theor.}} = N + 1$  for solution at time nodes  $\mathbf{u}^n$  and  $p_{\text{theor.}} = 2N + 1$  for the local solution  $\mathbf{q}$  are presented in Tables 7 and 8 for comparison. The presented results show that in all cases of orders of polynomials  $N \leq 9$  in the DG-representation, there is a good correspondence between the empirical  $p$  and theoretical  $p_{\text{theor.}}$  convergence orders. The numerical method demonstrates well the expected superconvergence with convergence order  $2N + 1$  for the solution at time nodes  $\mathbf{u}^n$ . It should be noted that in order to obtain correct values of empirical orders of convergence in the case of large degrees  $N = 8, 9$ , a special choice of the time step is necessary – in the region of small  $\Delta t$  there is a significant increase in round-off errors, which leads to an increase in errors  $\epsilon$  and  $\varepsilon$ . For the local solution  $\mathbf{q}$ , the errors did not reach the scale of round-off errors for double-precision floating-point numbers, however, this was achieved for the solution at time nodes  $\mathbf{u}^n$ , which of course affected the local solution, for which the node solution acts as the initial condition at each time step.

The presented results on the convergence orders for ADER-DG- $\mathbb{P}_N$  method are in good agreement with the results [22]. The numerical method demonstrates well the expected superconvergence with convergence order  $2N + 1$  for the solution at time nodes  $\mathbf{u}^n$ . This allows us to conclude that the software implementation of the ADER-DG- $\mathbb{P}_N$  method is correct.

## 6.2 One-dimensional Riemann problems

Obtaining a correct solution to the problem of advection of a sine wave made it possible to determine the correctness of the software implementation of the ADER-DG- $\mathbb{P}_N$  method. However, numerical simulation of detonation waves requires clarification of the correctness of the full software implementation of the ADER-DG- $\mathbb{P}_N$  method with a posteriori sub-cell ADER-WENO finite-volume limiting for simulation of flows with discontinuities in the solution.

This subsection presents the results of calculating classical test cases based on exactly solvable classical one-dimensional Riemann problems [53]. Verification and testing of the developed software implementation in this work was carried out on four gas-dynamic tests [53]: the classical Sod and Lax problems (1 and 2 tests), and the problem with two shock waves (3 test), the problem with two strong rarefaction waves (4 test). The spatial domain of the flow was chosen as  $\Omega = [0, 1]$ . The initial discontinuity was located at the coordinate  $x_c = 0.5$ . The initial conditions in the two-dimensional Riemann problems were chosen in the following form:

$$(\rho, u, p)(x, t = 0) = \begin{cases} (\rho_L, u_L, p_L), & \text{if } x \leq 0.5; \\ (\rho_R, u_R, p_R), & \text{if } x > 0.5; \end{cases} \quad (53)$$

where the parameter values  $(\rho_L, u_L, p_L)$  and  $(\rho_R, u_R, p_R)$  correspond to the state of the flow to the left and right of the discontinuity. Data for the parameter values  $(\rho, u, p)$  of these four Riemann problem tests are presented in Table 9. The boundary conditions were chosen as free outflow conditions. The final time of the simulation was chosen as  $t_{\text{final}} = 0.15$  for all four tests. The adiabatic index  $\gamma = 1.4$ . The Courant number  $\text{CFL} = 0.4$ .

Table 9: Data for one-dimensional Riemann problem tests. The parameter values  $(\rho_L, u_L, p_L)$  correspond to the state of the flow to the left of the discontinuity; the parameter values  $(\rho_R, u_R, p_R)$  correspond to the state of the flow to the right of the discontinuity.

Test	$\rho_L$	$u_L$	$p_L$	$\rho_R$	$u_R$	$p_R$
1	1.000	0.000	1.000	0.125	0.000	0.100
2	0.445	0.698	3.528	0.500	0.000	0.571
3	1.000	+1.000	1.000	1.000	-1.000	1.000
4	1.000	-1.000	1.000	1.000	+1.000	1.000

Numerical solution of the classical Sod, Lax, two shock waves and two rarefaction waves problems obtained using the ADER-DG- $\mathbb{P}_9$  method with a posteriori limitation of the solution by a ADER-WENO2 finite-volume limiter on mesh with 100 cells is presented in Figure 3.

The one-dimensional flow that occurs in the Sod problem contains a shock wave, a contact discontinuity, and a rarefaction wave. The obtained coordinate dependencies show that the shock front and contact discontinuity are resolved in the solution with an accuracy of one mesh cell. In this case, the width of the contact discontinuity does not increase over time, which is often characteristic of first- and second-order methods. The contact discontinuity does not appear in any way in the coordinate dependence of pressure  $p$  in the form of non-physical artifacts. The one-dimensional flow that arises in the Lax problem is also characterized by a shock wave, a contact discontinuity and a rarefaction wave, however, compared to the Sod problem, it is much more difficult to solve this problem by high-order methods. The obtained coordinate dependencies demonstrate properties of the numerical solution similar to the solution to the Sod problem – the shock wave and contact discontinuity are resolved with an accuracy of one mesh cell. An important feature of the numerical solution of the Sod and Lax problems is that in the solution only two troubled cells arise at each time step grid, as can be seen from the presented results for the troubled cells indicator  $\beta$ . Troubled cells are formed only in the coordinate vicinity of the shock wave front, while in the vicinity of the contact discontinuity, as well as the boundary characteristics of the rarefaction wave, troubled cells are not formed.

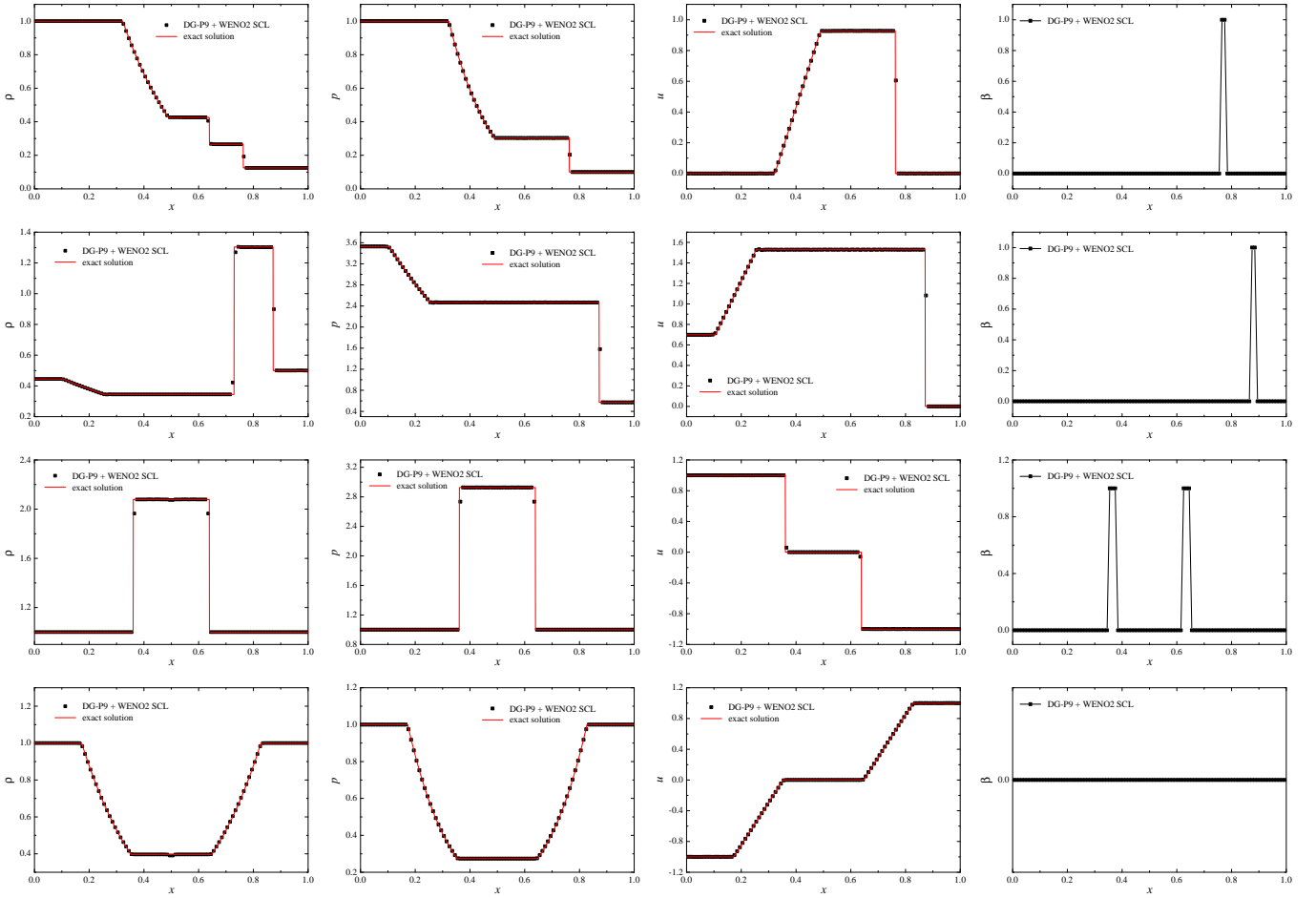


Figure 3: Numerical solution of the classical Sod, Lax, two shock waves problems and two rarefaction waves (from top to bottom) obtained using the ADER-DG- $\mathbb{P}_9$  method with a posteriori limitation of the solution by a ADER-WENO2 finite-volume limiter on mesh with 100 cells (a detailed statement of the problem is presented in the text). The graphs show the coordinate dependencies of density  $\rho$ , pressure  $p$ , flow velocity  $u$  and troubled cells indicator  $\beta$  (from left to right) at the final time  $t_{\text{final}} = 0.15$ . The black square symbols represent the numerical solution; the red solid lines represents the exact analytical solution of the problem.

The one-dimensional flow that occurs in Test 3 contains two symmetrical shock waves. Shock waves are resolved in a numerical solution with an accuracy of one mesh cell, while two troubled cells are formed in the vicinity of the shock wave fronts. The features of shock wave resolution in Test 3 are, in general, not different from the shock wave resolution in the Sod and Lax problems. The one-dimensional flow that occurs in Test 4 contains two symmetrical rarefaction waves. The presented results show that the main features of a flow with two rarefaction waves are resolved quite accurately in the numerical solution. It should also be noted that in this test case the limiter was not called – there are no grid cells, the troubled cells indicator  $\beta = 0$  is everywhere. It can also be noted that on the coordinate dependence of the density at the point of the initial position of the discontinuity, one can observe a small area of convexity downwards, the size of which is two cells. The features of the resolution of rarefaction waves in Test 4, in general, are not different from the resolution of rarefaction waves in the Sod and Lax problems.

As a result of the analysis, we can conclude that the developed software implementation of the ADER-DG- $\mathbb{P}_N$  method with a posteriori limitation of the solution by an ADER-WENO finite-volume limiter makes it possible to obtain numerical solutions to one-dimensional problems that are characterized by the appearance of discontinuous components in the solution. The properties of the numerical solution correspond to the results presented in the basic works [6, 10].

### 6.3 Kelvin-Helmholtz instability problem

The evolution of the Kelvin-Helmholtz instability was considered as a two-dimensional problem. The formation of a vortex street in a shear layer significantly depends on the dissipative properties of the numerical method used. In the one-dimensional Riemann problems discussed above, it was shown that contact discontinuities were resolved very well by the method, while the contact discontinuity region did not form troubles for mesh cells. Two-dimensional tangential discontinuities in gas dynamics exhibit instability to small perturbations of the discontinuity, accompanied by the generation of vortices that form an irregular structure of multiple vortices with fractal properties, which in dynamic evolution form a regular structure of large vortices in the form of a shifted sequence [54].

In this work, the problem statement was chosen in the form proposed in the work [54] and used in the work [55]. The coordinate domain was chosen in the form of a rectangle  $\Omega = [0, 2] \times [0, 1]$  with periodic boundary conditions, unlike the works [54, 55]



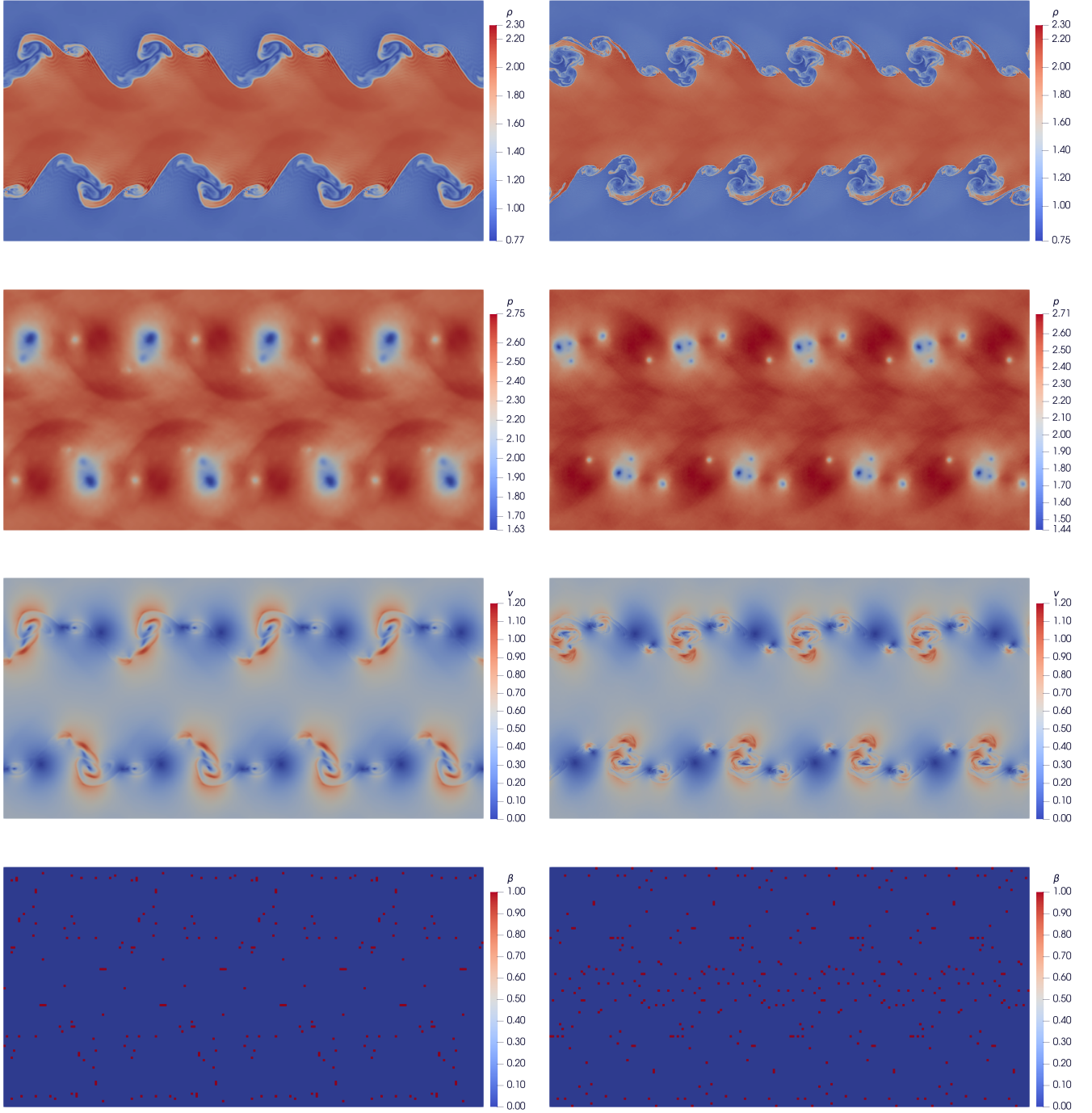


Figure 4: Numerical solution of the two-dimensional Kelvin-Helmholtz instability problem (a detailed statement of the problem is presented in the text) obtained using the ADER-DG- $\mathbb{P}_2$  (left) and ADER-DG- $\mathbb{P}_5$  (right) methods on mesh with  $200 \times 100$  cells at the time  $t = 0.8$ . The graphs show the coordinate dependencies of the subcells finite-volume representation of density  $\rho$ , pressure  $p$ , flow velocity magnitude  $v$  and troubled cells indicator  $\beta$  (bottom).

where a square unit domain was chosen. The initial conditions in the two-dimensional Kelvin-Helmholtz instability problem were chosen in the form [55]:

$$\begin{aligned}
 p(x, y, t = 0) &= 2.5; \\
 \rho(x, y, t = 0) &= \begin{cases} 2, & \text{if } 0.25 < y < 0.75; \\ 1, & \text{if } y \leq 0.25 \vee y \geq 0.75; \end{cases} \\
 u(x, y, t = 0) &= \begin{cases} -0.5, & \text{if } 0.25 < y < 0.75; \\ +0.5, & \text{if } y \leq 0.25 \vee y \geq 0.75; \end{cases} \\
 v(x, y, t = 0) &= v_0 \sin(4\pi x) \left\{ \exp\left(-\frac{(y - 0.25)^2}{2\sigma^2}\right) + \exp\left(-\frac{(y - 0.75)^2}{2\sigma^2}\right) \right\};
 \end{aligned} \tag{54}$$

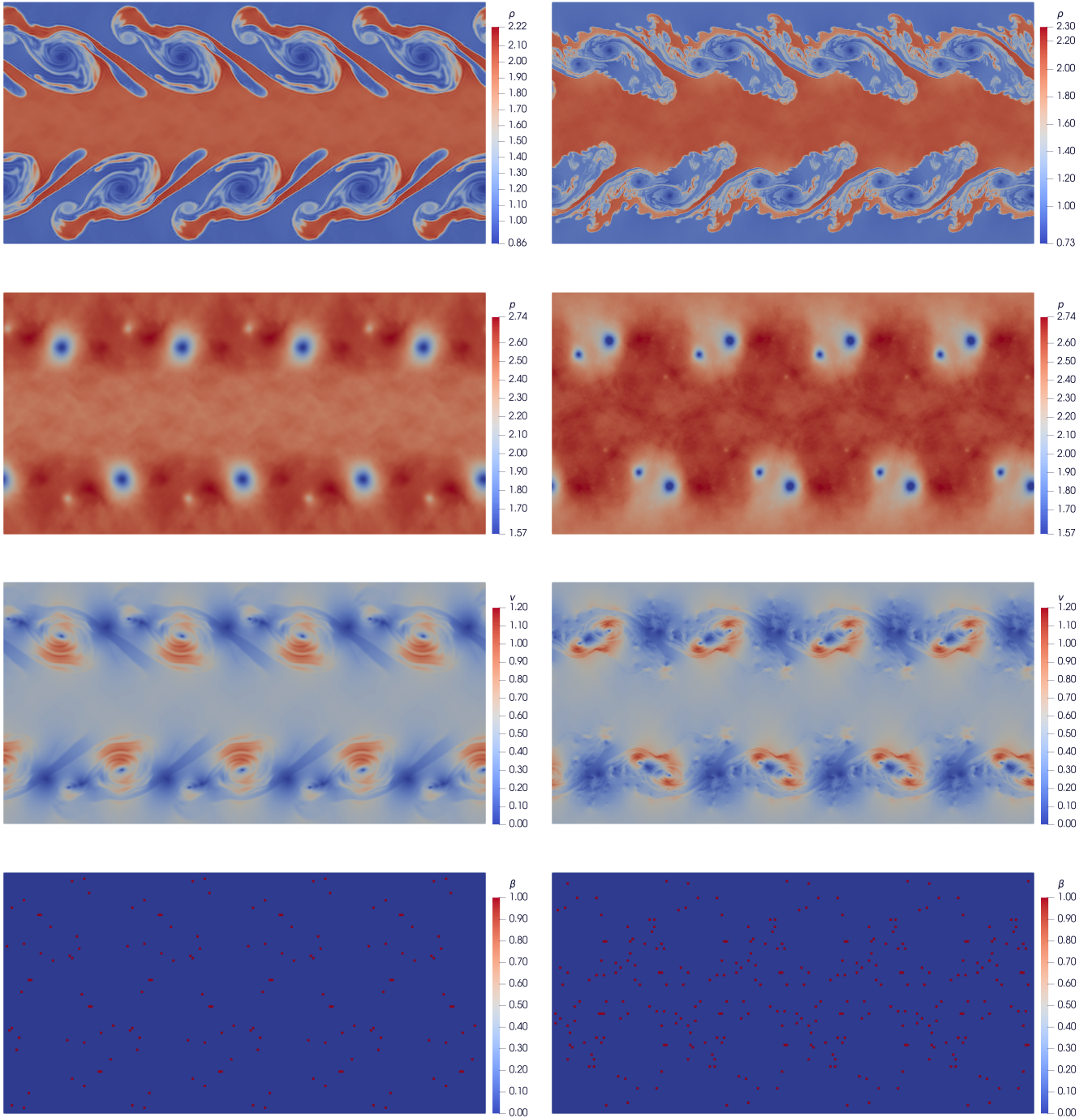


Figure 5: Numerical solution of the two-dimensional Kelvin-Helmholtz instability problem (a detailed statement of the problem is presented in the text) obtained using the ADER-DG- $\mathbb{P}_2$  (left) and ADER-DG- $\mathbb{P}_5$  (right) methods on mesh with  $200 \times 100$  cells at the time  $t = 2.0$ . The graphs show the coordinate dependencies of the subcells finite-volume representation of density  $\rho$ , pressure  $p$ , flow velocity magnitude  $v$  and troubled cells indicator  $\beta$  (bottom).

where  $v_0 = 0.1$  and  $\sigma = 0.05/\sqrt{2}$ , the adiabatic index  $\gamma = 1.4$ . The Courant number  $\text{CFL} = 0.4$ .

Numerical solutions were obtained on a  $200 \times 100$  mesh by the ADER-DG- $\mathbb{P}_5$  method. The ADER-WENO2 finite-volume method was used as a posteriori limiter. The main results obtained are presented in Figure 4 at the time  $t = 0.8$  and in Figure 5 at the time  $t = 2.0$ . To quantify the accuracy of the numerical solution, the results in the case of the ADER-DG- $\mathbb{P}_2$  method are also presented for comparison.

The presented results allowed to conclude that the ADER-DG- $\mathbb{P}_5$  method with a posteriori ADER-WENO2 finite-volume limitation allows us to obtain a solution of very high accuracy for the selected size of the spatial mesh  $200 \times 100$ . A direct comparison with the solution presented in the work [55] seems pointless, because it, of course, has much greater accuracy, which is associated with the use of AMR and a much larger spatial mesh size. However, taking into account the differences between spatial meshes, it can be said that the solution in this work agrees well with the results presented in the work [55].

In the numerical solution obtained using the ADER-DG- $\mathbb{P}_5$  method, a high accuracy of resolution of small-scale eddies,

significantly smaller than the coordinate step of the spatial mesh, is observed. In dynamics, an evolutionary process of the formation of a small-scale vortex structure is observed, followed by the coarsening of small-scale disturbances into large vortex structures. The accuracy of the resolution of the vortex structures of the shear layer is clearly visible in the coordinate dependence of the pressure  $p$ , where the cores of the main vortex structures correspond to local pressure minima.

The comparison with the results obtained using the ADER-DG- $\mathbb{P}_2$  shows that the use of  $N = 2$  leads to a significantly less accurate resolution of the vortex generation process, which, in principle, was initially expected. However, it should be noted that the numerical solution in the case of  $N = 2$  correctly resolves large-scale vortex structures – a direct comparison of the coordinate dependencies of the density shows that large-scale vortex structures are located in approximately the same coordinates in the numerical solution and demonstrate similar dynamics as in the case of the solution obtained using the ADER-DG- $\mathbb{P}_5$  method. In numerical solution obtained using the ADER-DG- $\mathbb{P}_2$ , premature merging of vortex structures is observed, which are resolved separately for a long time in numerical solution obtained using the ADER-DG- $\mathbb{P}_5$ .

It should be noted that there are very few troubled cells in the solution and all of them are irregularly distributed over the spatial mesh. This is due to the fact that in solving the problem, shock waves of significant amplitude are not formed, the front of which could be distinguished against the general background of the flow. This result applies to both method ADER-DG- $\mathbb{P}_5$  and method ADER-DG- $\mathbb{P}_2$ . However, in the case of method ADER-DG- $\mathbb{P}_2$ , there are usually slightly more troubled cells than in the case of method ADER-DG- $\mathbb{P}_5$ .

## 7 Computational costs

The main objective of this work was to integrate the interface of high-performance computing of the BLAS into the implementation of the finite-element numerical methods ADER-DR and finite-volume numerical methods ADER-WENO. Therefore, it was of interest to determine the computational costs and compare them with the computational costs of other implementations, which allowed us to determine the computational performance of the developed efficient software implementation. This Section presents a comparison of the computational costs of the ADER-DG- $\mathbb{P}_N$  method with a posteriori limitation of the solution by finite-volume ADER-WENO limiter obtained in four main cases:

1. Implementation without the use of BLAS interface (completely naive implementation, CN implementation), in which the formula apparatus of the numerical methods of the ADER family, described in detail in the text above, was used, which was explicitly implemented in the computational code. The explicit optimizations of the software implementation, including loop reordering to improve memory locality, were not used.
2. Optimized naive implementation (ON implementation), which used the implementation proposed in this paper, however, for the separate `gemm` function a naive implementation of matrix-matrix multiplication was used (taking into account the leading dimensions of matrices in BLAS), which has locality in memory and uses a simple memory access pattern.
3. Implementation, using general BLAS `gemm` function of the Intel MKL software library (GB implementation), included in the Intel oneAPI toolkit, while the optimizations available using the `MKL_DIRECT_CALL_JIT` option, as well as the batch and strided `gemm` functions, were not used. It should be noted right away that the computational costs obtained using OpenBLAS in this case are similar to the computational costs obtained using the general BLAS functions of Intel MKL.
4. Implementation, using the JIT `gemm` functions of the Intel MKL software library (JB implementation), included in the Intel oneAPI toolkit, optimized for operations with small matrices. The jitters were created in advance due to the known parameters of all necessary calls of the `gemm` functions. The choice between `MKL JIT` and `libxsmm` in favor of `MKL JIT` is related to that the use of `libxsmm` has already been presented in detail in the works [16, 19].

The software implementation of the method was developed using the C++ programming language. Multithreading and multiprocessing execution was organized using the OpenMP and MPI interfaces. Software implementations were carried out separately for one-dimensional, two-dimensional and three-dimensional problems. All calculations were carried out on the HEDT class workstation with Intel i9-10980xe processor and 256 GB RAM. The computational costs were determined for calculations with single MPI process and 18 OpenMP threads.

The compilation and linking of the project's program code was performed using compiler `icpx`, included in the Intel oneAPI toolkit. The options for strict compliance with the C++23 standard were selected; it was from this standard that the possibility of effective use of `goto` to the label at end of compound statement for breaking a nested loop when checking the admissibility criteria was taken, which is recommended by ES.76 C++ Core Guidelines recommendation. The `O3`, `funroll-loops`, `xHOST` and `qopt-zmm-usage=high` optimization options were selected. The optimization report, generated by using `qopt-report` option, showed that for the selected optimization options, in the case of an optimized naive implementation (ON), the compiler managed to vectorized the loops associated with stream triad, included in the inner loop of the `gemm` function using a simple memory access pattern. In case of completely naive implementation (CN), the compiler optimization report showed unrolling and vectorization of only some loops.

The computational costs were determined using the problem of advection of a periodic wave in two-dimensional and three-dimensional formulations of the problem. The initial conditions were chosen the same to the problem of sine wave advection considered in Subsection 6.1. Therefore, this problem allowed us to carry out a separate study both for the finite-element method ADER-DG, the use of which in the case of discontinuous solutions would necessarily require the use of a limiter, and for the finite-volume method ADER-WENO. The presented problem has a smooth solution, therefore in the numerical methods ADER-DG trouble cells do not occur and the limiter was not activated, however, the numerical solution of the problem was obtained using the full implementation of the ADER-DG method with a posteriori correction of the solution in subcells by the finite-volume ADER-WENO limiter, therefore, despite the inactivity of the limiter, the admissibility criteria were fully verified at each time step. In the case of obtaining a numerical solution using the finite-volume ADER-WENO method, the same

software implementation of the ADER-DG method with a posteriori correction of the solution in subcells by the finite-volume ADER-WENO limiter was used, however, the calculation of the candidate solution by the ADER-DG method was disabled, and the admissibility criteria explicitly designated all cells as trouble. In this case, the “basic” polynomial degree  $N = 2$  was chosen for the ADER-DG method, for which the subgrid size was  $N_s = 2N + 1 = 5$  in each cell, so the choice of the mesh with sizes 1, 2, 3, 4 in each coordinate direction allowed us to perform calculations by the finite-volume ADER-WENO method on a mesh of 5, 10, 15, 20, respectively. The subgrid size of  $N_s = 5$  in each direction was sufficient to perform dimension-by-dimension WENO reconstruction for methods ADER-WENO2, ADER-WENO3, ADER-WENO4 (and also for ADER-WENO5). Therefore, in the case of determining the computational costs of the finite-volume ADER-WENO method, the number of mesh cells is understood as the number of mesh subcells.

Table 10: The absolute computational costs (CPU time measured in seconds)  $T_{\text{JIT}}$ ,  $T_{\text{GEN}}$ ,  $T_{\text{ON}}$ ,  $T_{\text{CN}}$  for ADER-DG- $\mathbb{P}_N$  method for two-dimensional sine wave advection problem. The relative computational costs  $\Upsilon_{\text{JIT}}$ ,  $\Upsilon_{\text{GEN}}$ ,  $\Upsilon_{\text{ON}}$ ,  $\Upsilon_{\text{CN}}$  are the absolute computational costs  $T$  normalized to  $T_{\text{JIT}}$ .

	cells	$T_{\text{JIT}}$	$T_{\text{GEN}}$	$T_{\text{ON}}$	$T_{\text{CN}}$	$\Upsilon_{\text{JIT}}$	$\Upsilon_{\text{GEN}}$	$\Upsilon_{\text{ON}}$	$\Upsilon_{\text{CN}}$
DG- $\mathbb{P}_1$	$4^2$	3.50E-02	7.40E-02	3.70E-02	5.40E-02	1.00	2.11	1.06	1.54
	$8^2$	7.30E-02	1.50E-01	8.20E-02	1.23E-01	1.00	2.05	1.12	1.68
	$12^2$	1.43E-01	2.61E-01	1.61E-01	2.34E-01	1.00	1.83	1.13	1.64
	$16^2$	2.32E-01	4.05E-01	2.64E-01	3.78E-01	1.00	1.75	1.14	1.63
DG- $\mathbb{P}_2$	$4^2$	7.50E-02	1.84E-01	9.80E-02	1.54E-01	1.00	2.45	1.31	2.05
	$8^2$	1.31E-01	3.04E-01	1.66E-01	2.76E-01	1.00	2.32	1.27	2.11
	$12^2$	2.62E-01	5.94E-01	3.35E-01	5.68E-01	1.00	2.27	1.28	2.17
	$16^2$	5.16E-01	1.16E+00	6.21E-01	1.09E+00	1.00	2.26	1.20	2.11
DG- $\mathbb{P}_3$	$4^2$	1.27E-01	3.56E-01	1.91E-01	3.09E-01	1.00	2.80	1.50	2.43
	$8^2$	2.36E-01	6.06E-01	3.67E-01	6.68E-01	1.00	2.57	1.56	2.83
	$12^2$	5.03E-01	1.30E+00	8.96E-01	1.58E+00	1.00	2.59	1.78	3.13
	$16^2$	9.03E-01	2.42E+00	1.75E+00	3.27E+00	1.00	2.68	1.94	3.62
DG- $\mathbb{P}_4$	$4^2$	1.74E-01	4.78E-01	2.76E-01	4.64E-01	1.00	2.75	1.59	2.67
	$8^2$	3.82E-01	1.07E+00	7.69E-01	1.44E+00	1.00	2.80	2.01	3.78
	$12^2$	8.00E-01	2.25E+00	2.14E+00	3.58E+00	1.00	2.81	2.67	4.47
	$16^2$	1.51E+00	4.29E+00	4.39E+00	7.64E+00	1.00	2.84	2.91	5.06
DG- $\mathbb{P}_5$	$4^2$	2.89E-01	8.30E-01	5.23E-01	9.41E-01	1.00	2.87	1.81	3.26
	$8^2$	1.59E+00	4.94E+00	3.40E+00	6.59E+00	1.00	3.10	2.13	4.13
	$12^2$	3.56E+00	9.64E+00	9.15E+00	1.50E+01	1.00	2.71	2.57	4.20
	$16^2$	7.05E+00	1.86E+01	1.92E+01	3.15E+01	1.00	2.64	2.72	4.46
DG- $\mathbb{P}_6$	$4^2$	1.14E+00	2.92E+00	1.69E+00	3.34E+00	1.00	2.56	1.48	2.92
	$8^2$	3.08E+00	8.53E+00	6.77E+00	1.23E+01	1.00	2.76	2.20	3.97
	$12^2$	8.61E+00	2.04E+01	2.18E+01	3.15E+01	1.00	2.37	2.53	3.66
	$16^2$	1.86E+01	4.44E+01	4.86E+01	7.23E+01	1.00	2.39	2.62	3.89
DG- $\mathbb{P}_7$	$4^2$	1.56E+00	4.82E+00	2.66E+00	5.73E+00	1.00	3.09	1.70	3.67
	$8^2$	5.39E+00	1.46E+01	9.14E+00	2.19E+01	1.00	2.71	1.70	4.06
	$12^2$	1.65E+01	4.33E+01	2.81E+01	6.48E+01	1.00	2.63	1.70	3.93
	$16^2$	3.91E+01	9.79E+01	6.53E+01	1.51E+02	1.00	2.50	1.67	3.88
DG- $\mathbb{P}_8$	$4^2$	2.37E+00	7.17E+00	4.18E+00	1.06E+01	1.00	3.02	1.76	4.45
	$8^2$	1.11E+01	2.86E+01	1.90E+01	5.60E+01	1.00	2.59	1.72	5.05
	$12^2$	3.37E+01	8.05E+01	5.81E+01	1.63E+02	1.00	2.39	1.72	4.84
	$16^2$	7.60E+01	1.82E+02	1.35E+02	3.85E+02	1.00	2.40	1.77	5.06
DG- $\mathbb{P}_9$	$4^2$	3.30E+00	9.99E+00	6.13E+00	1.63E+01	1.00	3.03	1.86	4.94
	$8^2$	1.85E+01	4.60E+01	3.22E+01	9.07E+01	1.00	2.48	1.74	4.90
	$12^2$	5.80E+01	1.36E+02	1.07E+02	2.72E+02	1.00	2.34	1.84	4.69
	$16^2$	1.45E+02	3.10E+02	2.47E+02	6.43E+02	1.00	2.13	1.70	4.42

The computational costs of the finite-element method ADER-DR for polynomial degrees  $N = 1, \dots, 9$  and the finite-volume method ADER-WENO for polynomial degrees  $N = 1, \dots, 3$  were separately investigated. In the context of using numerical methods of ADER, the finite-volume method ADER-WENO is usually used as a limiter, and the ADER-WENO3 method with  $N = 2$  is mainly used [10, 11], therefore, the computational costs of polynomial degrees  $N \geq 4$  were not investigated. In the basic works [8, 9] in which the numerical method ADER-WENO was developed, methods with degrees  $N \leq 3$  were used. The computational costs of two-dimensional and three-dimensional implementation were also investigated separately. Computational costs were determined not only for different polynomial degrees  $N$ , but also for different mesh sizes.

Absolute computational costs  $T$  were determined as the CPU time (measured in seconds) to perform the calculations in the four main software implementations:  $T_{\text{JB}}$ ,  $T_{\text{GB}}$ ,  $T_{\text{ON}}$ ,  $T_{\text{CN}}$ , which correspond to variants JB, GB, ON, CN, introduced above in the text, respectively. To compare the obtained results and determine the increase of performance as a result of using the BLAS interface integration method presented in this paper, relative computational costs  $\Upsilon = T/T_{\text{JB}}$  were also determined:  $\Upsilon_{\text{JB}}$ ,  $\Upsilon_{\text{GB}}$ ,  $\Upsilon_{\text{ON}}$ ,  $\Upsilon_{\text{CN}}$ , defined as absolute computational costs  $T$  normalized by the computational costs  $T_{\text{JB}}$  of the JB implementation, therefore  $\Upsilon_{\text{JB}} = 1$ . Calculations of absolute computational costs were made based on averaging the CPU time of calculations

Table 11: The absolute computational costs (CPU time measured in seconds)  $T_{\text{JIT}}$ ,  $T_{\text{GEN}}$ ,  $T_{\text{ON}}$ ,  $T_{\text{CN}}$  for ADER-DG- $\mathbb{P}_N$  method for three-dimensional sine wave advection problem. The relative computational costs  $\Upsilon_{\text{JIT}}$ ,  $\Upsilon_{\text{GEN}}$ ,  $\Upsilon_{\text{ON}}$ ,  $\Upsilon_{\text{CN}}$  are the absolute computational costs  $T$  normalized to  $T_{\text{JIT}}$ .

	cells	$T_{\text{JIT}}$	$T_{\text{GEN}}$	$T_{\text{ON}}$	$T_{\text{CN}}$	$\Upsilon_{\text{JIT}}$	$\Upsilon_{\text{GEN}}$	$\Upsilon_{\text{ON}}$	$\Upsilon_{\text{CN}}$
DG- $\mathbb{P}_1$	$4^3$	7.38E-01	2.44E+00	1.34E+00	2.03E+00	1.00	3.31	1.82	2.76
	$5^3$	9.38E-01	3.29E+00	1.72E+00	2.72E+00	1.00	3.50	1.83	2.90
	$6^3$	1.54E+00	4.46E+00	2.40E+00	3.61E+00	1.00	2.89	1.55	2.34
	$7^3$	1.31E+00	4.50E+00	2.20E+00	3.76E+00	1.00	3.44	1.68	2.87
DG- $\mathbb{P}_2$	$4^3$	2.01E+00	7.14E+00	3.78E+00	6.11E+00	1.00	3.56	1.88	3.04
	$5^3$	2.39E+00	8.90E+00	4.43E+00	7.60E+00	1.00	3.73	1.85	3.18
	$6^3$	2.84E+00	1.26E+01	6.82E+00	1.10E+01	1.00	4.43	2.40	3.88
	$7^3$	3.00E+00	1.37E+01	7.06E+00	1.30E+01	1.00	4.56	2.35	4.34
DG- $\mathbb{P}_3$	$4^3$	5.80E+00	1.54E+01	8.01E+00	1.38E+01	1.00	2.66	1.38	2.38
	$5^3$	4.52E+00	1.38E+01	7.62E+00	1.41E+01	1.00	3.06	1.69	3.12
	$6^3$	8.75E+00	3.20E+01	1.75E+01	3.17E+01	1.00	3.66	2.00	3.63
	$7^3$	1.13E+01	3.60E+01	2.05E+01	3.91E+01	1.00	3.19	1.82	3.47
DG- $\mathbb{P}_4$	$4^3$	8.49E+00	2.99E+01	1.68E+01	2.92E+01	1.00	3.52	1.97	3.44
	$5^3$	1.25E+01	3.94E+01	2.37E+01	4.21E+01	1.00	3.15	1.90	3.36
	$6^3$	1.56E+01	5.16E+01	3.34E+01	6.16E+01	1.00	3.31	2.14	3.95
	$7^3$	2.07E+01	6.75E+01	4.76E+01	9.22E+01	1.00	3.25	2.30	4.45
DG- $\mathbb{P}_5$	$4^3$	1.55E+01	5.46E+01	3.31E+01	5.86E+01	1.00	3.52	2.14	3.77
	$5^3$	2.16E+01	6.89E+01	4.83E+01	8.65E+01	1.00	3.18	2.23	4.00
	$6^3$	2.84E+01	8.43E+01	7.17E+01	1.30E+02	1.00	2.97	2.52	4.58
	$7^3$	4.08E+01	1.36E+02	1.12E+02	2.23E+02	1.00	3.34	2.75	5.48
DG- $\mathbb{P}_6$	$4^3$	2.31E+01	7.22E+01	5.26E+01	9.05E+01	1.00	3.13	2.28	3.92
	$5^3$	3.40E+01	1.03E+02	8.69E+01	1.50E+02	1.00	3.03	2.56	4.42
	$6^3$	5.23E+01	1.60E+02	1.48E+02	2.61E+02	1.00	3.05	2.83	4.99
	$7^3$	7.76E+01	2.32E+02	2.43E+02	4.32E+02	1.00	2.98	3.13	5.57
DG- $\mathbb{P}_7$	$4^3$	3.87E+01	1.14E+02	7.66E+01	1.54E+02	1.00	2.95	1.98	3.98
	$5^3$	5.94E+01	1.69E+02	1.25E+02	2.60E+02	1.00	2.84	2.11	4.38
	$6^3$	9.64E+01	2.70E+02	2.10E+02	4.63E+02	1.00	2.80	2.17	4.80
	$7^3$	1.50E+02	4.20E+02	3.36E+02	7.93E+02	1.00	2.80	2.25	5.30
DG- $\mathbb{P}_8$	$4^3$	8.31E+01	2.00E+02	1.37E+02	4.05E+02	1.00	2.41	1.65	4.87
	$5^3$	1.32E+02	2.92E+02	2.27E+02	7.58E+02	1.00	2.20	1.71	5.73
	$6^3$	1.98E+02	4.07E+02	3.95E+02	1.36E+03	1.00	2.06	1.99	6.86
	$7^3$	2.84E+02	6.78E+02	6.72E+02	2.41E+03	1.00	2.39	2.36	8.48
DG- $\mathbb{P}_9$	$4^3$	1.55E+02	3.04E+02	2.30E+02	6.64E+02	1.00	1.97	1.49	4.29
	$5^3$	2.67E+02	4.83E+02	4.44E+02	1.29E+03	1.00	1.81	1.66	4.84
	$6^3$	5.30E+02	8.09E+02	7.60E+02	2.52E+03	1.00	1.53	1.43	4.75
	$7^3$	8.68E+02	1.25E+03	1.33E+03	4.27E+03	1.00	1.44	1.53	4.92

Table 12: The absolute computational costs (CPU time measured in seconds)  $T_{\text{JIT}}$ ,  $T_{\text{GEN}}$ ,  $T_{\text{ON}}$ ,  $T_{\text{CN}}$  for finite-volume ADER-WENO( $N+1$ ) method for two-dimensional sine wave advection problem. The relative computational costs  $\Upsilon_{\text{JIT}}$ ,  $\Upsilon_{\text{GEN}}$ ,  $\Upsilon_{\text{ON}}$ ,  $\Upsilon_{\text{CN}}$  are the absolute computational costs  $T$  normalized to  $T_{\text{JIT}}$ .

	cells	$T_{\text{JIT}}$	$T_{\text{GEN}}$	$T_{\text{ON}}$	$T_{\text{CN}}$	$\Upsilon_{\text{JIT}}$	$\Upsilon_{\text{GEN}}$	$\Upsilon_{\text{ON}}$	$\Upsilon_{\text{CN}}$
WENO2	$5^2$	1.70E-02	4.80E-02	2.50E-02	3.80E-02	1.00	2.82	1.47	2.24
	$10^2$	4.50E-02	9.80E-02	5.10E-02	8.10E-02	1.00	2.18	1.13	1.80
	$15^2$	6.80E-02	1.62E-01	9.90E-02	1.45E-01	1.00	2.38	1.46	2.13
	$20^2$	1.35E-01	2.53E-01	1.49E-01	2.25E-01	1.00	1.87	1.10	1.67
WENO3	$5^2$	3.20E-02	1.10E-01	6.90E-02	1.17E-01	1.00	3.44	2.16	3.66
	$10^2$	7.20E-02	2.44E-01	1.52E-01	2.57E-01	1.00	3.39	2.11	3.57
	$15^2$	1.74E-01	4.96E-01	3.34E-01	5.12E-01	1.00	2.85	1.92	2.94
	$20^2$	3.93E-01	8.04E-01	5.27E-01	9.65E-01	1.00	2.05	1.34	2.46
WENO4	$5^2$	6.00E-02	2.43E-01	2.02E-01	3.62E-01	1.00	4.05	3.37	6.03
	$10^2$	1.45E-01	5.45E-01	4.96E-01	8.29E-01	1.00	3.76	3.42	5.72
	$15^2$	2.57E-01	9.28E-01	7.53E-01	1.41E+00	1.00	3.61	2.93	5.50
	$20^2$	5.19E-01	1.61E+00	1.41E+00	2.73E+00	1.00	3.11	2.72	5.27

for more than 5 program runs, while the total execution time was taken to be at least 5 minutes, therefore samples executed for less than 1 second were repeated more than 300 times to average the execution time.

The obtained values of absolute  $T$  and relative computational costs  $\Upsilon$  for the finite-element ADER-DG method in the two-dimensional case are presented in Table 10 and in the three-dimensional case are presented in Table 11. The obtained values of

Table 13: The absolute computational costs (CPU time measured in seconds)  $T_{\text{JIT}}$ ,  $T_{\text{GEN}}$ ,  $T_{\text{ON}}$ ,  $T_{\text{CN}}$  for finite-volume ADER-WENO( $N + 1$ ) method for three-dimensional sine wave advection problem. The relative computational costs  $\Upsilon_{\text{JIT}}$ ,  $\Upsilon_{\text{GEN}}$ ,  $\Upsilon_{\text{ON}}$ ,  $\Upsilon_{\text{CN}}$  are the absolute computational costs  $T$  normalized to  $T_{\text{JIT}}$ .

	cells	$T_{\text{JIT}}$	$T_{\text{GEN}}$	$T_{\text{ON}}$	$T_{\text{CN}}$	$\Upsilon_{\text{JIT}}$	$\Upsilon_{\text{GEN}}$	$\Upsilon_{\text{ON}}$	$\Upsilon_{\text{CN}}$
WENO2	$5^3$	5.64E-01	2.16E+00	1.06E+00	1.68E+00	1.00	3.84	1.89	2.98
	$10^3$	1.61E+00	4.99E+00	2.60E+00	3.99E+00	1.00	3.09	1.61	2.47
	$15^3$	6.28E+00	1.70E+01	9.28E+00	1.36E+01	1.00	2.71	1.48	2.17
	$20^3$	1.80E+01	5.38E+01	2.75E+01	3.88E+01	1.00	2.99	1.52	2.15
WENO3	$5^3$	1.76E+00	7.92E+00	4.61E+00	7.80E+00	1.00	4.50	2.62	4.43
	$10^3$	4.26E+00	1.84E+01	1.04E+01	1.81E+01	1.00	4.31	2.45	4.25
	$15^3$	1.82E+01	6.28E+01	3.88E+01	6.13E+01	1.00	3.45	2.13	3.37
	$20^3$	6.49E+01	2.21E+02	1.33E+02	2.35E+02	1.00	3.41	2.04	3.61
WENO4	$5^3$	4.67E+00	2.08E+01	1.63E+01	2.70E+01	1.00	4.46	3.48	5.79
	$10^3$	1.39E+01	4.93E+01	3.84E+01	6.51E+01	1.00	3.53	2.75	4.67
	$15^3$	5.77E+01	1.73E+02	1.38E+02	2.18E+02	1.00	3.00	2.40	3.77
	$20^3$	1.89E+02	5.75E+02	4.62E+02	7.87E+02	1.00	3.05	2.45	4.17

absolute and relative computational costs for the finite-volume ADER-WENO method in the two-dimensional case are presented in Table 12 and in the three-dimensional case are presented in Table 13.

Note that the increase in absolute computational costs  $T$  for a certain value of the polynomial degree  $N$  is slower than the growth in the number of mesh cells, which is due to the existence of additional calculations associated with the calculation of initial conditions – they are calculated only once, so there is a decrease in the relative contribution of this procedure with an increase in the number of time steps with a decrease in the coordinate step  $h$ ; associated with the calculation of boundary conditions – the boundary has a dimension one less than the dimension of the problem, and the growth in the number of boundary cells with an increase in the mesh size has a different dimensional asymptotics; as well as with a change in the number of LST-DG predictor iterations – for very coarse meshes, the number of iterations is close to the largest expected value  $\sim N + 1$ , and with mesh refinement, the relative variability of the smooth solution in the cell decreases, and with it the number of iterations decreases.

The relative performance gain depends significantly on the polynomials degree  $N$ , that determine the sizes of the matrices with which the solution representations are convolved, and on the size of the spatial mesh on which the calculations are performed. There is also a significant dependence on the spatial dimension of the problem and a specific numerical method – finite-element ADER-DG or finite-volume ADER-WENO. It should be noted that the nature of these dependencies is significantly non-monotonic, however, these patterns can be explained in the context of reducing the overhead costs of function calls (especially in the case of the GB implementation) and changing the number of `gemm` function calls.

The obtained relative values of computational costs  $\Upsilon$  allowed to immediately conclude that the implementation presented in this work, based on the use of the JIT functions of the BLAS, outperforms both the implementation based on the general BLAS functions and the naive implementations using explicit multiplications and summations in simple loops. The JB implementation outperforms the ON implementation in computation speed by 1.5-2.5 times in most cases, the GB implementation by 1.5-4.0 times, and the CN implementation by 2-8 times. In this case, this advantage is observed precisely in the computational costs of executing the entire algorithm, and not just matrix-matrix multiplications.

In almost all cases, the next smallest computational cost is the implementation of ON based on a simply optimized `gemm` function. In the case of the ADER-DG- $\mathbb{P}_1$  method for two-dimensional problem, the implementation of ON is only 6-14% slower than the JB implementation, which is due to the relatively small number of calls to the `gemm` function in loops and the commensurability of the performance of the functions in the case of multiplication by a  $2 \times 2$  matrix. However, in the case of ADER-DG- $\mathbb{P}_1$  method for three-dimensional problem, the differences are already 1.5-2.0 times. With an increase in the polynomials degree  $N$ , there is a relative increase in the computational costs of the implementation of ON compared to JB. The ON implementation shows results slower than GB only in case of ADER-DG- $\mathbb{P}_6$  method for three-dimensional problem with mesh size  $7^3$ . It should be noted that the simplicity of the implementation of ON vs JB is not great – it is still necessary to explicitly use the `gemm` function, only with a simple implementation instead of creating, storing and destroying jitters in JB implementation. In this case, the relative efficiency of ON compared to CN is due to the allocation of a separate `gemm` function as a bottleneck in execution, and its implementation in such a way that the compiler could effectively optimize this function.

The high computational costs  $\Upsilon$  of the GB implementation are expected – the `sblas_(d)gemm` functions are originally intended for calculations with relatively large matrices, unlike JIT BLAS. However, in many of the presented cases, GB has lower computational costs compared to CN. The high computational costs  $\Upsilon$  of the CN implementation are also expected and are related to the inefficiency of compiler optimization of operations with low memory locality and very deep nested loops. However, the CN implementation is the simplest of those proposed – it is a simple coding of the formula apparatus of the numerical method.

## Conclusion

In conclusion, it should be noted that implementations of finite-element ADER-DG and finite-volume ADER-WENO methods with the LST-DG predictor based on the use of the BLAS interface were developed and proposed in this work. The use of the BLAS interface was limited to the `gemm` function only.

The proposed approach immediately operates on AoS, which makes it possible to efficiently calculate flux, source and non-conservative terms, in this case, there is no need to carry out transposition, which must be carried out in the algorithm proposed in the work [16] and implemented in the work [19]. An important difference from existing descriptions [16,19] of the use of BLAS in the implementation of numerical methods is the use of the AoS paradigm for storage the coefficients of the local discrete space-time solution  $\mathbf{q}$ .

The developed implementations for the LST-DG predictor are presented, in which the Picard iterative method was used to solve a system of nonlinear algebraic equations, a one-step discrete finite-element ADER-DG and finite-volume ADER-WENO schemes, and implementations of the suitable piecewise-constant projection operator and the suitable high order accurate reconstruction operator used in the ADER-DG method with a posteriori correction of the solution in subcells by a finite-volume limiter are also presented.

This paper presents detailed algorithms and tables with function parameters, which allow to develop effective software implementations of finite-element ADER-DG and finite-volume ADER-WENO methods with the LST-DG predictor. The calculated matrices are small matrices; at the same time, the proposed implementation makes it possible to effectively use existing JIT technologies, in particular, the JIT `gemm` from the `Intel MKL` library, designed for acceleration of small matrix multiplication.

The obtained computational costs allow to conclude, that the implementation presented in this work, outperforms the optimized naive implementation in computation speed by 1.5-2.5 times in most cases, the implementation with general BLAS functions by 1.5-4.0 times, and the completely naive implementation without the use of BLAS interface by 2-8 times.

It should be noted that the simplicity of the implementation of “optimized naive” vs. “JIT BLAS” implementation is not great – it is still necessary to explicitly use the `gemm` function, only with a simple implementation instead of creating, storing and destroying jitters in implementation with JIT BLAS. Therefore, the complexity of developing an implementation based on the approach proposed in this paper does not exceed the complexity of developing a naive optimized implementation.

Computations were carried out that showed high accuracy and convergence of numerical methods of the ADER family within the framework of this implementation with the integration of the BLAS interface, showing the correctness of the chosen implementation method.

## Acknowledgments

The reported study was supported by the Russian Science Foundation grant No. 21-71-00118:  
<https://rscf.ru/en/project/21-71-00118/>.

The author would like to thank Popova A.P. for help in correcting the English text.

## References

- [1] Titarev, V.A, Toro, E.F.: ADER: arbitrary high order Godunov approach *J. Sci. Comput.* **17**, 609 (2002)
- [2] Titarev, V.A., Toro, E.F.: ADER schemes for three-dimensional nonlinear hyperbolic systems. *J. Comput. Phys.* **204**, 715 (2005)
- [3] Dumbser, M., Enaux, C., Toro, E.F.: Finite volume schemes of very high order of accuracy for stiff hyperbolic balance laws. *J. Comput. Phys.* **227**, 3971 (2008)
- [4] Hidalgo, A., Dumbser, M.: ADER Schemes for Nonlinear Systems of Stiff Advection-Diffusion-Reaction Equations. *J. Sci. Comput.* **48**, 173 (2011)
- [5] Loubère, R., Dumbser, M., Diot, S.: A New Family of High Order Unstructured MOOD and ADER Finite Volume Schemes for Multidimensional Systems of Hyperbolic Conservation Laws. *Communications in Computational Physics.* **16**, 718 (2014)
- [6] Dumbser, M., Zanotti, O., Loubère, R., Diot, S.: A posteriori subcell limiting of the discontinuous Galerkin finite-element method for hyperbolic conservation laws. *J. Comput. Phys.* **278**, 47 (2014)
- [7] Zanotti, O., Dumbser, M.: A high order special relativistic hydrodynamic and magnetohydrodynamic code with space-time adaptive mesh refinement. *Computer Physics Communications.* **188**, 110 (2015)
- [8] Dumbser, M., Zanotti, O., Hidalgo, A., Balsara, D.S.: ADER-WENO finite-volume schemes with space-time adaptive mesh refinement. *J. Comput. Phys.* **248**, 257 (2013)
- [9] Dumbser, M., Hidalgo, A., Zanotti, O.: High order space-time adaptive ADER-WENO finite-volume schemes for non-conservative hyperbolic systems. *Comput. Methods Appl. Mech. Engrg.* **268**, 359 (2014)
- [10] Zanotti, O., Fambri, F., Dumbser, M., Hidalgo, A.: Space-time adaptive ADER discontinuous Galerkin finite element schemes with a posteriori sub-cell finite-volume limiting. *Computers & Fluids.* **118**, 204 (2015)
- [11] Fambri, F., Dumbser, M., Zanotti, O.: Space-time adaptive ADER-DG schemes for dissipative flows: Compressible Navier-Stokes and resistive MHD equations. *Computer Physics Communications.* **220**, 297 (2017)
- [12] Busto, A., Rio-Martin, L., Vazquez-Cendon, M.E., Dumbser, M.: A semi-implicit hybrid finite-volume/finite-element scheme for all Mach number flows on staggered unstructured meshes. *Applied Mathematics and Computation*, **402**, 126117 (2021).

- [13] Fambri, F., Dumbser, M., Köppel, S., Rezzolla, L., Zanotti, O.: ADER discontinuous Galerkin schemes for general-relativistic ideal magnetohydrodynamics. *MNRAS*. **477**, 4543 (2018)
- [14] Dumbser, M., Guercilena, F., Köppel, S., Rezzolla, L., Zanotti, O.: Conformal and covariant Z4 formulation of the Einstein equations: Strongly hyperbolic first-order reduction and solution with discontinuous Galerkin schemes. *Phys. Rev. D*. **97**, 084053 (2018)
- [15] Dumbser, M., Zanotti, O., Gaburro, E., Peshkov, I.: A well-balanced discontinuous Galerkin method for the first-order Z4 formulation of the Einstein-Euler system. *J. Comp. Phys.*, **504**, 112875 (2024)
- [16] Dumbser, M., Fambri, F., Tavelli, M., Bader, M., Weinzierl, T.: Efficient implementation of ADER discontinuous Galerkin schemes for a scalable hyperbolic PDE engine. *Axioms*. **7(3)**, 63 (2018)
- [17] Busto, S., Chiochetti, S., Dumbser, M., Gaburro, E., Peshkov, I.: High Order ADER Schemes for Continuum Mechanics. *Front. Phys.* **32**, 8 (2020)
- [18] Tavelli, M., Chiochetti, S., Romenski, E., Gabriel, A.A., Dumbser, M.: Space-time adaptive ADER discontinuous Galerkin schemes for nonlinear hyperelasticity with material failure. *J. Comp. Phys.*, **422**, 109758 (2020)
- [19] Reinartz, A., Charrier, D.E., Bader, M., Bovard, L., Dumbser, M., Duru, K., Fambri, F., Gabriel, A.-A., Gallard, G.-M., Köppel, S., Krenz, L., Rannabauer, L., Rezzolla, L., Samfass, P., Tavelli, M., Weinzierl, T.: ExaHyPE: An Engine for Parallel Dynamically Adaptive Simulations of Wave Problems. *Computer Physics Communications*. **254**, 107251 (2020)
- [20] Wolf, S., Galis, M., Uphoff, C., Gabriel, A.-A., Moczo P., Gregor, D., Bader, M.: An efficient ADER-DG local time stepping scheme for 3D HPC simulation of seismic waves in poroelastic media. *J. Comp. Phys.*, **455**, 110886 (2022)
- [21] Bassi, C., Busto, S., Dumbser, M.: High order ADER-DG schemes for the simulation of linear seismic waves induced by nonlinear dispersive free-surface water waves. *Applied Numerical Mathematics*, **158**, 236 (2020)
- [22] Popov, I.S.: Space-Time Adaptive ADER-DG Finite Element Method with LST-DG Predictor and a posteriori Sub-cell WENO Finite-Volume Limiting for Simulation of Non-stationary Compressible Multicomponent Reactive Flows. *J. Sci. Comput.*, **95**, 44 (2023)
- [23] Dumbser, M., Casulli, V.: A staggered semi-implicit spectral discontinuous Galerkin scheme for the shallow water equations. *Appl. Math. Comput.* **219**, 8057 (2013)
- [24] Fernandez, E.G., Diaz, M.J.C., Dumbser, M., de Luna, T.M.: An Arbitrary High Order Well-Balanced ADER-DG Numerical Scheme for the Multilayer Shallow-Water Model with Variable Density. *J. Sci. Comput.*, **90**, 52 (2022)
- [25] Montecinos, G.I., Santaca, A., Celant, M., Muller, L.O., Toro, E.F.: ADER scheme with a simplified solver for the generalized Riemann problem and an average ENO reconstruction procedure. Application to blood flow. *Computers & Fluids*, **248**, 105685 (2022).
- [26] Gaburro, E., Dumbser, M.: A Posteriori Subcell Finite Volume Limiter for General  $P_N P_M$  Schemes: Applications from Gasdynamics to Relativistic Magnetohydrodynamics. *J. Sci. Comput.* **86**, 37 (2021)
- [27] Dumbser, M., Loubère, R.: A simple robust and accurate a posteriori sub-cell finite-volume limiter for the discontinuous Galerkin method on unstructured meshes. *J. Comput. Phys.* **319**, 163 (2016)
- [28] Dumbser, M., Zanotti, O.: Very high order  $P_N P_M$  schemes on unstructured meshes for the resistive relativistic MHD equations. *J. Comput. Phys.* **228**, 6991 (2009)
- [29] Dumbser, M.: Arbitrary high order  $P_N P_M$  schemes on unstructured meshes for the compressible Navier-Stokes equations. *Computers & Fluids*. **39**, 60 (2010)
- [30] Boscheri, W., Dumbser, M.: Arbitrary-Lagrangian–Eulerian Discontinuous Galerkin schemes with a posteriori subcell finite-volume limiting on moving unstructured meshes. *J. Comput. Phys.* **346**, 449 (2017)
- [31] Charrier, D.E., Hazelwood, B., Tutlyaeva, E., Bader, M., Dumbser, M., Kudryavtsev, A., Moskovsky, A., Weinzierl, T.: Studies on the energy and deep memory behaviour of a cache-oblivious, task-based hyperbolic PDE solver. *The International Journal of High Performance Computing Applications*. **33**, 973 (2019)
- [32] Samfass, P., Weinzierl, P., Hazelwood, B., Bader, M.: TeaMPI — Replication-Based Resilience Without the (Performance) Pain. In book *High Performance Computing* edited by Sadayappan, P., Chamberlain, B.L., Juckeland, G., Ltaief, H., p. 455, Springer, Cham. (2020)
- [33] Samfass, P., Weinzierl, T., Charrier, D.E., Bader, M.: Lightweight task offloading exploiting MPI wait times for parallel adaptive mesh refinement. *Concurrency and Computation: Practice and Experience*, **32**, e5916 (2020)
- [34] Charrier, D.E., Hazelwood, B., Weinzierl, T.: Enclave Tasking for DG Methods on Dynamically Adaptive Meshes. *SIAM J. Sci. Comput.* **42**, 69 (2020)



- [35] Popov, I.S.: Arbitrary High Order ADER-DG Method with Local DG Predictor for Solutions of Initial Value Problems for Systems of First-Order Ordinary Differential Equations. *J. Sci. Comput.*, **100**, 22 (2024).
- [36] Gaburro, E., Boscheri, W., Chiocchetti, S., Klingenberg, C., Springel, V., Dumbser, M.: High order direct Arbitrary-Lagrangian-Eulerian schemes on moving Voronoi meshes with topology changes. *J. Comput. Phys.* **407**, 109167 (2020)
- [37] Gaburro, E.: A Unified Framework for the Solution of Hyperbolic PDE Systems Using High Order Direct Arbitrary-Lagrangian-Eulerian Schemes on Moving Unstructured Meshes with Topology Change. *Archives of Computational Methods in Engineering.* **28**, 1249 (2021)
- [38] Huynh, H.T., Wang, Z.J., Vincent, P.E.: High-order methods for computational fluid dynamics: A brief review of compact differential formulations on unstructured grids. *Computers & Fluids.* **98**, 209 (2014)
- [39] Jackson, H.: On the eigenvalues of the ADER-WENO Galerkin predictor. *J. Comput. Phys.* **333**, 409 (2017)
- [40] Zanotti, O.: ADER Discontinuous Galerkin schemes. Lecture Notes for the course at the Institute for Theoretical Physics. Frankfurt (2016)
- [41] Vilar, F.: A posteriori correction of high-order discontinuous Galerkin scheme through subcell finite-volume formulation and flux reconstruction. *Journal of Computational Physics.* **387**, 245 (2019)
- [42] Liu, S., Yuan, L.: A Modified A Posteriori Subcell Limiter for High Order Flux Reconstruction Scheme for One-Dimensional Detonation Simulation. *J. Sci. Comput.*, **97**, 31 (2023)
- [43] Krivodonova, L., Qin, R.: An analysis of the spectrum of the discontinuous Galerkin method. *Appl. Numer. Math.* **64**, 1 (2013)
- [44] Chalmers, N., Krivodonova, L., Qin, R.: Relaxing the CFL Number of the Discontinuous Galerkin Method. *SIAM Journal on Scientific Computing.* **36**, A2047 (2014)
- [45] Delfour, M.C., Hager, W., Trochu, F.: Discontinuous Galerkin Methods for Ordinary Differential Equations. *Math. Comp.* **36** 455 (1981)
- [46] Delfour, M.C., Dubeau F.: Discontinuous Polynomial Approximations in the Theory of One-Step, Hybrid and Multistep Methods for Nonlinear Ordinary Differential Equations. *Math. Comp.* **47** 169 (1986)
- [47] Baccouch, M.: Analysis of a posteriori error estimates of the discontinuous Galerkin method for nonlinear ordinary differential equations. *Applied Numerical Mathematics* **106**, 129 (2016)
- [48] Baccouch, M.: A posteriori error estimates and adaptivity for the discontinuous Galerkin solutions of nonlinear second-order initial-value problems. *Applied Numerical Mathematics* **121**, 18 (2017).
- [49] Baccouch, M.: Superconvergence of the discontinuous Galerkin method for nonlinear second-order initial-value problems for ordinary differential equations. *Applied Numerical Mathematics* **115**, 160 (2017)
- [50] Baccouch, M.: Analysis of optimal superconvergence of the local discontinuous Galerkin method for nonlinear fourth-order boundary value problems. *Numerical Algorithms* **86**, 16159 (2021)
- [51] Baccouch, M.: The discontinuous Galerkin method for general nonlinear third-order ordinary differential equations. *Applied Numerical Mathematics* **162**, 331 (2021)
- [52] Baccouch, M.: Superconvergence of an Ultra-Weak Discontinuous Galerkin Method for Nonlinear Second-Order Initial-Value Problems. *International Journal of Computational Methods* **20**(2), 2250042 (2023)
- [53] Toro, E.F.: *Riemann Solvers and Numerical Methods for Fluid Dynamics*. Springer, Berlin, Heidelberg (2009)
- [54] Springel, V.: *E pur si muove*: Galilean-invariant cosmological hydrodynamical simulations on a moving mesh. *MNRAS*, **401**, 791 (2010)
- [55] Schaal, K., Bauer, A., Chandrashekar, P., Pakmor, R., Klingenberg, C., Springel, V.: Astrophysical hydrodynamics with a high-order discontinuous Galerkin scheme and adaptive mesh refinement. *MNRAS*, **453**, 4278 (2015)